

FUNCTIONAL NANOSTRUCTURES
BY
ORDERED POROUS TEMPLATES

Dissertation

zur Erlangung des akademischen Grades

Dr. rer. nat.

genehmigt durch die

Mathematisch-Naturwissenschaftlich-Technische Fakultät
(Mathematisch-naturwissenschaftlicher Bereich)
der Martin-Luther-Universität Halle-Wittenberg

von Frau Dipl.-Phys. Yun Luo
geboren am 08.09.1976 in Shanghai

Gutachter:

1. Prof. U. Gösele
2. Prof. T. Thurn-Albrecht

Halle (Saale), Januar 2005, verteidigt am 20.06.2005

urn:nbn:de:gbv:3-000008613

[<http://nbn-resolving.de/urn/resolver.pl?urn=nbn%3Ade%3Agbv%3A3-000008613>]

Abstract

The objective of this thesis is to investigate ferroelectric micro- and nanotubes which have been successfully prepared by the template-wetting method. Template characterizations, mainly optical investigations of ordered porous alumina, and physical principles underlying wetting phenomena are investigated first. Micro- and nano-tubular structures, consisting of either inorganic ferroelectric oxides such as lead zirconate titanate (PZT) or barium titanate (BTO), or organic ferroelectric copolymers such as P(VDF-co-TrFE), are obtained by wetting of the porous templates. Their physical properties, particularly crystallinity and ferroelectric switchings, are explored by *X-ray diffraction* and *Scanning force microscopy*, respectively. Especially for the P(VDF-co-TrFE) copolymer nanotubes, the phase behaviors are investigated by *Differential scanning calorimetry* and information on ferroelectric domain structures on the tube walls is drawn by *Piezoresponse force microscopy* measurements. Pt nanoshell tubes are also fabricated which may serve as electrodes at both the inner and outer walls of the ferroelectric tubes. To construct simple hybrid systems from the 1D functional micro- and nano-objects for the purpose to be potentially used as building blocks to assembly functional devices, two ways are employed: either to construct multi-layer metal-oxide-metal micro- and nano(shell) tubes, or to fabricate tubes free-standing orderly from a silicon substrate on a macroscopically large scale (cm^2). These results show in principle the feasibility to integrate these 1D structures as building blocks of miniaturized devices in the fields of MEMS or NEMS.

Kurzfassung

Das Ziel dieser Arbeit ist die Untersuchung ferroelektrischer Mikro- und Nanoröhrchen, die mittels Templatbenetzung erhalten wurden. Die Eigenschaften der porösen Templat, insbesondere die optischen Eigenschaften von geordnetem porösen Aluminiumoxid, sowie die der Templatbenetzung zugrunde liegenden physikalischen Phänomene werden diskutiert. Mikro- und Nanoröhrchen konnten einerseits aus anorganischen ferroelektrischen Oxiden wie Bleizirkonat-titanat (PZT) und Bariumtitanat (BTO), andererseits aus ferroelektrischen Kopolymeren wie Poly(vinylidenfluorid-co-trifluorethylene) P(VDF-co-TrFE) hergestellt werden. Ihre physikalischen Eigenschaften, insbesondere ihre Kristallinität und ihre ferroelektrische Schaltbarkeit, wurden mittels Röntgenbeugung bzw. rastersondenmikroskopischer Methoden untersucht. Im Falle von P(VDF-co-TrFE) Kopolymer-Nanoröhrchen diente dynamische Differentialkalorimetrie zur Untersuchung des Phasenverhaltens, während die ferroelektrischen Domänen mit Hilfe von *Piezoresponse Force*-Mikroskopie charakterisiert wurden. Ebenso wurden Platin-Röhrchen hergestellt, die als Elektroden für die ferroelektrischen Röhrchen dienen können. Zur Generierung von Hybridstrukturen als potentielle Bauelemente in komplexen funktionalen Architekturen wurden zwei Ansätze verfolgt: Mehrschicht-Röhrchen wurden durch aufeinanderfolgende Benetzungsschritte erhalten. Weiterhin konnten makroskopisch ausgedehnte, hochgeordnete Anordnungen paralleler Röhrchen hergestellt werden. Diese Ergebnisse zeigen im Prinzip die Integrierbarkeit eindimensionaler Nano- und Mikrostrukturen in komplexe funktionale Architekturen.

Contents

1	Introduction	2
1.1	Scope of the thesis	2
1.2	Building blocks of tomorrow’s storage devices	2
1.3	“Millipede” - a new approach for storing data	3
1.4	Ferroelectric materials for nano- and microelectronics	4
1.4.1	Ferroelectricity and piezoelectricity	4
1.4.2	Ferroelectric nano- and microtubes - better candidates for cantilevers?	6
1.4.3	Ordered arrays of piezoelectric nano- and microtubes: a new route toward mass storage devices	8
1.5	Array design, technology and fabrication	9
1.5.1	Template-directed approaches to 1D micro- and nanostructures	9
1.5.2	Basic building blocks for functional devices	10
1.6	Organization of the thesis	13
2	Exploiting wetting phenomena to tailor 1D nano- and microstructures	15
2.1	Wetting on a macroscopic scale	15
2.1.1	Contact angle and Young’s law	15
2.1.2	Tanner’s law	17
2.1.3	Spreading coefficient	18
2.2	Wetting on a microscopic scale	18
2.2.1	Role of the disjoining pressure	18
2.2.2	Precursor films	19
2.3	Wetting by liquid polymers	21
2.4	Wetting the walls of cylindrical pores by non-volatile liquids	22
2.4.1	Capillary rise	22
2.4.2	The pinch-off mechanism	22
2.4.3	Rayleigh instability	23
2.5	Wetting of surfaces with critical mixtures	24
2.5.1	Critical point wetting	24
2.5.2	Surface-directed spinodal decomposition	25
2.6	Structure formation processes during the wetting of porous materials with polymeric liquids	26
2.6.1	Adaption of wetting phenomena from flat substrates to porous templates	26
2.6.2	Occurrence of Rayleigh instabilities	27
2.6.3	Tailoring the morphology of the tube walls	28
2.7	Summary of the chapter	29
3	Ordered porous templates	30
3.1	Porous alumina templates	31
3.1.1	Disordered pore arrays	31
3.1.2	Pore arrays with polycrystalline degree of order	31

3.1.3	Monodomain porous alumina obtained by nanoimprint lithography (NIL)	32
3.2	Macroporous silicon templates	41
3.3	Summary of the chapter	42
4	Experimental details	44
4.1	Preparation of tubes or wires from porous templates	44
4.2	Characterization methods of 1D micro- and nanostructures	45
4.2.1	Electron microscopy	45
4.2.2	X-ray diffraction (XRD)	46
4.2.3	Scanning force microscopy (SFM)	46
4.2.4	Differential scanning calorimetry (DSC)	50
4.3	Summary of the chapter	51
5	Building Blocks I: Ferroelectric inorganic micro- and nano(shell) tubes	52
5.1	New candidates for nanoelectronics: ferroelectric nanotubes	52
5.2	Large-scale fabrication of inorganic ferroelectric nano(shell) tubes by template wetting	53
5.3	Morphology and crystallinity of ferroelectric nano(shell) tubes	54
5.4	Occurrence of Rayleigh instabilities	56
5.5	Ferroelectric hysteresis of individual ferroelectric nano(shell) tubes	57
5.6	Summary of the chapter	58
6	Building blocks II: Ferroelectric P(VDF-co-TrFE) copolymer nanotubes	59
6.1	Properties of PVDF and its copolymers	59
6.2	Fabrication of P(VDF-co-TrFE) copolymer nanotubes	62
6.3	Characterization of P(VDF-co-TrFE) copolymer nanotubes	63
6.3.1	Morphology	63
6.3.2	DSC investigations	63
6.3.3	XRD results on unpoled P(VDF-co-TrFE) embedded in porous alumina	70
6.3.4	Ferroelectric properties	74
6.4	Summary of the chapter	78
7	Building blocks III: metallic micro- and nano(shell) tubes and multi-layer tubes	79
7.1	Pt nano(shell) tubes via organometallic composite precursors	79
7.1.1	Crystallinity of Pt nano(shell) tubes	80
7.1.2	Morphology characterization of Pt nano(shell) tubes	81
7.1.3	Metal/organic composite tubes	82
7.2	Multi-layer nano(shell) tubes	83
7.3	Summary of the chapter	86
8	Conclusions and outlook	87
8.1	Conclusions	87
8.2	Outlook	88
9	Curriculum vitae	99

1. Introduction

1.1 Scope of the thesis

The aim of this thesis is to investigate the physical and structural properties of ferroelectric micro- and nano-tubes which can be potentially used as building blocks to assembly functional devices for the purpose of mass storage. The choice of ferroelectric tubes is based on the following features:

- Their state can be controlled precisely with little energy consumption due to their thin wall thickness;
- They can be easily integrated into device architectures in the form of ordered tube arrays;
- As actuator cantilevers, ferroelectric tubes have more deflection freedom than thin films and wires;
- An individual ferroelectric tube with domains having polarizations perpendicular to the tube walls can act as a barcode;
- The ferroelectricity is scalable, thus, in the long-run, we expect that such ferroelectric nano- and micro-tubes can be used as building blocks in mass storage devices on the nanometer scale.

The method proposed in this thesis to fabricate 1D nano- and micro-objects is based on wetting of ordered porous templates. By a controlled procedure, tubes and wires in the nano- and micro-ranges composed of inorganic ferroelectrics and organic polymers as well as metals have been realized and characterized, respectively. A first step towards an assembly, which is a tri-layer metal/ferroelectrics/metal tubular structure, is also proposed in this work which might lead to such functional devices as a mass storage similar to IBM's "Millipede".

1.2 Building blocks of tomorrow's storage devices

In the 21st century, the information technology will move from structured elements in the micrometer range to those in the nanometer range. The involved nanotechnology is often somewhat arbitrarily defined as containing structural or functional elements on a scale smaller than 100 *nm*. With the fast evolution of new technology, the nanometer scale is expected to pervade also such fields as data storage. Today, most data storage is realized by magnetism in which no clear-cut way has been shown to achieve the nanometer scale in all three dimensions. With its speedy developments, however, magnetic storage technology will doubtless arrive at a point where fundamental physical phenomena start to become important, e.g., the well-known limit of superparamagnetism. Several ideas have been proposed to overcome this limit.

For key areas in information technology, especially in the areas of nano-electronics and data storage, it is not yet obvious which materials and technologies will offer potential alternatives

to the magnetic storage approach. Any emerging technology which could be considered seriously as a substitute for an already-existing but limited one must be able to provide long-term perspectives. In the case of storage device, any new technique, which has a better storage capability than today's magnetic recording [1], should possess the long-term possibility for further scaling.

An available tool well-known today which is suitable as a potential replacement technique and which offers long-term perspectives is a sharp tip with a dimension in the nanometer range. Such tips are widely used in atomic force microscopes (AFM) and scanning tunnelling microscopes (STM) for imaging and structuring down to the atomic scale. The main function of the simple tips lies in the local confinement of interaction between the tip and another medium which is manipulated or characterized.

In 1992, Mamin *et al.* at the *IBM Almaden Research Center* pioneered the possibility of using an AFM tip for readback and writing of topographic features for the purpose of data storage [2]. In the scheme developed by them, reading and writing were demonstrated with a single AFM tip in contact with a rotating polycarbonate substrate, as shown in figure 1.1. Data was formed by a thermomechanical process by applying local heating and force to the polymer through the tip. In this way, densities of up to 30 Gb/in^2 were achieved. This represented a significant advance in the storage densities of that day. Later, this system was further refined which included mainly an increase in the readback speeds to a data processing rate of 10 Mb/s [3].

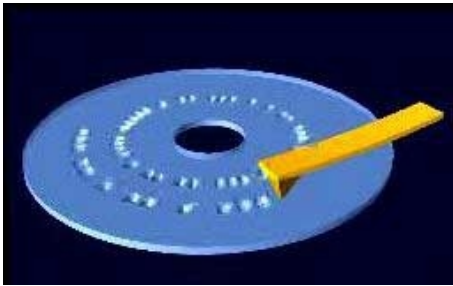


Figure 1.1: Performance of thermomechanical writing with an AFM tip on a rotating polymer surface. A focused laser beam propagates through a transparent Poly(methyl methacrylate) (PMMA) sample and heats the optically absorbing AFM tip. The heated tip softens the substrate, and the local tip pressure creates an indentation. The sample is placed on a precision air-bearing spindle to allow for sample rotation [2].

There also exist fundamental limits for high data processing rate in exploiting single tips in AFM operation for storage, at present mainly including, the mechanical resonant frequencies of the AFM cantilevers limit the data rates of a single cantilever to a few Mb/s [4, 5]. The operation time of a single AFM at present does not have advantage over the conventional magnetic storage either. Currently, a single AFM operates at best on the microsecond time scale while conventional magnetic storage operates at best on the nanosecond time scale. To be competitive not only with the currently existing magnetic recording but also with future developments, the AFM data rates have to be improved by at least three orders of magnitude.

1.3 “Millipede” - a new approach for storing data

At the end of 1990's, the scientists in *IBM Zurich* proposed a new concept, the so-called “Millipede” [6], which has the potential to store data at high speed with an ultrahigh density. The feasibility of this high-density data storage system was suggested to be based on micromechanical components borrowed from AFM: tiny depressions melted by an AFM tip into a polymer medium represent stored data bits that can then be read by the same tip [6]. This thermomechanical storage technique is capable of achieving data densities in the hundreds of Gb/in^2 range, well beyond the expected limits for magnetic recording ($60 - 70 \text{ Gb/in}^2$). Whereas the readback

rate of an individual probe is limited, high data rates can be achieved through the use of massive parallelism: in the “Millipede” system concept, the read/write head consists of an array of more than 1000 thermomechanical probes, fabricated on a single silicon chip using Very Large Scale Integration (VLSI) microfabrication techniques, which operate simultaneously.

As illustrated in figure 1.2, at the heart of the prototype “Millipede” storage system is an array of 1,024 tiny V-shaped levers with very sharp tips. The whole array lies on an area of 3mm^2 . Each cantilever is $0.5\ \mu\text{m}$ thick and $70\ \mu\text{m}$ long. The tip at the point of the “V” on the cantilevers is two micrometers long. Beneath the array of cantilevers is a polymer layer that acts as the medium for storing bits of information. Bits are written and read thermomechanically.

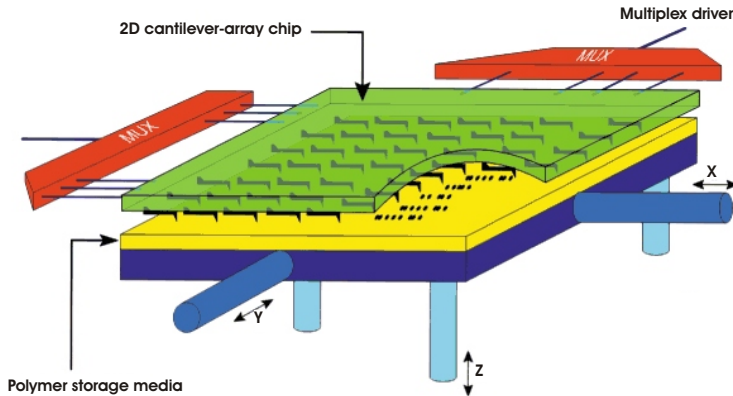


Figure 1.2: Illustration of the “Millipede” concept [6].

Prototype versions of “Millipede” have gone through more than 100,000 write-and-erase cycles to prove the durability of the system. Currently, data can be read and written from the device at a rate of a few Kb/s , but the IBM researchers estimate that with refinement the system could boost this to Mb/s . The plastic film that data is written on and from is moved around beneath the lever array so that each individual tip addresses an area on the order of $100\ \text{nm}^2$.

Using this set-up, the IBM researchers managed to cram $500\ \text{Mb}$ of data into each $100\ \text{nm}^2$ area. This is approximately 20 times denser than that can be achieved with the best magnetic storage system today. Upon realization, this new technology could bring vast amounts of data which could be stored in the mobile phones, laptop computers and even watches. In the present thesis, I will suggest an approach for an analogous data storage device replacing the individual cantilevers by piezoelectric tubes.

1.4 Ferroelectric materials for nano- and microelectronics

1.4.1 Ferroelectricity and piezoelectricity

The word “piezo” originates from Greek, which means “to press” or “to squeeze”. Piezoelectric materials are a class of materials that can be polarized by applying a mechanical stress or an electric field. The direct piezoelectric effect is described as that when an external stress is applied to the material, charges appear [7]. This can be illustrated by a linear relation of the charge density D_i as a function of the stress X_{jk} applied to the piezoelectric material (using the Einstein summation convention):

$$D_i = d_{ijk}^{\text{direct}} X_{jk} \quad (1.1)$$

where d_{ijk} is the third-order piezoelectric coefficients tensor measuring in $[C/N]$. The piezoelectric coefficient measured in the direction of the applied field is usually called the longitudinal coefficient, and that measured in the direction perpendicular to the field is known as the transverse coefficient [7]. Other piezoelectric coefficients are denominated shear coefficients.

The reverse effect is that a strain appears when the piezoelectric material is subject to an external electric field. The corresponding relation is also described by a linear equation which relates the X_{ij} developed in a piezoelectric material and the external electric field E_k :

$$X_{ij} = d_{kij}^{reverse} = (d_{ijk}^{direct})^t E_k \quad (1.2)$$

where t denotes the transposed “matrix”. The unit of the reverse piezoelectric coefficient is $[m/V]$.

Practically, it is useful to relate the piezoelectric coefficients to the local spontaneous polarization (P_S). For most ferroelectric materials, the paraelectric phase is centrosymmetric, which leads to the disappearance of the linear piezoelectric coefficients. For the ferroelectric phase which is nonlinear, higher order terms give:

$$d_{im} = \epsilon_{ij} Q_{mjk} P_{Sk} \quad (1.3)$$

where Q_{ijk} are the polarization-related electrostrictive coefficients and ϵ_{ij} the linear dielectric tensors.

For the particular case of tetragonal symmetry where axis “3” is the polar axis, $P_{S1} = P_{S2} = 0$, $\epsilon_{11} = \epsilon_{22}$, $\epsilon_{ij} = 0$ for $i \neq j$, and the only non-zero electrostrictive coefficients are $Q_{11} = Q_{22}$, $Q_{12} = Q_{21}$, $Q_{13} = Q_{23}$, $Q_{31} = Q_{32}$, Q_{33} , $Q_{44} = Q_{55}$, Q_{66} . It follows:

$$d_{33} = \epsilon_{33} Q P \quad (1.4)$$

By this equation, the absolute value of the polarization can be estimated if the electrostrictive coefficient Q and the dielectric constant ϵ_{33} are known.

In a “standard” dielectrics, positive and negative charges are displaced from their original position by the application of an external electric field. This creates a dipole moment, the polarization. However, this polarization will vanish, if the electric field is switched back to zero. In a ferroelectric material, on the contrary, a permanent displacement is inherent to the material and does not disappear in the absence of the external electric field. The direction of this polarization can be switched by applying an appropriate external field. In fact, the key property of a ferroelectrics is described by the switchable spontaneous polarization by an external electric field. As a result, the polarization will not be a linear function of the applied electric field as it would be in a normal dielectrics. It shows hysteresis behavior. The ideal case is depicted in figure 1.3a. At any point, it is approximately given by

$$\mathbf{P} = \mathbf{P}_s + (\epsilon - 1)\mathbf{E} \quad (1.5)$$

where the spontaneous polarization \mathbf{P}_s is equal to the polarization in the absence of an external electric field within a single ferroelectric domain.

In a real case, the loop is less square due to the presence of nucleation centers, which induce an earlier switching (as depicted in figure 1.3b). At that time, the spontaneous polarization is

obtained by extrapolating the polarization at high electric field linearly down to zero field [8]. P_r stands for the polarization remaining after the disappearance of the external electric field. It is worth to mention that the remnant polarization is not a material parameter as it would be for the spontaneous polarization. P_r depends on the history of the sample, e.g., on the amplitude of the last electric field used for poling.

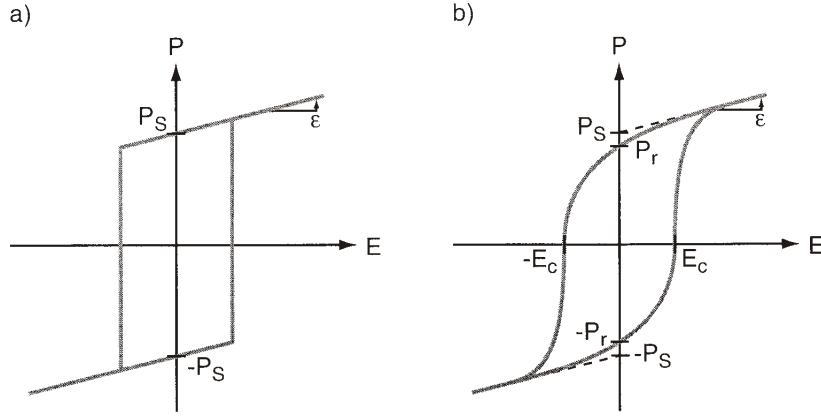


Figure 1.3: (a) Hysteresis loop of an ideal ferroelectric domain. (b) Hysteresis loop of a real ferroelectric material [9].

Most ferroelectrics exist in a paraelectric form \mathcal{P} at higher temperatures and transform into a non-centrosymmetric phase \mathcal{F} on cooling below a characteristic temperature, the so-called *Curie point*, T_c . This phase transition can be depicted by a change in point symmetries from \mathcal{P} to $\mathcal{F} \subset \mathcal{P}$.

Ferroelectric phase transitions are said to be of the first-order when the spontaneous polarization changes abruptly at the Curie point. Second-order phase transitions are characterized by a smooth disappearance of the spontaneous polarization at the Curie point. The two mostly commonly used materials, barium titanate ($BaTiO_3$, *BTO*) and lead zirconate titanate ($PbZrTiO_3$, *PZT*), treated in this dissertation, possess a first-order transition.

Upon cooling through T_c , a spontaneous polarization evolves. It will be different in different areas in a crystal. Thus the crystal consists in general of many domains. Neighboring domains are separated by domain walls.

1.4.2 Ferroelectric nano- and microtubes - better candidates for cantilevers?

1D ferroelectric structures, such as tubes and wires in nano- and micro-scales, belong to a newly developing category of nano- and microscale ferroelectrics [10]. As illustrated in figure 1.4a, a piezoelectric tube, which could be either an ABO_3 perovskite type oxide, e.g., *PZT*, *BaTiO_3*, *PbTiO_3*, *LiNbO_3*, *LiTaO_3* or *Bi₁₂GeO₂*, or a ferroelectric polymer, e.g., PVDF and its copolymers, can be fabricated into a new type of cantilever with its inner and outer electrodes in the same configurations as the conventional piezoelectric scanner used in nowadays scanning probe microscopes. With one end fixed onto a substrate and the other end kept freely moving, as well as four properly attached electrodes respectively at the inner and outer pore walls, such a piezoelectric tube could be deflected in the desired direction by the application of an external electric voltage ($\pm V_x$, $\pm V_y$) between one inner and one outer electrodes on the opposite sides

across the tube wall. This allows a 3D movement of the free end of the tip. Vice versa, a controlled deflection can also create voltages.

We propose that such ferroelectric tubes, either composed of inorganic perovskite materials, with a diameter within the micrometer range ($0.05 \mu m - 5 \mu m$) but with a wall thickness in the nanometer range ($10 nm - 100 nm$), or composed of organic polymers, with a diameter from $25 nm$ to $400 nm$ and a wall thickness of around $30 nm$ (when the diameter is larger than $60 nm$), when mounted with a sharp tip (e.g., a diamond-like carbon tip), could potentially be better candidates for the levers (as shown in figure 1.4b) used in mass-storage devices due to the following advantages besides the usual advantages of ferroelectric thin films used in nowadays FeRAMs:

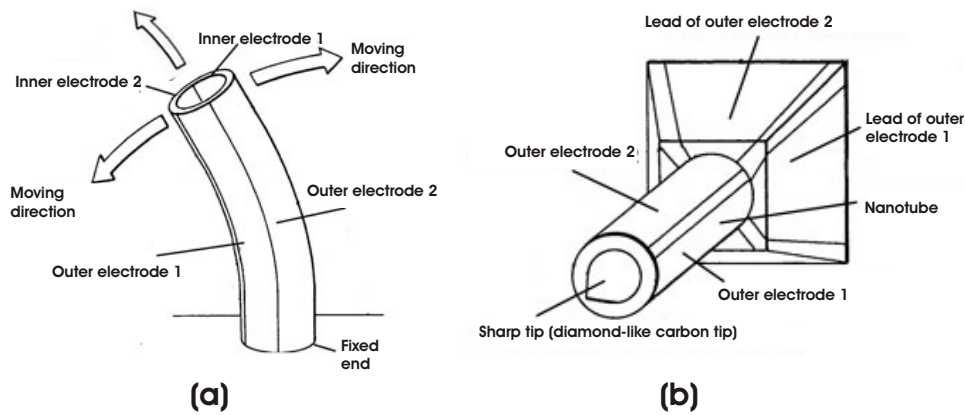


Figure 1.4: (a) A piezoelectric tube, either made of an inorganic perovskite material or made of an organic polymer, with its properly attached electrodes, can be manipulated by the application of an external electric field. (b) Schematic of a sub-micron piezoelectric scanner and active cantilever.

- For very thin tube walls, the deflection of the tube can be controlled precisely by small voltages applied to the electrodes. For a piezoelectric tube of $1 \mu m$ in diameter, $50 nm$ wall thickness and $100 \mu m$ in length, $1 V$ applied between the inner and outer electrodes on the opposite sides across the tube wall can induce a movement of the free end of the tube as much as $2.5 \mu m$. If voltages are applied to all the four pairs of the inner and outer electrodes across the tube wall in the same direction, e.g., from outer electrode to inner electrode or from inner electrode to outer electrode at the same time, an elongation or shrinkage in the z direction can happen. Calculations show that $1 V$ applied on all the four pairs of electrodes can induce a change of $600 nm$ in the length of the tube. This means that only small voltages are required for a manipulation of such a piezoelectric tube.
- Such piezoelectric nano- and microtubes are compatible with the *Complementary Metal Oxide Semiconductor (CMOS)* driving circuits. As stated above, a movement of $1 \mu m$ of the free end of the tip of the tube needs $0.4 V$ as the voltage applied. As a result, such piezoelectric nano- and microtubes can be readily integrated into the already existing CMOS logical circuits. We expect that even more sophisticated functions can be integrated via such a piezoelectric tube on a very local scale.

1.4.3 Ordered arrays of piezoelectric nano- and microtubes: a new route toward mass storage devices

Similar to the concept of “Millipede” depicted in figure 1.2, which is not just a modification of an already existing storage technology, but involves a new concept in which high data rates result from massive parallel operation of arrays of tips, highly ordered arrays of ferroelectric nanotubes also have a large application potential in the same field as mass storage devices, as shown in figure 1.5.

Such a mass storage chip composed of arrays of piezoelectric tubes is based on a mechanical parallel x/y scanning of the individual tubes without movement of the whole chip over a storage medium, which can be the same material as in the case of “Millipede”, a thin polymer film. In addition, a feedback-controlled z -approaching and z -levelling scheme bring the entire cantilever array chip into contact with the storage medium. This tip-medium contact is maintained and controlled while x/y scanning of the individual tubes is performed in parallel for write/read. It is important to note that this data processing approach is not based on individual z -feedback for each cantilever; rather, it uses a feedback control for the entire chip, which greatly enhances the efficiency. That means, in such devices, all the micro-cantilevers (piezoelectric tubes) scan independently their individual area and write/read data in an associated section of the storage medium, which is called a bit array of a storage field. Compared to the conventional mass storage devices, the ferroelectric probe arrays permit a fully random read/write with an increased access speed since the individual storage field is not read out in series, but in parallel. The speed of the proposed device could potentially exceed the present access time limit, which is in the 10 ms range.

During the storage operation, the chip is raster-scanned over an area called the storage field. The scanning area of an individual tube is equivalent to the cantilever x/y pitch, which is currently $1.5\ \mu\text{m}$. Each cantilever tip of the array writes and reads data only in its own storage field. This eliminates the need for lateral positioning adjustments of the tip to offset lateral position tolerances in tip fabrication. Consequently, a 32×32 array chip will generate 32×32 ($\sim 1,024$) storage fields on an area of less than $50\ \mu\text{m} \times 50\ \mu\text{m}$. Assuming an areal density of $500\ \text{Gb}/\text{in}^2$, a storage field of one cantilever ($1.5\ \mu\text{m} \times 1.5\ \mu\text{m}$) has a capacitor of about $2 \times 10^{-3}\ \text{Mb}$, and correspondingly a 32×32 array chip has a storage capacity of $2\ \text{Mb}$ on an area of less than $50\ \mu\text{m} \times 50\ \mu\text{m}$. Compared to the concept of “Millipede” which has an x/y pitch of $92\ \mu\text{m}$, the data access rate might be increased as the area each ferroelectric tubular cantilever reads/writes is much smaller.

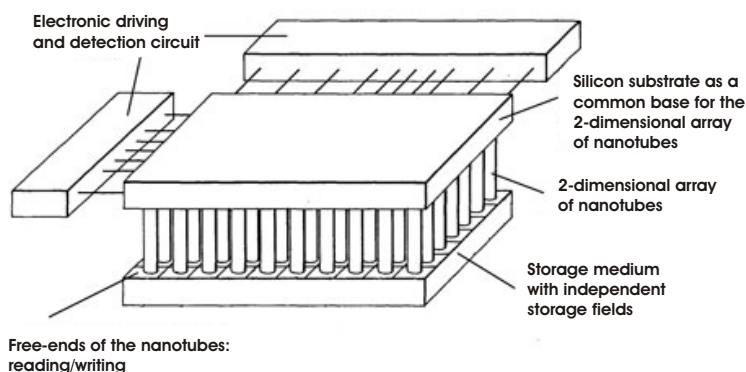


Figure 1.5: A mass storage device which is based on highly ordered arrays of piezoelectric tubes on a large scale. In such a device, all the micro-cantilevers (piezoelectric tubes) scan independently their individual area and write/read data in an associated section of the storage medium, which is called a bit array of a storage field.

In real applications, the space needed for the individual write/read wiring of each tube has to be considered. The row and column time-multiplexing addressing scheme implemented successfully in every DRAM is a very elegant solution to this issue. We propose that in our data storage device which is based on piezoelectric tubes, this can be done in the same way as in the case of the “Millipede”, that is, the time-multiplexed addressing scheme is used to address the array row by row with full parallel write/read operation within one individual row.

1.5 Array design, technology and fabrication

Before any prototype of the above-proposed mass storage device can be fabricated, which is based on arrays of functional piezoelectric tubes, different building blocks must be accomplished. They include the preparation and characterization of:

1. Functional piezoelectric nano- and microtubes composed of materials of either an inorganic perovskite oxide or an organic polymer, adopting a configuration of either released or as arrays.
2. Metallic coatings which could be at specific places at the outer wall and/or inner wall of the piezoelectric nano- and microtubes. These metallic structures also have tubular configurations. Potentially, they could be carried out by the same method as the one used for piezoelectric nano- and microtubes.
3. Individual complex tubular structures with their tube wall consisting of metal/ferroelectrics/metal in radial direction consecutively. This allows for the realization of a prototype of functionality of an individually controllable cantilever.
4. Ordered arrays of functional complex tubular structures.

This thesis will deal with all these steps though not all details (e.g., separated four electrodes on the outer surface of the piezoelectric tubes) could be solved and realized within the scope of the work. The results of this thesis will be helpful as first steps towards the realization of the suggested mass storage device.

1.5.1 Template-directed approaches to 1D micro- and nanostructures

The fabrication method we chose to use in the fabrication of the above elements is based on template-directed approaches, especially template-wetting.

As a straightforward route towards the fabrication of 1D nanostructures, template-directed approach entails synthesizing the desired materials in desired topology via a wealth of templates. The structures so-obtained are complementary to those of the templates. Notable examples include:

- Templating against features on solid substrates such as described in [11, 12]. By this method, metal nanowires as thin as 15 *nm* were prepared by shadow sputtering a metal source against an array of V-grooves etched on the surface of a Si(100) wafer.
- Templating against self-assembled molecular structures. It explores the fact that surfactant molecules spontaneously organize into rod-shaped micelles (or inverse micelles) when their concentration reaches a critical value [13].

- Templating against existing nanostructures. For example, gold nanorods are directly coated by polystyrene or silica (5 – 10 *nm* in thickness) to form cable-like nanostructures [14].
- Templating within the pores of a porous membrane. The most outstanding character of this method is that it is extremely general with regard to the types of materials that can be prepared [15, 16, 17].

Among all the template-related methods listed above, synthesis within the channels of porous materials is of our particular interest. This method has several unique advantages: First of all, it is versatile, with the possibility to prepare nanotubes composed of various materials (e.g., metals [18], semiconductors [19], ceramics [20], and polymers [21]) in a controlled manner. The diameter of the tubes can be as small as 3 *nm* [22]. The nano- and micro-objects obtained are mono-disperse and can be either released from or connected to the templates used.

With the so-called template-wetting method proposed in this thesis, which exploits wetting phenomena based on the ability of low surface energy liquids to wet high surface energy solids, we are thus able to make the first step towards the fabrication of all the 1D elements necessary to realize such functional-tubes-based mass storage devices.

1.5.2 Basic building blocks for functional devices

We chose the following basic building blocks to be realized first before the fabrication of any complex structures can be attempted:

Piezoelectric nano- and microtubes composed of perovskite ABO_3 ceramics

The first core building block consists of ferroelectric nano- and microtubes which are composed of perovskite ABO_3 ceramics.

Dynamic random access memories (DRAMs) are the workhorses for memory chips. Presently, the most commonly used nonvolatile memories are “flash memories” and electronically erasable programmable read only memories (EEPROM). They have common drawbacks: lack of speed, without easy and unlimited reprogrammability, and they are relatively expensive. To overcome these shortcomings of flash memories and EEPROMs, advanced concepts are explored based on either magnetic or ferroelectric materials. Perovskite oxides are prime candidates for these applications, because of their high permittivity in the paraelectric phase or their ferroelectric properties [23]. They also have such advantages as lower operating voltages, improved read/write time-scale and physical robustness compared to the already existing memory types. In fact, these materials are already on the way to memory densities comparable to these of conventional ferroelectrics. The fabrication of future nanoscale capacitors with improved performance for non-volatile memory applications will very likely rely on the new technology of complex oxides. Ferroelectric random access memory devices (FeRAMs) use the remanent polarization for non-volatile information storage.

As described earlier in this chapter, ferroelectrics belongs to polar materials whose spontaneous polarization, in an attainable range of temperature and pressure, possesses at least two equilibrium orientations in the absence of an external electric field. The direction of the spontaneous polarization can be used to store information. This is employed in nonvolatile random access memories. Ferroelectrics also often exhibit a large dielectric permittivity which can be used in thin film capacitors and DRAMs. The piezoelectricity of ferroelectrics is used in actuators,

microelectromechanical systems (MEMS) and pressure sensors, while their pyroelectricity is used for load-sensitive pyroelectric sensors.

The preparation of functionalized nanotubes from complex oxide ferroelectrics is of general interest in materials science. Recently, ferroelectric nanorods with diameters as small as 5 nm to 60 nm and with lengths of more than $10\text{ }\mu\text{m}$ were obtained by a solution-phase decomposition of bimetallic alkoxide precursors in the presence of coordinating ligands [24]. By means of electrostatic force microscopy, ferroelectric switching was shown in a 12 nm diameter rod [25]. Application advantages of these devices include [26] “enhancing the piezoelectric response of composite materials by five orders of magnitude in comparison with bulk ceramic materials”.

Moreover, the fabrication of such FeRAMs poses significant technological challenges. Naturally, the great interest in nanoscale leads to a question: how small may be a ferroelectric component from a capacitor that is still remaining stable and switchable?

A point to note here is that, for practical applications, especially with diameters in the mesoscale range, ferroelectric oxide tubes are more desirable than the simple rods. A rod cannot be manipulated in the same way as a tube. Especially for tubes with thin walls, they can be manipulated very precisely and thus very sensitively on a local scale.

Compared to the method used in [24], a big advantage of the template-wetting method (which will be described in more details in this thesis) to fabricate these piezoelectric nano- and microtubes lies in the possibility that the large-scale configuration of the tubes can be designed *a priori* by the design of the template used. That means, free-standing arrays of ferroelectric nano- and microtubes can be accomplished not only on relatively large-scale but also with desired arrangement such as hexagonal or squared which is related to the specific structure of the templates.

Ferroelectric nanotubes composed of organic polymers

1D ferroelectric nano- and micro-objects can also be realized by organic polymers besides inorganic ceramics. In recent years, there has been an increasing recognition of the importance of polymeric materials which can be incorporated as active elements in electric circuits. Among the properties which can be exploited, an important one is piezoelectricity. Due to the molecular, crystalline and morphological structure of polymers, they have the potential to comply with the restrictive requirements of piezoelectricity and its two related properties: pyroelectricity and ferroelectricity. The investigations of Kawai in 1969 [27] on elongated and polarized films revealed a large piezoelectric effect exhibited by poly(vinylidene fluoride) (PVDF) with the molecular repeating unit ($\text{CH}_2\text{-CF}_2$).

Ferroelectricity has also been found in certain copolymer compositions of VDF with trifluoroethylene, TrFE [28, 29, 30, 31, 32] and tetrafluoroethylene, F_3E [33]. Specially, copolymers of P(VDF-co-TrFE) are of great interest because of their outstanding ferroelectricity [31, 34, 35], together with a concurrent strong piezo- [29] and pyroelectricity. These polymers exhibit, in addition, an important aspect of ferroelectricity that so far has not been demonstrated in PVDF: the existence of a Curie temperature at which the crystals undergo reversibly a ferroelectric-to-paraelectric phase transition in a wide range of VDF-to-TrFE compositions. In PVDF, the existence of such a ferroelectric-to-paraelectric transition is still uncertain, and, in fact, it is generally believed that melting may intervene before the onset of such a phase transition.

Although piezoelectricity in synthetic polymers is not as high as that in naturally occurring

single crystal inorganic materials and ceramics, the advantage of these polymeric materials as piezoelectric elements arises because they have lower density, more flexibility, and are easier to process. They also show a much higher dielectric strength and much better chemical resistance than ceramics together with a lower mechanical and acoustic impedance which make them good candidates for building blocks as sensors of mechanical signals. In fact, PVDF has already been used in many applications such as transducers in ultrasonic cardiac imaging, blood pressure and pulse measurements, touch sensors in robotics [36], optical fiber coatings for electric field sensing [37], and, as a programmable neural network system [38]. They can also be used in composites with piezoelectric ceramics to improve their properties in device applications [39].

PVDF nanotubes were prepared by Steinhart *et al.* [40] by wetting of ordered porous templates. Although crystallization occurring within the nanotube walls exhibits directional crystal growth due to the confined geometry and curvature within the pores of the template, only the non-polar α -phase was observed. In order to get better functionality, e.g., piezoelectricity and pyroelectricity, a substitute has to be used.

1D ferroelectric polymeric nano- and micro-objects which will be realized in this thesis are based a copolymer, P(VDF-co-TrFE). The P(VDF-co-TrFE) nanotubes or nanowires obtained by the template-wetting method show piezoelectric properties which makes them promising to be used in parallel to inorganic ferroelectric nano- and microtubes in various applications. Compared to ferroelectric ceramics, the ferroelectric polymers are more readily altered to conform to complex device requirements imposed by the environment, size, shape, reliability and durability. They can also be easily patterned for integrated electronic applications. Ferroelectric polymers adhere well to a wide variety of substrates yet difficult for many other ferroelectric ceramics.

Metallic nano(shell) tubes

As shown earlier, in order to move the free end of a piezoelectric tube, it is necessary to apply an external electric voltage via a certain configuration of metallic electrodes. In this sense, to fabricate metallic nano- and microtubes which can be adapted to the configuration of the ferroelectric tubes is necessary. Besides the use as electrodes, metallic nano- and microstructures have a lot of further applications, such as catalysts, hydrogen storage and sensors.

Hollow structures made of metals, so called metallic nanoshell tubes or metallic nanoshell particles, are attractive mainly because they do not only exhibit such important features as surface plasmonic resonances and catalytic activities different from and even superior to their bulk counterparts [41, 42], but also have the potential to serve as electrodes in integrated electronic devices on the nanoscale. Among all the metals, platinum (Pt) is of particular interest as the most widely used catalyst and electrode.

For applications in the field of catalysts and electrodes, it is advantageous to employ Pt nanoparticles [43, 44, 45] and nanotubes [46, 47], with a considerably enhanced surface-to-volume ratio compared to bulk Pt. Particularly interesting are Pt nano(shell) tubes within the pores of a membrane acting as a support. Such hybrid systems may exhibit channels with diameters ranging from a few tens of nm to several μm and depths up to hundreds of μm with Pt-coated walls. The advantages compared to dispersed systems are obvious: no precipitating and flocculating of the Pt species reducing its activity occur. Pt-coated porous membranes are easy to handle, and no tedious recovering procedures are necessary as in the case of dispersed Pt nanoparticles. They are ideal building blocks for miniaturized flow reactors. Tubes should be prevented from leaching rather than discrete nanoparticles attached to the pore walls that could be removed by

a flowing medium. Aligned pores within a membrane having blind ends, whose walls being coated with Pt, may allow performing Pt catalyzed reactions within their interior. Such hybrid systems containing functionalized microcavities could be promising materials for the “lab on a chip” technology. Furthermore, Pt coated porous materials may be used as nanostructured electrodes [48] which can in turn be wetted with another material, e.g., ferroelectrics.

Although 1D metallic nanotubes have significant application potential in different fields, few methods have been reported on the preparation of uniform metallic 1D structures. Up to now, two approaches to metallic 1D structures have been proven most successful: template synthesis and step-edge decoration. In the frame of template synthesis, macroporous membranes [49] and nanotubes [50, 51] have been used as sacrificial templates. Recently, a chemical process has been reported to synthesize Au, Ag and Pt nanowires [52]. The second method, step-edge decoration has been employed to synthesize molybdenum and some other metallic 1D structures [53, 54, 55]. Nonetheless, a versatile method is still required to produce mono-disperse metallic nanotubes or nanowires in a controlled manner. The goal lies not only in fabricating metallic nano- and microtubes of the desired materials and studying their properties, but also in making use of them as electrodes for other functional structures.

1.6 Organization of the thesis

The purpose of the present thesis is to investigate essential elements required for potential future prototypes of functional devices based on piezoelectric materials, such as a new mass storage device. This includes the fabrication and investigation of the different nano- and micro-elements necessary as well as a proposal of the primary composite functional structures based on these elements.

First of all, since the so-called template-wetting method, which is the method of choice in this thesis, exploits the basic phenomena of wetting, Chapter 2 gives an overview of the wetting theory. Not only general aspects are dealt with but also the specific aspects associated with: the physics underlying the occurrence of wetting within the confinement in the 1D cylindrical pores. The structure formation and tailoring of the morphology of the 1D nano- and micro-objects obtained from this specific wetting phenomena are addressed. Because these cylindrical pores are from the porous templates, the next chapter, Chapter 3, is dedicated to a detailed description of the fabrication as well as the materials properties of such porous templates, including porous alumina and macroporous silicon. We expect that the results of these investigations on the materials properties may have also implications for applications in the areas of sensors and opto-electronics.

Before the description on the fabrication and characterization of all the nano- and micro-elements, an experimental chapter, Chapter 4, describes all the methods used in the characterization, including scanning electron microscopy (SEM), energy-dispersive X-ray analysis (EDX), transmission electron microscopy (TEM), X-ray diffraction (XRD), differential scanning calorimetry (DSC), atomic force microscopy (AFM) and piezoresponse force microscopy (PFM).

In Chapter 5 and Chapter 6, the fabrication and the characterization of two core elements towards the assembly of a mass-storage device are described:

- Inorganic piezoelectric perovskite oxide tubes (Chapter 5) composed of materials including *PZT* and *BTO*. Besides the morphology and crystallinity, their piezoelectric property is also characterized by PFM on an individual tube on a local scale.

- Organic polymeric tubes (Chapter 6) composed of β -phase P(VDF-co-TrFE). Specific properties, such as temperature-induced phase changes, were measured by DSC, besides morphological, and crystalline properties. Piezoelectric switching as well as ferroelectric domain information is also shown by PFM on an individual nanotube.

The possibility to mount metal electrodes on the ferroelectric nano- and microtubes is depicted in the Chapter 7. A prototype of tri-layer tubes with tube-walls composed of metal/ferroelectrics/metal in radial direction consecutively is also shown in the same chapter.

The last chapter, Chapter 8, gives a summary and an outlook based on the results presented in this thesis. We expect that these basic elements as well as primary composite structures could potentially serve as the essential elements and a major trial step towards complex functional devices for data-storage in the future.

2. Exploiting wetting phenomena to tailor 1D nano- and microstructures

2.1 Wetting on a macroscopic scale

As a large part of the work in this thesis deals with wetting of porous materials, the phenomena involved in wetting are first discussed in this chapter. It entails a detailed discussion of the underlying physics even though a lot of open questions will remain unanswered.

2.1.1 Contact angle and Young's law

In the theory of classical capillarity of wetting phenomena, the interfacial tension γ_{ij} plays a key role. It represents the free energy necessary to increase by one unit the area of contact between two different phases i and j . The origin of this free energy can be understood physically as follows: Inside a dense phase, i , the molecules attract each other, and they can interact better with neighbors of the same species i when located in the bulk material than when located close to the interface to another phase j .

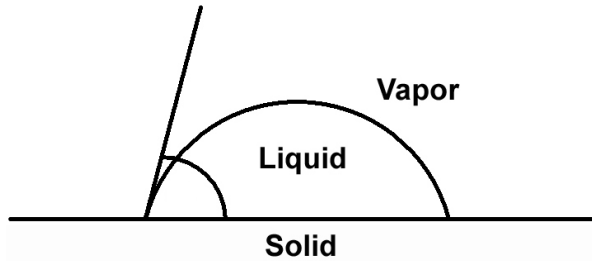


Figure 2.1: Schematic of wetting during the coexistence of three phases, respectively liquid, solid and vapor phases. The contact angle is denoted by θ .

Suppose we have a solid substrate S wetted by a liquid L in contact with a vapor V , as shown in figure 2.1. Three interfaces can then be distinguished: liquid-vapor, solid-liquid, and solid-vapor with the correspondingly associated free surface energies: γ_{LV} , γ_{SL} and γ_{SV} , respectively. In figure 2.1, a tendency is shown towards wetting rather than dewetting. Indeed, out of the two phases, liquid and vapor, the solid substrate prefers the liquid and disfavors the vapor. This can be seen from the spreading of the liquid on the solid substrate: the contact angle θ is less than 90° . Experimentally, the contact angle must be measured close enough to the wall, that is, within a few percent of the capillary length a_0 [56]. This length is a measure of the distance over which the liquid-vapor interface is curved, and results from the competition of surface tension and gravity. It is defined as [56]:

$$a_0 = \sqrt{\frac{2\gamma_{LV}}{g\Delta\rho}} \quad (2.1)$$

where g is the gravitational acceleration and $\Delta\rho$ is the density difference of liquid and vapor. Typical values of a_0 are of the order of one millimeter. Another point needs to be noted is that all the free energies are “far-field”, which means that these interfacial free energies act “sufficiently” far way from the region near the contact line of molecular dimensions.

In figure 2.1, it can also be figured out that, although the inequality $\gamma_{LS} < \gamma_{SV}$ applies, a direct solid-vapor contact is still tolerated. However, when the preference for adsorption of the liquid would be further increased (for example, by changing the temperature), the vapor may become excluded from contact with the solid. Then, a liquid layer will intrude between solid and vapor. This is termed *complete wetting*, whereas the situation in figure 2.1 represents *partial wetting*. The thickness of the liquid wetting layer in the case of complete wetting is typically a few hundred Å, as will be discussed in more details in section 2.2.2. The equilibrium surface free energy of the solid-vapor interface is consequently defined as

$$\gamma_{SV} \geq \gamma_{SL} + \gamma_{LV} \quad (2.2)$$

at complete wetting.

For partial wetting, on the other hand, the inequality applies:

$$\gamma_{SV} < \gamma_{SL} + \gamma_{LV} \quad (2.3)$$

which expresses that although a solid-liquid contact is preferred, a solid-vapor interface has lower free energy than the combination of solid-liquid and liquid-vapor interfaces. Balancing the components of these forces along the direction parallel to the substrate and perpendicular to the contact line (the vertical direction in figure 2.1) leads to [57]:

$$\cos \theta = \frac{\gamma_{SV} - \gamma_{SL}}{\gamma_{LV}} \quad (2.4)$$

The angle θ is the contact angle, as defined in figure 2.1. The equation 2.4 is also known as Young’s law. Note that the equation 2.4 can also serve as the thermodynamic definition of the contact angle, when the surface free energies are known, but no direct observation of θ is made. Clearly, complete wetting corresponds to $\theta = 0$. Young’s law needs to be generalized as soon as the surface tension of the interface between the two adsorbed phases is anisotropic. In the case of partial wetting, Young’s law expresses the mechanical equilibrium of the forces (per unit length) that the interfaces exert on the contact line along which they meet.

The contact angle given by Young’s equation is static, i.e., Young’s law applies to the equilibrium state of the system. However, if the three phase (liquid/solid/vapor) boundary is in actual motion, the angles produced are called *dynamic contact angles* and are referred to as “advancing” and “receding” angles, as shown in figure 2.2. The difference between “advanced” and “advancing”, “receded” and “receding” is that in the static case motion is incipient while in the dynamic case motion is actual. During its motion toward an equilibrium state, a liquid drop scans a range of dynamic contact angles. Dynamic contact angles may be determined at various rates of speed. Dynamic contact angles measured at low velocities should be equal to properly measured static angles.

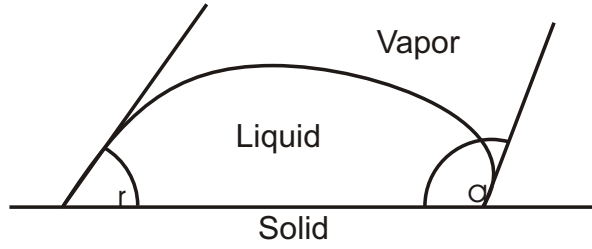


Figure 2.2: Side view of a sessile water drop on a solid surface showing advancing and receding contact angles (θ_a and θ_r).

2.1.2 Tanner's law

It is important to notice that the effect of body forces such as gravity on the contact line is vanishingly small and that, therefore, equation 2.4 is valid even in the presence of gravity or any other body force. Only such forces as viscous forces which might become increasingly large at the contact line can affect Young's law. In the case when the surface tension is the only driving force, Tanner's spreading law [58] is an approximated solution of the hydrodynamics of spreading.

Regard a nonvolatile liquid drop on a nonreactive smooth surface when inertial or viscoelastic effects are neglected. Furthermore, the drops are supposed to be small enough for the gravity to be negligible.

On a macroscopic scale, according to Tanner, a universal spreading equation, regarded as Tanner's law, reads [58]:

$$\frac{da}{dt} = v^* \theta^3 \quad (2.5)$$

where a is the radius of the liquid-substrate contact area and v^* a characteristic velocity, defined by

$$v^* = \frac{\gamma_{LV}}{\mu} \quad (2.6)$$

where μ is the viscosity of the spreading liquid.

As a result of equation 2.5, this model gives the radius a as a function of the time t in the complete wetting regime as $a \propto t^n$.

Tanner's law has also been obtained by de Gennes [57] from a balance between the viscous dissipation and the work done by the surface tension force. He uses a general equation that describes the profile of the droplet near the edge when the long-range forces are negligible. In this more general theory, the dependence of a on the droplet volume Ω is obtained by:

$$a \propto \Omega^m (v^* t)^n \quad (2.7)$$

with $n = 0.1$, $m = 0.3$.

Lopez *et al.* [59] have analyzed the situation, when gravity is the main driving force. They obtained a similar power law with $n = 0.125$ and $m = 0.375$. These theories are based on steady state arguments focusing on the edge of the film and using a lubrication approximation. Tanner [58] and Lopez [59] compared theories to experiments, finding good agreement in both cases. Hydrodynamic models, however, do not predict the dependence of n on a change such

as in temperature or in pH value which alter both the surface tension and the viscosity. The lack of a controlled experimental environment might therefore explain the range of observed values of n and m .

2.1.3 Spreading coefficient

If non-equilibrium situations are dealt with, we may have a solid/vapor interfacial tension γ_{SV} that is larger than $\gamma_{SL} + \gamma_{LV}$. The difference

$$S = \gamma_{SV} - \gamma_{SL} - \gamma_{LV} \quad (2.8)$$

is called the spreading coefficient.

The transition from partial to complete wetting can be discussed in terms of the equilibrium spreading coefficient S as follows. When S is positive, the spreading is energetically favored. The liquid spontaneously spreads and tends to cover the whole solid surface. Using Young's law (equation 2.4), we obtain:

$$S = \gamma_{LV}(\cos \theta - 1) \quad (2.9)$$

so that for partial wetting $S < 0$, and for complete wetting $S = 0$. The wetting kinetics can now be characterized by the way in which S tends to zero, or, equivalently, the way in which $\cos \theta$ tends to 1.

Up to now, all the situations aforementioned can be summarized in terms of contact angle as:

- complete wetting $\leftrightarrow \theta = 0$
- partial wetting $\leftrightarrow 0 < \theta < 90^\circ$
- partial drying $\leftrightarrow 90^\circ < \theta < 180^\circ$

From the values of bulk cohesive energy, there are two main types of solids: (a) hard solids (covalent, ionic, or metallic), which have a solid/vapor interfacial energy of γ_{SV} - 500 to 5000 ergs/cm² and (b) weak molecule crystals and organic liquids (bound by van der Waals forces, or in some special cases, by hydrogen bonds), which have a γ_{SV} - 50 ergs/cm² [60]. Most molecular liquids can have complete wetting on high-energy surfaces. This can be explained qualitatively as follows: The underlying solid usually has a polarity much higher than that of the liquid. In contrast, low-energy surfaces can also give rise to a partial or complete wetting. It depends on the surface tension of the liquid. For a complete wetting, there exists a "critical surface tension". Only when the surface tension of a chosen liquid is smaller than the critical value can a complete wetting happen.

2.2 Wetting on a microscopic scale

2.2.1 Role of the disjoining pressure

As mentioned earlier, if the spreading coefficient S is positive, spontaneous spreading occurs, and the equilibrium situation corresponds to a complete coverage of the solid by a thin liquid film. However, several measurements of the spreading kinetics of liquids on a large variety of

substrates seem to give spreading kinetics approximately independent of S , and the adequacy of a description based on interfacial energies and simple hydrodynamic concepts has been widely debated [61]. To solve this dilemma, Joanny and de Gennes pointed out the role of molecular long-range forces, which may result in the formation of a precursor film [57, 62]. They stated that when a film is very thin, long-range forces cannot be neglected. These forces may be electrostatic, steric, or van der Waals in nature. In this thesis, all the long-range forces are restricted to van der Waals interactions, which always exist between two atoms or molecules. The potential of interaction is attractive and decreases with intermolecular distance r as r^{-6} ; this is the so-called nonretarded regime. When this potential is integrated over all pairwise interactions between two half-spaces separated by a small distance e , one finds a slow decreasing potential¹ [63]:

$$W(e) = -\frac{A}{12\pi e^2} \quad (2.10)$$

where A is an effective Hamaker constant [64] which contains all non-geometric contributions to interaction, on the order of a few k_bT (where k_b is the Boltzmann constant and T is the absolute temperature), and e is the liquid film thickness. If A is positive, the interaction is attractive. As an example, A is always positive between two identical bodies, which explains why particles in solution generally flocculate.

In the case of a liquid film deposited on a solid surface, the two half-spaces are different (solid and gas, as shown in figure 2.3), and the Hamaker constant can be either positive or negative. In wetting conditions, A is negative: solid and gas repel each other through the liquid. The effect of long-range forces, that is, the disjoining pressure, Π , is then to make the liquid film thicker, since $W(e)$ has a minimum for an infinite liquid thickness ($e = \infty$). The sign of A can be determined from approximate combining relations [64]:

$$A \simeq A_{SV} + A_{LL} - A_{LV} - A_{SL} \quad (2.11)$$

where the A_{IJ} is Hamaker constant in general between media I and J (which could be either a liquid, vapor or solid), which is proportional to the product of the densities of phases I and J and to the product of their polarizabilities $\alpha_I\alpha_J$. Because the density of the gaseous phase is generally negligible, A is negative when the polarity of the solid is larger than that of the liquid. Therefore, a solid of high surface energy, such as metal or clean glass, should be wet by all the usual liquids.

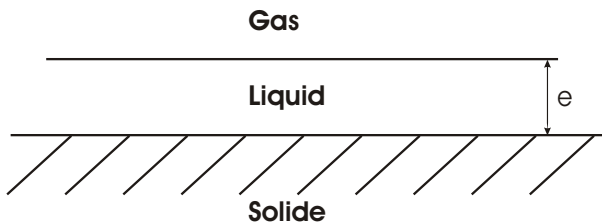


Figure 2.3: Wetting film on a planar solid surrounded by a gas.

2.2.2 Precursor films

For a complete wetting, precursor films may occur. They emanate from a macroscopic droplet and have a thickness e of a few tens of nm in the vicinity of the droplet, and a thickness

¹For thicker films ($e > 300\text{\AA}$), retarded effects must be considered and $W(e)$ decreases as e^{-3} .

smaller than a molecular monolayer at the microscopic spreading front. As shown in figure 2.4, the precursor film precedes the macroscopic spreading front all around the droplets, with a structure strongly dependent on the spreading coefficient S . If the wetting liquid is non-volatile (“dry spreading”), the only efficient transport of the liquid is by diffusion within the liquid. The precursor film, as depicted in figure 2.4a, forms when the intermolecular forces of attraction between the solid and liquid are sufficiently strong to create positive spreading coefficients and disjoining pressures. As it spreads, more and more material is drawn out of the macroscopic drop into the precursor film, as depicted in figure 2.4b. The submicroscopic structure and dynamics of precursor films depend on the spreading coefficient S and are affected by the local inhomogeneities in surface energy. In this microscopically almost flat precursor film, in which Laplace pressure is negligible, the thickness is governed by long-range forces and decreases towards the equilibrium state which might be either a pancake [57, 62] or a surface gas [65]. In case of pancake, the equilibrium thickness is $e \sim S^{-1/2}$ while in case of a surface gas, the thickness corresponds to a sub-monolayer because of a non-complete surface gas coverage.

As stated by de Gennes [57] and Joanny [62], long-range forces, for example, van der Waals forces, should be taken into account in the spreading phenomenon of precursor film. It is found that, at sufficiently short time, when the macroscopic droplet still acts as a reservoir, the behavior of the precursor film is diffusive and the radial extension (l) on macroscopic scale follows a universal time dependence (t) of the form:

$$l^2 = Dt \quad (2.12)$$

where D is the diffusion coefficient of the liquid within the precursor film. It is different from the conventional diffusion coefficient describing the random motion of particles in the bulk liquid phase or on solid substrates. As a matter of fact, D also depends on the driving forces which cause the film spreading.

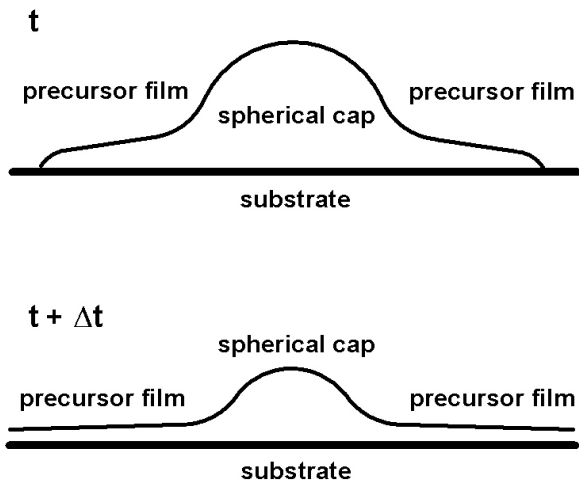


Figure 2.4: Formation of a precursor film during the wetting process of a polymer melt or liquid at time t and $t + \Delta t$.

In a microscopic drop, van der Waals forces are dominant. The following spreading equation stands for van der Waals driven spreading [66]:

$$R(t) = R_0 + v_r t \quad (2.13)$$

with $v_r = \frac{A}{2\mu a_c^k}$. A is an effective Hamaker constant with $A = \frac{B}{12\pi}$ and $k = 2$ for nonretarded van der Waals forces and $A = \frac{C}{9}$ and $k = 3$ for the retarded case, where B and C

are positive constants. a_c is a cutoff length for small values of h (which is the height of the geometrically spherical drop). The supposition that the drop is self-similar and has a spherical profile is justified for the case of the macroscopic drop, where droplet spreading is driven by the Laplace pressure. However, for van der Waals driven spreading, this is only an approximation. In particular near the contact line, it is known that van der Waals pressures deform the drop. Therefore, a_c is not a molecular length scale, but has a much larger value.

It was predicted that the final state of spreading should be a limited flat wetted spot with abrupt edges: a “pancake” [57, 62]. But in the case $S/\gamma_{LV} \geq 1$, the predicted pancake thickness falls in the range of molecular thicknesses: below 20\AA . One can expect the details of the structure to be strongly dependent on the *short-range forces*. One should stress also that *molecular diffusion*, which was not taken into consideration in de Gennes’ theory, is expected to ultimately destroy the pancake structure if it overcomes the film cohesion [67]. As a matter of fact, when diffusion takes over liquid cohesion, a droplet evolves by diffusion to reach a surface gas [65].

2.3 Wetting by liquid polymers

A polymer is a macromolecule composed of many repeating units of segments. The molecular weight M_0 of a monomer unit is typically between 50 g/mol and 100 g/mol , while the total molecular weight $M = nM_0$ can range from 1000 to above 10^6 . When in solution or molten, a polymer chain can adopt a number of configurations depending on the net segment-segment forces in the liquid. If these are weak, the polymer assumes the shape of an “unperturbed” random coil. An important length scale is the root mean square radius of the polymer coil. For an unperturbed coil, this is known as the *unperturbed radius of gyration* R_g [68], and is given by

$$R_g = \frac{l_e \sqrt{n}}{\sqrt{6}} = \frac{l_e \sqrt{\frac{M}{M_0}}}{\sqrt{6}} \quad (2.14)$$

where n is the number of segments and l_e the effective segment length. As an example, if $l_e = 1.0\text{ nm}$ and the segment molecular weight is $M_0 = 200$, then for a polymer of $M = 10^6$, R_g has a value of about 29 nm . However, the real volume of the chain is only a small fraction of the volume encompassed by R_g . Thus, if the segment width is about the same as the segment length l_e , the molecular volume is $\pi(l_e/2)^2 n l_e \sim n l_e^3$, while the volume encompassed by R_g is $\frac{4}{3}\pi R_g^3 \sim 0.3 n^{\frac{3}{2}} l_e^3$. The ratio of these volumes is $\sim \sqrt{\frac{n}{10}}$. Thus, for a polymer with $n = 1000$ segments, only about 1 % of the random coil volume is actually occupied.

According to sections 2.1 and 2.2, as nearly all liquids other than liquid metals have free surface energies of less than 75 ergs/cm^2 at ordinary temperature. They are allowed to spread spontaneously on “high energy surfaces” such as in organic oxides, silica and most metals. In the case of complete wetting, a sub-micrometer range “precursor film” of liquid spreads ahead of the macroscopically observable liquid edge. The spreading of polymers, which are low energy liquids with large dimension, was first investigated by Ausserré [69]. According to the precursor film profiles of spreading liquid drops studied by Léger *et al.* [70], the thickness profile of a polymeric precursor film decreases as the distance to the macroscopic droplet increases. In its vicinity, the thickness of the precursor film e has a mesoscopic value while at the microscopic spreading front it is below a molecular monolayer. At the microscopic spreading front, the thickness is smaller than the radius of gyration. As a result, individual molecular chains

move by surface diffusion in disentangled states. Glick *et al.* have observed the spreading of polystyrene drops on gold at elevated temperatures and have shown the spreading behavior to be qualitatively consistent with a theoretical picture where the drop acts as a reservoir for a spreading precursor film [71].

2.4 Wetting the walls of cylindrical pores by non-volatile liquids

2.4.1 Capillary rise

The motion of wetting liquid films in cylindrical pores is an important topic in this thesis. When placed inside a cylindrical pore of radius b , whether a liquid plug will spread or not depends on the spreading parameter S , as defined in equation 2.8. The energy (per unit volume) of the spreading liquid is [72]:

$$F_f = \frac{2\pi L(b(\gamma_{SL} - \gamma_{SV}) + (b - e)\gamma_{LV} + bP(e))}{\pi L(2eb - e^2)} \quad (2.15)$$

with $P(e)$ the long-range van der Waals interaction term ($P(e) = \frac{\gamma a^2}{2e^2}$ where $a^2 = \frac{A_{SL} - A_{LL}}{6\pi\gamma}$, A_{SL} and A_{LL} being the Hamaker constants related to solid-liquid and liquid-liquid interactions), while the energy of the unspread drop is

$$F_g = \frac{2\pi bl(\gamma_{SL} - \gamma_{SV})}{\pi b^2 l} = -\frac{2(S + \gamma_{LV})}{b} \quad (2.16)$$

At the drop-film transition, $F_f = F_g$ together with $\frac{\partial F_f}{\partial e} = 0$ gives:

$$S_c = \frac{3}{2}\gamma_{LV}\frac{a^{2/3}}{b} \quad \text{and} \quad e_c = a^{2/3}b^{1/3} \quad (2.17)$$

- When $S < S_c$, the drop will not spread (situation depicted in figure 2.5b) and partially wets the tube wall, forming an angle of contact (which can be equal to zero, unlike the contact angle of a drop on a planar surface).
- When $S > S_c$, the drop will spread and cover the interior of the pore, making a film (situation depicted in figure 2.5a) of thickness $e = a\sqrt{\frac{3\gamma}{2S}}$. The thickness results from a competition between spreading (expressed by S) and thickening long-range molecular forces (expressed by A) and usually has a value of molecular thickness. This thickness is so small that, even for tiny quantity of liquid, the film will usually coexist with a drop: the pressures of the drop and the film should be the same and this leads to a film thickness of e_c , i.e., the value at the threshold.

2.4.2 The pinch-off mechanism

In his article [73] on the experimental results of the infiltration of disordered glass capillary models consisting of channels with diameters of the order of 100 μm with water, Bernadiner described the so-called pinch-off mechanism, which leads to the filling of a capillary with a liquid.

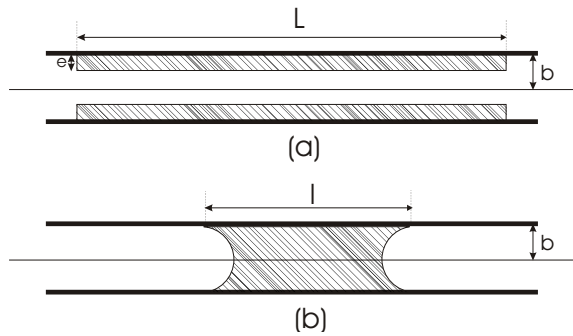


Figure 2.5: Side-view of a capillary tube wetted by a droplet of liquid: (a) a film of thickness e and length L is formed; (b) a drop of length l is formed.

The detailed analysis shows that the pinch-off mechanism consists of four consecutive steps, as shown in figure 2.6: “film flow”, “occurrence of instability”, “snap-off”, and “interface movement”, consecutively. Initially, water invades the individual capillary in the form of a thin film moving along the capillary channel surface. This film divides the cross section area of the capillary channel into two layers, water and air. The increase in the thickness of the water layer caused by inflowing water results in the formation of a neck at the air/water interface. Ultimately, the neck snaps, forming two air/water interfaces across the capillary channel. As water continues to flow in the capillary channel, the capillary channel fills up with water, and the interfaces travel in opposite directions along the capillary channel and eventually invade the adjacent pores, forming stagnant boundaries of residual air.

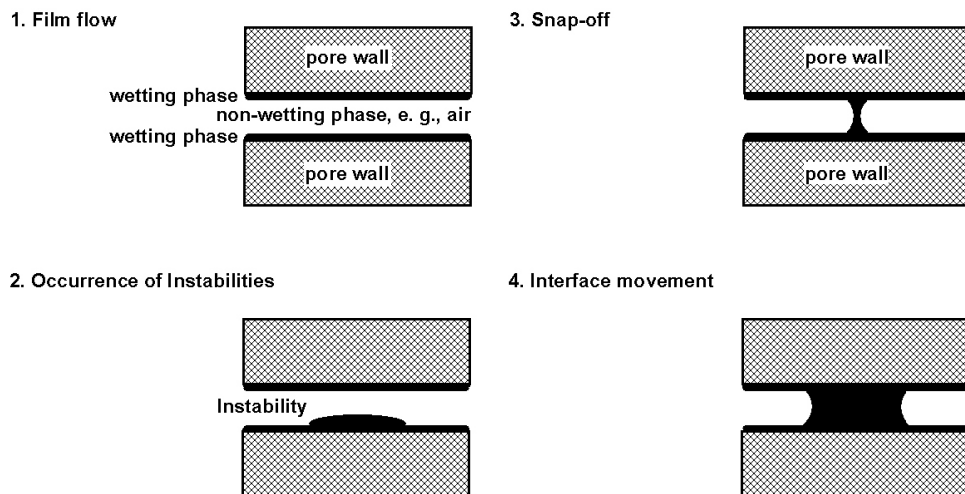


Figure 2.6: The pinch-off mechanism for the formation of the internal front microstructure in capillary with four consecutive stages: (a) film flow; (b) occurrence of instability; (c) snap-off and (d) interface movement.

2.4.3 Rayleigh instability

Joseph Plateau (1801-1883), a Belgian physicist also known for his work on soap films, was the first to study the instability of cylindrical films [74]. Plateau understood that the instability of these films is driven by the liquid surface tension. When the free surface of a liquid cylinder undulates with a wavelength λ , its area decreases [75], provided that λ is larger than the circumference of the cylinder ($2\pi R$ for a liquid jet of radius R , or $2\pi b$ for a film of thickness e on a fiber of radius b for $e \ll b$). Although the observed longitudinal curvature of the film should oppose the growth of the instability, the curvature associated with the cross-sectional

area of the column, which is larger than the longitudinal curvature, actually governs the growth of the instability. The Laplace pressure is higher in the troughs than in the crests and thus the instability can develop.

In a series of papers [76] written between 1878 and 1892, Lord Rayleigh revisited and extended the work of Plateau. He showed that the instability of cylindrical films is established with a well-defined wavelength, and thus explained the regularity in spacing of the drops that form. The observed wavelength simply corresponds to the fastest growing mode and, for a thin film coating a fiber of radius b , being $2\pi\sqrt{2}b$, about $10b$.

For a polymeric solution which has higher molecular weight than usual liquids, the condition $S > S_c$ is satisfied. The polymer melt can spread over the interior of the pore walls. As stated earlier, when a liquid polymer is spreading on a solid high surface energy substrate, at microscopic spreading front the diffusion is realized by disentangled polymer chains, which suffer long-range forces, mainly van der Waals interactions. Because of the small value of the thickness of the precursor film, the wetting can be stabilized by the long-range van der Waals forces [77]. That means, for the wetting of high molecular weight polymer solutions, Rayleigh instability is suppressed after the generation of the very thin precursor films. If the wetting film has an intermediate thickness, linearly saturated instabilities occur. In the case of thick wetting films, Rayleigh instabilities grow corresponding to a certain extent to the mechanism found by Bernandiner [73].

2.5 Wetting of surfaces with critical mixtures

When wetting occurs with critical mixtures (i.e., mixtures what could be either mixed or decomposed on temperature T , pressure P or volume V), there is an interplay between wetting phenomena and the decomposition. In this context, critical point wetting and surface directed spinodal decomposition are discussed. These structure formation processes may be exploited to generate functional morphologies as in the case of platinum microtubes (c.f. Chapter 7).

2.5.1 Critical point wetting

In his paper [78], Cahn used only three equations and less than one column of text to show that if two phases, say fluid A and fluid B , approach a critical point in the presence of a non-critical phase C , then before the critical point is reached, one of the fluid phases completely wets the non-critical phase, and there is no contact between C and the other fluid phase. His argument was based on the thermodynamic stability condition, that the three surface energies obey the inequality:

$$|\gamma_{BC} - \gamma_{BC}| \leq \gamma_{AB} \quad (2.18)$$

He observed that the right hand side of this inequality vanished at the critical point as $(T_c - T)^{2\nu}$, where ν is the critical exponent, and he made the reasonable conjecture that the left hand side vanished as $(T_c - T)^3$. With the known values of the critical exponents $\nu \approx 0.65$, the inequality must become an equality before $(T_c - T)$ vanishes; hence a transition from non-wetting to wetting must occur as one approaches the critical point within the two-phase region of the phase diagram.

2.5.2 Surface-directed spinodal decomposition

Working with polymers has some benefits to unveil the spinodal phase decomposition, including the observation of the ripening of the phase structure and the time dependence of the size of individual domains. In the presence of a substrate, i.e., a non-critical matrix phase, this has been well exemplified by the surface-directed spinodal decomposition in polymer blends [79]. Spinodal decomposition, when occurring in the bulk, refers to spontaneous growth of concentration fluctuations with specific period [80]. This results in the generation of a near-ordered phase morphology on decomposition. The occurrence of halos on light scattering is caused by this near order. The halos represent the most frequent distance in the system. The period grows because of the ripening. The driving force for this is the reduction of the interface area between the co-existing phases. In the presence of viscous polymers, this Ostwald ripening process is so slow that it can be monitored with conventional methods. The system can be frozen by the solidification of the polymers at specific stages. This makes polymer extremely suitable to study the basic mechanism. The freezing at different stages also gives the possibility to generate specific morphologies required for corresponding applications.

However, in the presence of external surfaces, the separation process of the phases is directed by the external surface [81, 82]. In this process, phase separation dynamics does not proceed isotropically as it would in the bulk. Following the theoretical prediction by Ball and Essery [83], the first experimental observation of a “surface-directed spinodal decomposition” was reported by Jones and co-workers [79]. They studied spinodal decomposition of mixtures of poly(ethylenepropylene) (PEP) and perdeuterated poly(ethylenepropylene) (d-PEP) near the surface. Composition waves with wave vectors normal to, and which propagate inwards from, the surface have been found, which maintain coherence for several wavelengths. If the multi-component system is confined, the phase morphology is strongly affected by substrate/film and film/air interfaces, as well as by confinement effects [84]. As a result, layered structure composition waves emanating from both interfaces interfere. The basic features of surface directed (micro-) phase separation in immiscible polymer systems have been presented in [79]. It was found that highly-ordered multilayered structures that extend over a large number of microdomains before a higher entropy state of disordered bulk domains occurs. The effect of finite film thickness on the kinetics of spinodal decomposition in a film thickness range where a transition from three-dimensional bulk-like to near two-dimensional kinetics was investigated by Sung *et al.* [85]. Below a certain threshold thickness, 2D phase structures where the domains penetrate through the whole film thickness, instead of layered structure, occur. Theoretical studies of the wetting behavior of two-phase systems confined inside cylindrical pores were proposed by Liu *et al.* [86]. Three configurations, respectively tubes, capsules, and plugs were proposed depending on the cylindrical pore radius, molecular length and temperature. It was also stated in the article that for small pores, there is a direct transition between plugs and the tube, while for larger pores there is an intermediate capsule regime. The formation of tubes and capsules correspond to the wetting while that of plugs to non-wetting.

2.6 Structure formation processes during the wetting of porous materials with polymeric liquids

2.6.1 Adaption of wetting phenomena from flat substrates to porous templates

Wetting phenomena described above are the key to template wetting for the preparation of 1D nano- and micro-objects. Organic polymers are among the materials with low surface energy [60, 87]. A polymeric melt or solution can be loaded with considerable proportions of low molar mass compounds. When a polymer-containing liquid is brought into contact with or a polymer melt is molten onto the surface of a porous membrane, wetting of the pore walls occurs while individual chains diffuse onto and along the pore walls as depicted in figure 2.7a. As a prerequisite, the pore walls must have a high surface energy. The processes discussed here are microscopic in nature, in contrast to phenomena such as the Lotus effect [88], which are associated with the macroscopic wettability of structured surfaces. Then, a mesoscopic precursor film will wet the walls of the pores in a similar manner to the formation of a precursor film on a flat substrate (figure 2.7b).

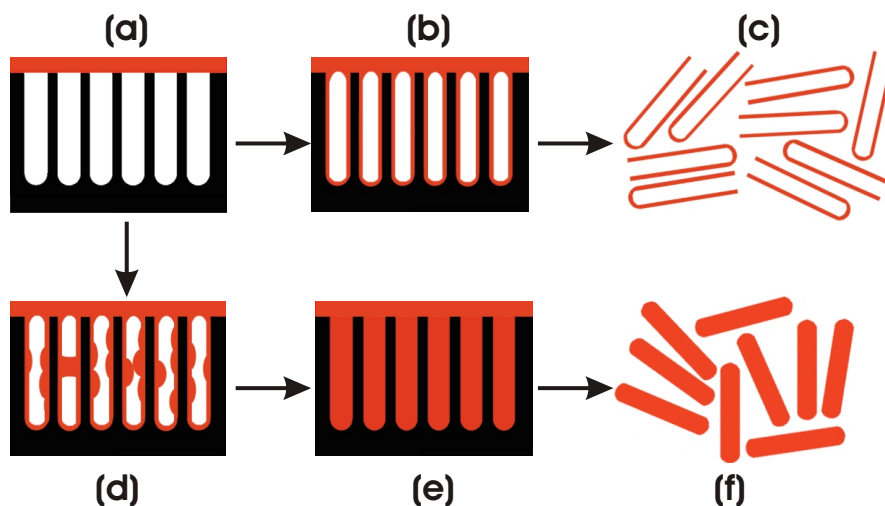


Figure 2.7: Wetting process of porous templates with polymer-containing liquids. (a) The fluid is brought into contact with the templates and covers the pore openings. (b) Within a certain time, the pore walls are covered by a mesoscopic film of the liquid. (c) Polymeric nanotubes obtained by selectively removing the template. (d) Formation of a meniscus in the case of wetting by nonpolymeric solutions. (e) Complete filling of pores. (f) Nanowires obtained by selectively removing the template.

In case of the spreading of liquids on flat substrates, the area to be wetted can be regarded as infinite and the liquid reservoir as finite. In case of pore wetting, however, the area to be wetted is finite, and the liquid reservoir infinite. If disordered liquids, for instance, molten homopolymers, are in contact with a porous material whose pore walls possess a sufficiently high surface energy (c.f. figure 2.7a), the wetting may occur as follows: at first, individual disentangled polymer chains diffuse on the pore wall. After a certain coverage has been reached, relaxation processes should occur. Both entropic relaxation (the polymer chains lying flat on the pore walls have an entropically unfavorable conformation), and the disjoining pressure that promotes a thickening of the wetting film could play a role. Typically, the walls of the thus-obtained tubes have a wall thickness of a few tens of nm, i.e., corresponding to the radii of gyration of typical polymers (c.f. figure 2.7b). This indicates that the tube walls consist of a

monolayer of macromolecules. The occurrence of Rayleigh instabilities (c.f. figure 2.7d), which is to be expected for liquid cylindrical films, is obviously suppressed. Eventually, the entire process may be frozen by the solidification of the polymeric layer. This can be accomplished by the evaporation of a solvent or thermal quenching, leading to vitrification or crystallization. Note that solid fibres are obtained if the diameter of the template pores is decreased below twice the wall thickness of the tubes.

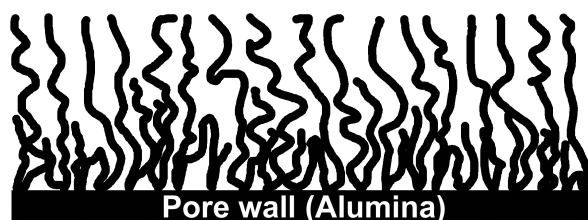


Figure 2.8: Absorption layer of polymer molecules on the inner pore walls of porous templates with a high surface energy. All the molecules are in direct contact with the pore walls, thus preventing the attractive interaction of the pore walls with another layer of the same material.

A point to note here is whether the final equilibrium state corresponds to a complete filling of the pore volume. If the diameters of the pores are much larger than the molecule size of the polymers, a complete filling (c.f. figure 2.7e) can only happen, if it occurs at all, at a completely different time scale, which is much longer than the time needed for wetting. This can be explained by the unusually large dimensions of the polymer molecules.

With polymer melts as well as polymer solutions the pore walls are completely wetted, with complete reproduction of the pore structure even for pore depths (T_p) of $100 \mu m$. The liquid film solidifies when cooling or evaporation of the solvent leads to crystallization or vitrification. By selectively removing the templates, polymeric nanotubes (c.f. figure 2.7c) or nanowires (c.f. figure 2.7f) can be obtained.

Figure 2.9 depicts pore openings from the top of a macroporous silicon membrane that has been wetted by a homogeneous layer of PMMA-DR1 (poly(methyl methacrylate) with disperse red-1 side-chains). It is clear that the interior of the pore has not been filled completely, but only the pore walls coated by a polymeric layer homogeneously.

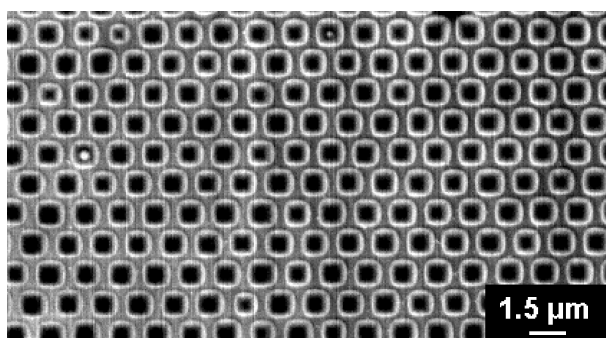


Figure 2.9: SEM image on the top of PMMA coated macroporous silicon. The pores are open with a visible layer of PMMA-DR1 which measures around 80 nm.

2.6.2 Occurrence of Rayleigh instabilities

The situation is very different in the case of template wetted by nonpolymeric liquids, in which the molecular weight as well as the size of the molecules is very low compared to that of polymers. As stated earlier, complete filling occurs in such systems thus leading to the formation of rods of low molar mass compounds. If a porous template is wetted by a nonpolymeric solution or an oligomeric solution, long-range intermolecular interactions lead to a wetting film consisting of many molecular layers on the pore walls as a result of the disjoining pressure. As

only a small fraction of the molecules is in direct contact with the pore walls, such multilayers are obviously more amenable to the occurrence of Rayleigh instabilities than macromolecular monolayers having the same thickness. This could lead to a formation of a meniscus, and is speculated to trigger the occurrence of Rayleigh instabilities described in section 2.4.3. This possibly leads to a complete filling of the pores after a certain time (c.f. figure 2.7d), similar to the mechanism observed by Bernadiner [73] (c.f. section 2.4.2).

In figure 2.10, the SEM pictures of PZT nanoshell tubes, which are obtained from an oligomeric precursor (figure 2.10a) and a mixture of the same oligomeric precursor with a polymer poly(*D,L*-lactide) (PDLLA) (figure 2.10b), are shown. The difference in the contrast corresponds to different wall thicknesses. It can be seen in figure 2.10a that the wall thickness is not homogeneous along the direction of the tube axis, but has an undulated morphology. This is because the precursor used is an oligomer with relatively low molar mass instead of a polymer with higher molecular weight. The wetting film on the pore walls consisting of the precursor-oligomer obviously had a thickness where linearly saturated Rayleigh instabilities occur (c.f. section 2.4.3). However, this undulation can be eliminated if a mixture of the oligomer and a polymer is used as the precursor. As shown in figure 2.10b, the wall thickness becomes homogeneous.

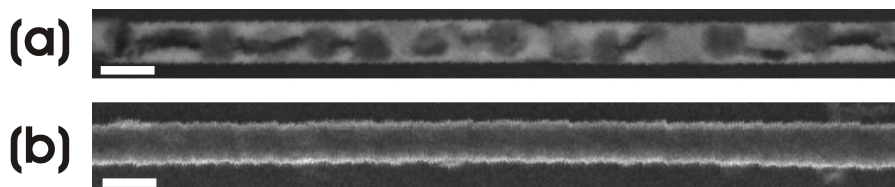


Figure 2.10: (a) Occurrence of Rayleigh instabilities within a PZT nanoshell tube wall along the tube axis due to the low molar mass precursor used (b) Rayleigh instability is suppressed after the low molar mass PZT precursor is mixed up with a polymer poly(*D,L*-lactide) (PDLLA). The scale bar in both images represents 1 μm .

2.6.3 Tailoring the morphology of the tube walls

A polymer in the form of a melt is placed on the porous templates at a temperature well above the glass transition point in the case of amorphous polymers, or well above the melting point in the case of partially crystalline polymers. The polymeric melt rapidly covers the pore walls. Alternatively, polymeric solutions may be dropped on the templates at ambient conditions.

As the pores are blind each with a capped end, the wetting layer has a tubular form which is an exact replica of the pore shape. A thermal treatment is usually necessary to get different target structures with desired materials and morphology:

- In case of oligomeric precursors contained in the tube walls to get inorganic ceramic tubular structures such as PZT or BTO nano(shell) tubes (c.f. Chapter 5), a first step of thermolysis at relatively low temperature at 300 °C converts the oligomer into the target materials, but in an amorphous phase. Then, a second annealing step at higher temperature (600 °C ~ 850 °C) crystallizes the target materials within the tube walls into the perovskite phase.
- In case of pure polymeric melts such as the copolymer P(VDF-co-TrFE) (c.f. Chapter 6), which has the advantage that no pyrolysis is needed, thus avoiding the by-products during the process, porous templates wetted by a polymer are heated to a temperature above the

melting point in case of partially crystalline polymers. Then, cooling the sample to room temperature at specific cooling rates allows for a precise control of the crystallization process. The confined crystallization leads to the formation of specific textures of the tube walls.

- In case of organometallic precursors as used in the 3-component mixture $CHCl_3/Pt(acac)_2/PDLLA$ (c.f. Chapter 7), a first step of demixing by the evaporation of solvent ($CHCl_3$) leads to the coexistence of PDLLA-rich and $Pt(acac)_2$ -rich phases (as described in figure 2.11a and figure 2.11b as well as in section 2.5.2). Then, a pyrolysis converts the Pt(II) into Pt(0). A final ripening process (as described in figure 2.11c) is needed to get closed Pt layers forming the tube walls whereas only distinct Pt particles are obtained without this process.

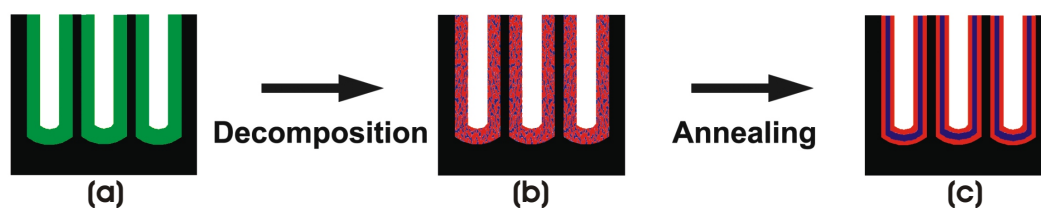


Figure 2.11: Formation of inorganic nanotubes within porous template via wetting by polymeric precursors: (a) formation of multi-component nanotubes; (b) decomposition by evaporation of solvent; (c) Ostwald ripening resulting in the growth of the crystallites of target materials with adjustable morphology sandwiched between two polymeric layers.

2.7 Summary of the chapter

In this chapter, wetting phenomena, which serve as a theoretical starting point for the rest of the thesis, are reviewed. First of all, wetting is described on a macroscopic scale. Important parameters such as spreading parameter and contact angle are explained in view of the Young's law. Then, on a microscopic scale, wetting is depicted by the existence of a thin precursor film as a result of the existence of long-range forces such as van der Waals interactions. Special features of polymers, such as variable chain lengths, small density fluctuations, and slow motions of long chains, open a new window on the classical wetting theory. Especially by wetting of polymers within confined geometry, new features can be obtained.

Then this general theory underlying wetting phenomena is adapted to a more specific case: wetting of porous templates, which entails the coexistence of polymer or polymeric solutions and a high surface energy pore walls, in order to fabricate functional 1D nano- and microstructures. This new approach is called *template wetting*. Important features such as structure formation, occurrence of Rayleigh instabilities, and tailoring of the morphology of the finally obtained tubes during the template-wetting process are described in details. A brief experimental procedure is sketched via phase separation and crystallization of targets materials within the polymeric matrix wetting the pore walls. Further detailed descriptions in the next chapters on the fabrication as well as characterization of 1D nano- and micro-objects with specific target materials are based on this chapter.

3. Ordered porous templates

In the frame of this thesis, porous templates including porous alumina and macroporous silicon were used to generate 1D nano- and micro-structures by the so-called template wetting method, as described in Chapter 2. Both of these two types of templates have properties which make them suitable for the template-wetting method which can be depicted briefly as the ability of one material (especially a liquid) to spread on/in the other materials (especially a solid). These properties include:

- High surface energy at the inner pore walls: This is a prerequisite to conduct the wetting or infiltration of liquid materials, which can be solidified in the pores so that 1D nano- and micro-objects are conserved.
- Controlled morphology: Well-arranged air pores in porous alumina or macroporous silicon can be realized in a precise way. The pore diameter range is covered from 15 nm up to several micrometers as indicated in figure 3.1. The length of the pores can reach 100 μm while still being highly ordered all along the pores in a regular fashion with a very low dispersity of less than 2 %.

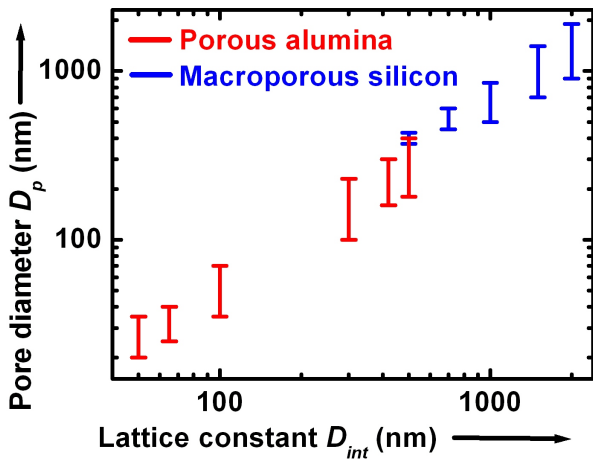


Figure 3.1: Overview of the pores diameters (D_p) and lattice constant (D_{int}) of the currently available highly ordered templates of porous alumina (red bars) and macroporous silicon (blue bars) [89].

- Easy fabrication: With existing technologies, these templates can be fabricated in large quantities using established techniques. The fabrication methods will be briefly described in the next two sections.
- Possible integration in already existing systems: These porous materials possess highly ordered hexagonal or orthogonal arrays of air pores with very high aspect ratio (which is defined as pore-length/pore-diameter ratio). Such arrays, after being coated by other specific target materials, can find their applications in the integration of oxide or metal nanostructures with technologies such as Si technology. The periodicity greatly helps in terms of addressing/registration for device applications. For example, macroporous silicon with hexagonally arranged air pores possessing periodicity in either in-plane and/or out-of-plane direction can open a photonic forbidden band gap, provided that the ratio of the pore radius r over inter-pore distance D_p is carefully chosen [90]. Integrated with

such functional photonic structures, 1D nano- or microstructures might find their devices applications in information manipulations by photons.

Functional 1D nano- and micro-objects either released or as hybrid material within templates have such advantages as: perfect alignment, rendering channels with functionalized walls, and eventually, functional membranes can also be obtained. The first step towards such functionalization lies in the investigations of porous template properties, including their optical and dielectric properties as well as wall chemistry. Such studies are important for applications like sensors, optical/electronic building blocks, etc.

In the following two sections, the materials properties of ordered porous alumina and macroporous silicon, which will be used as the templates for the generation of nano- and microstructures, will be discussed.

3.1 Porous alumina templates

3.1.1 Disordered pore arrays

Anodization of aluminum (Al) in aqueous electrolytes is governed by drift of the anions and cations in the applied electric field and the rate equations at the two interfaces: at the metal/oxide interface Al is oxidized, at the oxide/electrolyte interface oxygen is reduced and a porous alumina film is formed [91].

The pore formation mechanism is schematically displayed in figure 3.2. At the beginning of the anodization, the barrier film, which consists of non-conductive oxide ($= 10^{10} \sim 10^{12} \Omega \text{ cm}$ [92]), covers the entire surface of the aluminum (regime 1 in figure 3.2). The electric field is locally focused according to the fluctuations of the surface (regime 2 in figure 3.2). This leads to field-enhanced or/and temperature-enhanced dissolution in the formed oxide and thus to the growth of pores (regime 3 in figure 3.2). Since some pores stop growing at specific points due to competition among the pores, the current decreases. Finally, the current density j_p stays constant at an equilibrated state. In this stage, pores grow in a stable manner. However, it is observed very often that during the stable pore growth, the current density continues to decrease slightly. This is due to diffusion effects in the long pore channels [93].

The growth of disordered pore domains has been studied in details and a unique relationship between anodization voltage U and interpore distance D_{int} was found:

$$D_{int} = d + 2\alpha U \quad (3.1)$$

where d is the diameter of the pores, α is a proportionality constant of approximately between 2.5 and 2.8 nm/V .

3.1.2 Pore arrays with polycrystalline degree of order

The method discovered by Masuda *et al.* relies on self-ordering of the pores after a first-anodization step if the anodization properties meet the 10 % porosity rule [95, 96]. The driving force for self-assembly has been attributed to mechanical stress caused by the repulsive force between neighboring pores during anodization. Several previous studies revealed that self-ordered

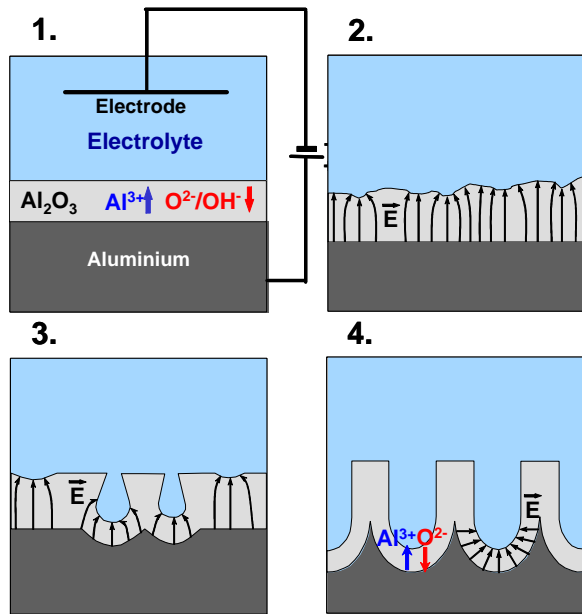


Figure 3.2: Schematic diagram of the pore formation at the beginning of the Al anodization. Regime 1: formation of barrier oxide on the entire area; regime 2: local field distributions caused by surface fluctuations; regime 3: creation of pores by field-enhanced or/and temperature-enhanced dissolution; regime 4: stable pore growth [94].

porous alumina structures can only be obtained under specific conditions. For example, structures with interpore spacing of 50, 65, 100, 420 and 500 nm can be fabricated at 19 V and 25 V in sulfuric acid, at 40 V in oxalic acid, and at 160 V and 195 V in phosphoric acid, respectively [93], as depicted in figure 3.3.

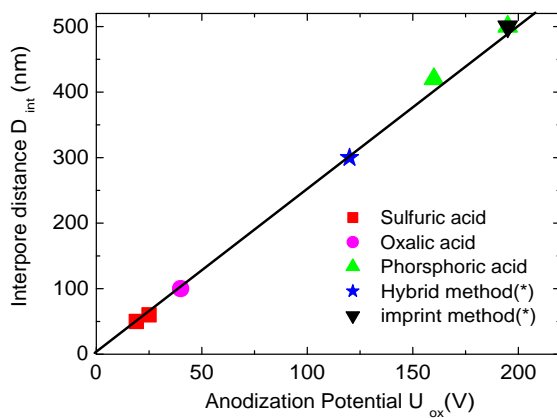


Figure 3.3: Interpore distance as a function of the applied potential during the anodization of porous alumina. The known self-ordering regimes are shown as symbols. The line is a fit to the data with a proportionality constant α of 2.5 nm/V (see equation 3.1) [93].

3.1.3 Monodomain porous alumina obtained by nanoimprint lithography (NIL)

In this section, the fabrication of monodomain porous alumina by means of nanoimprint lithography will be briefly introduced. This method uses a master stamp [97, 98] to initiate the growth of pores in alumina substrate which consists of Si_3N_4 pyramids with a height of 260 nm and a lattice constant of 500 nm (as shown in figure 3.4).

Figure 3.5 shows monodomain porous alumina with a 500 nm interpore distance and a 100 μm length formed by anodization of pre-patterned aluminum (purity: 99.99 %) at 195 V in 0.1 M phosphoric acid for 10 h. The structure shows a defect-free array and straight channels, demonstrating that it can possess outstanding optical properties such as photonic bandgaps. In principle, monodomain porous alumina on a cm^2 scale can be fabricated by this imprint method.

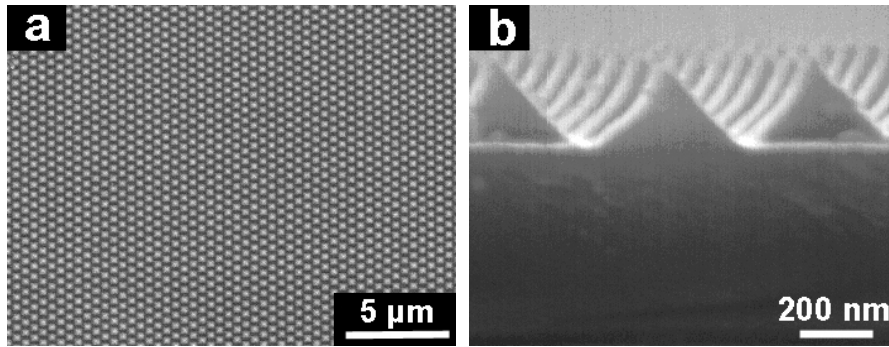


Figure 3.4: SEM image of the imprint master stamp consisting of Si_3N_4 pyramids with a 500 nm lattice constant and a 260 nm height: (a) top and (b) cross-section views of the imprint master stamp [97].

The details of the porous alumina structure are very similar to those shown by reference [96]. In figure 3.6, one can see that the inner oxide layer near the cell boundary is about 50 nm thick. The outer oxide layer lies between the inner oxide layer and the air pore. In fact, the inner oxide layer is known to be composed of pure alumina oxide, whereas the outer oxide layer has impurities such as incorporated anions [99]. The definition of the inner oxide and the outer oxide in porous alumina is analogous to that in barrier-type alumina where the inner oxide and the outer oxide exist adjacent to aluminum and the electrolyte, respectively. An investigation on the optical properties of the porous alumina [100] revealed the inhomogeneous distribution of the anions in the both inner and outer oxide alumina pore walls.

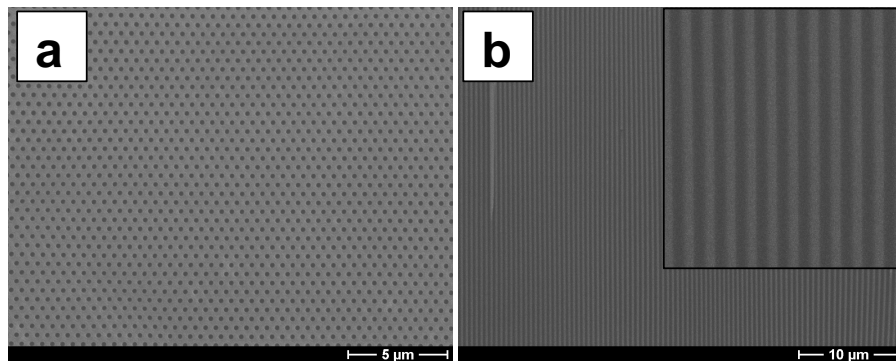


Figure 3.5: SEM image of perfectly-ordered porous alumina fabricated by anodization of pre-patterned aluminum (purity: 99.99 %) at 195 V in 0.1 M phosphoric acid for 10 h [97]: (a) surface and (b) cross-section views of porous alumina. The interpore distance is 500 nm corresponding to the lattice constant of the imprint master stamp. Monodispersity of the channel diameter is highlighted in the inset of (b).

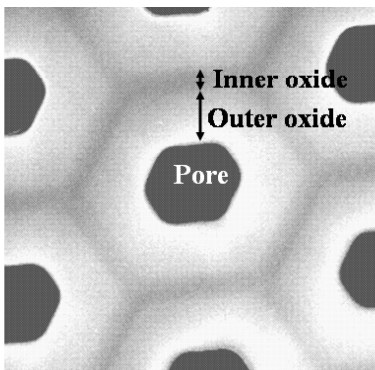


Figure 3.6: TEM image of an ordered porous alumina array obtained by imprint lithography and subsequent anodization (195 V , $0.1 \text{ M H}_3\text{PO}_4$). The duplex oxide layers consisting of an inner oxide and an outer oxide are visible. The thickness of the inner oxide is always 50 nm , whereas that of the outer oxide decreases with increasing the pore diameter (initial diameter : 180 nm) by isotropic etching [96].

Optical characterization of monodomain porous alumina as 2D photonic crystals

Periodic dielectric materials allowing to control the flow of light are classified as photonic crystals (PCs) [90]. Due to their low absorption coefficient, excellent thermal stability and easy handling, porous alumina structures could be potential materials for PCs in the visible and infrared ranges which are both out of the their electronic bandgap of $7 \sim 9.5 eV$ (correspondingly $130 \text{ nm} \sim 177 \text{ nm}$ in wavelength). In the following, the definition of PCs will be briefly reviewed first and then followed by a detailed description of those based on porous alumina. The measured reflectivity will be compared with theoretical predictions. Moreover, a distribution of anions in the duplex oxide layers of the porous alumina wall to explain the optical properties is suggested accordingly.

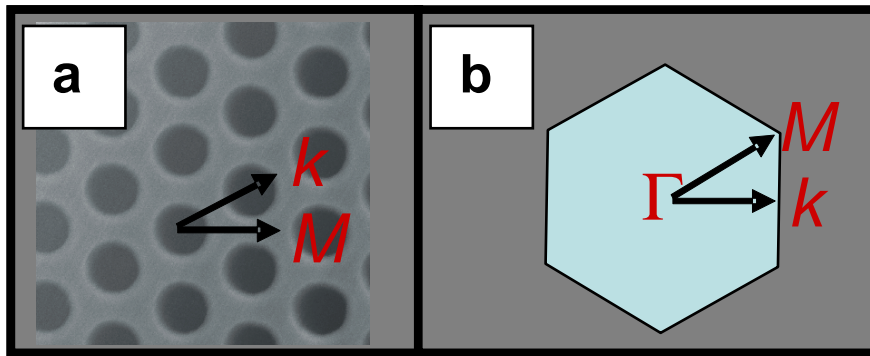


Figure 3.7: Hexagonal lattice (a) in real lattice space; (b) in reciprocal space. The high-symmetry directions Γ - M and Γ - K are indicated in both real and reciprocal spaces.

The definition of the photonic bandgaps is borrowed from that of the bandgaps in solid-state physics. In a crystal, the interaction between the periodically arranged atoms and electrons moving through its periodic lattice results in the formation of allowed and forbidden energy states, determining the electronic properties of crystals.

Similarly, we can consider photons moving through a dielectric material with a periodic potential. If the absorption of the light by the material is negligible and the contrast in refractive index between the two regions is high enough, light can not propagate in certain directions with specified energies due to the existence of photonic band gap.

In the configuration interesting us, a PC is composed of hexagonally arranged air holes in a dielectric matrix. The corresponding photonic band gaps are determined by the configuration (geometry and spacing) of air holes and the contrast in refractive indices. The size of a photonic bandgap is determined by the refractive index contrast and by the filling ratio¹ of the higher-index material. The location of the gap is determined by the lattice constant. For example, the wavelength of light lying within the photonic band gaps can be roughly estimated by the spacing between the air holes (or the lattice size) times the sum of refractive index of the dielectric materials [90].

Before optical characterization, porous alumina membranes are prepared by selective etching of aluminum in a CuCl_2 -containing solution. Afterwards, the membranes are cleaved mechanically and well cleaved planes are confirmed by SEM. For the optical characterization, the reflectivity of the porous alumina structures with different pore radius/interpore distance-values

¹ = surface area of a pore/surface area of a unit cell

are measured along $\Gamma - M$ direction (figure 3.7) with Fourier Transform Infrared (FT-IR) Spectrometer (Bruker, IFS 66) equipped with a UV-CaF₂-beamsplitter, a tungsten lamp, and a MCT detector.²

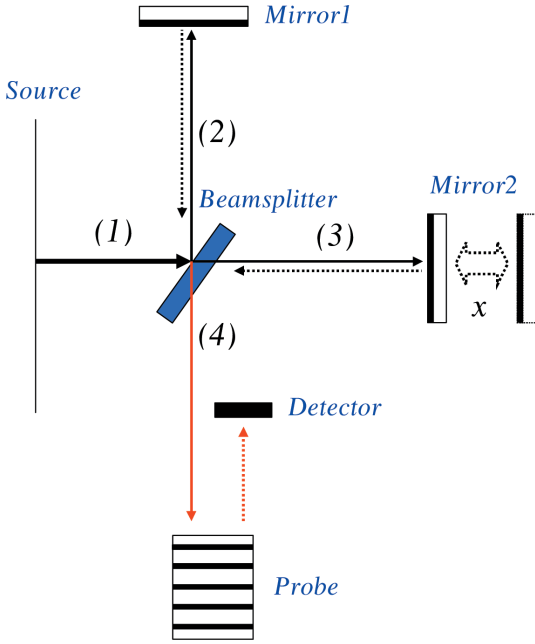


Figure 3.8: A scheme of the Michelson interferometer.

The underlying principle of the reflectivity measurement with the FTIR microscope is based on a Michelson interferometer and Cassé-grain method. The Michelson interferometer consists of a beamsplitter, a fixed mirror (Mirror 1), and a translatable mirror (Mirror 2) as sketched in figure 3.8. The beam radiated from the source (beam 1) is separated into two beams by the beamsplitter: half of the radiation is reflected to the fixed mirror (beam 2) and the other half is transmitted to the moving mirror (beam 3). The fixed and moving mirrors reflect the beams back to the beamsplitter. Again, half of this reflected beam is transmitted and the other half is reflected at the beamsplitter, resulting in one beam passing to the detector (beam 4) and the second back to the source.

The optical path difference (Δ_p), which is defined as the difference between the beams travelling through the fixed and moving mirrors, is

$$\Delta_p = 2 x n \cos(\delta) \quad (3.2)$$

where x is the moving mirror displacement, n is the index of refraction of the medium filling the interferometer arms, and δ is the angle of the inclination of the beam relative to the optical axis. For a normal beam ($\cos(\delta) = 1$) and for the air medium ($n = 1$), Δ_p can be deduced as $2x$. The net optical path difference $\Delta (= \Delta_p + \Delta_r$, where the equivalent path difference arising from phase change on reflection, Δ_r , is π due to two external reflections in the case of beam 2, whereas only one for beam 3.³ If $\Delta = m\lambda$ or $(m + \frac{1}{2})\lambda$ (where m is an integer), constructive or destructive interference of the two beams is produced, respectively, for every $\lambda/2$ translation of one of the mirrors [101].

An interferogram⁴ of a signal is collected as a function of the optical path difference. Afterwards, the spectrum is obtained by performing a Fourier Transform (FT) on the interferogram

²(HgCdTe) photoconductive detector. This fast detector is suitable for measuring the infrared radiation.

³A relative phase shift of π occurs by reflection of the light going from a lower index toward a higher index, the so-called external reflection.

⁴The name of the signal format acquired by an FTIR spectrometer.

as a function of wavelength. The measurement with the FTIR spectroscopy is performed twice with and without the sample present. The signal originating from the sample is calculated from the difference between the two computed spectra.

To measure the reflectivity of the sample, the Cassé-grain method is employed as shown in figure 3.9 in which the angular aperture of the IR-objective is indicated as 30° .

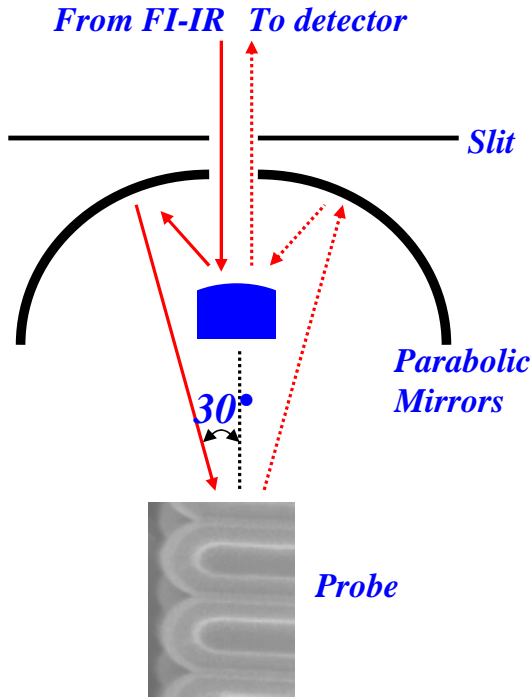


Figure 3.9: Cassé-grain mirror objective in the FTIR microscope.

A background measurement is performed on a silver mirror as a reference prior to the actual measurements.

The reflectivity of the porous alumina structure with different values of the r/D_{int} ratio was measured along the Γ -M direction. The measurement was carried out on a cleavage plane after the alumina structure had been broken carefully. As described earlier, the porous alumina structure has duplex oxide layers with different dielectric constants. As a result, the effective dielectric constant of the whole structure is not a constant for different values of r/D_{int} ratio. In particular, we will see later that the outer oxide layer has a nonhomogeneous effective dielectric constant depending on the concentration of impurities at different parts of the pore walls.

As indicated in [96], for the lattice constant $D_{int} = 500 \text{ nm}$, the porous alumina structure is only composed of the inner oxide layer when the pore radius $r \geq 200 \text{ nm}$. Therefore, we first measured the reflectivity of a sample with $r/D_{int} = 0.4$ which is composed of only inner oxide. Note that we have taken into account the fact that pore shapes are hexagonal but not perfectly round.

Figures 3.10a, b and c show the reflection spectra in the Γ -M direction for the porous alumina with $r/D_{int} = 0.4, 0.24$ and 0.18 , respectively. The stopgaps⁵ of TE polarization in Γ -M direction for these three r/D_{int} ratios are $0.96 \mu\text{m} - 1.20 \mu\text{m}$, $1.17 \mu\text{m} - 1.36 \mu\text{m}$ and $1.28 \mu\text{m} -$

⁵Complete (Full) photonic bandgap: bandgap in all directions and for both polarizations; Photonic bandgap: bandgap in all directions and for one polarization; Photonic stopgap: bandgap in one direction and for one polarization.

1.41 μm , respectively. Figure 3.11 shows that stopgaps of the TM polarization exist only in the Γ -M direction for all r/D_{int} ratios.

Table 3.1: Literature survey of refractive index, n , of alumina. Here, we assume that the dielectric constant of alumina, ϵ , is equivalent to n^2 due to a low absorption coefficient in the visible and infrared ranges.

Authors	Refractive index n	Conditions
K. Huber [102]	1.65	unknown
G. Hass [103]	1.67 - 1.62 @ $\lambda = 0.3 - 0.6 \mu\text{m}$	3% Ammonium tartrate
S. Nakamura <i>et al.</i> [104]	1.64 @ $\lambda = 0.546 \mu\text{m}$	4.25% Phosphoric acid (140 V)

For both polarizations, the dielectric constant of the inner oxide is deduced by the position and width of the maximum reflection (photonic stopgap in Γ -M direction) compared to the theoretical calculation for different supposed values of refractive indices. The dielectric constant of the inner oxide, ϵ_{inner} , is determined by the bandstructure calculation which matches best the measured reflection in the porous alumina with $r/D_{int} = 0.40$. Here, ϵ_{inner} is estimated around 2.8 for both E- and H- polarization, which is in a good agreement with the previously reported dielectric constant of pure aluminum oxide (table 3.1). Note that among the three dispersion relations (figure 3.10d, e and f) for TE mode, a bandgap in all direction is opened for $r/D_{int} = 0.40$ and $r/D_{int} = 0.24$. The dispersion relation for $r/D_{int} = 0.18$ does not open a bandgap in all directions, but a stopgap in the Γ -M direction.

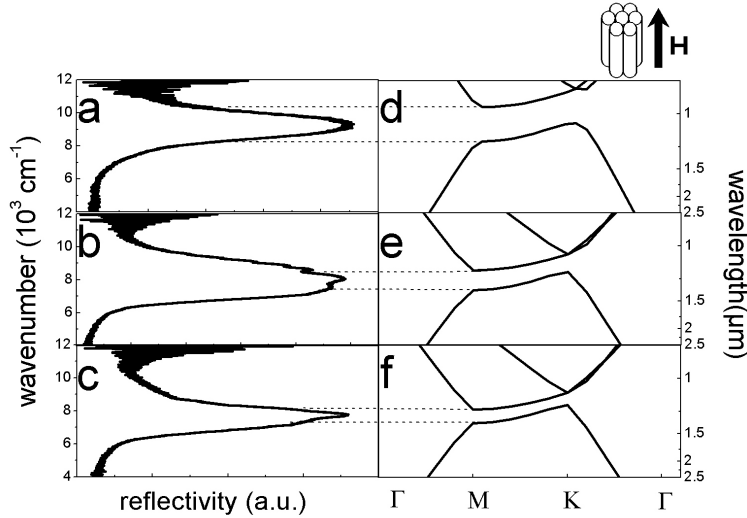


Figure 3.10: Comparison of the reflectivity measurements and bandstructure calculations of porous alumina (Γ -M direction, TE (H)-polarization) for different values of r/D_{int} ratio: (a) $r/D_{int} = 0.4$; (b) $r/D_{int} = 0.24$; (c) $r/D_{int} = 0.18$; (d), (e), and (f) are corresponding bandstructure calculations of (a), (b), and (c), respectively.

In figure 3.12, the measured reflection spectrums of alumina PCs with $r/D_{int} = 0.4$ in Γ -M direction for both polarizations are compared to calculation by the *Translight* package [105]. For both E- and H- polarization, the bandgap positions observed in the measurement are in a good agreement with the calculated ones. In addition, for the TE mode, more than 90 % reflectivity within the stopgap is observed, indicating very low losses and high quality structures. For the TM mode, a slight blue shift on the high frequency side implies a stronger angular dependence of the E-polarization since the IR-objective has an angular aperture of 30° .

After determining the refractive index of the inner oxide, a series of reflectivities of both polarization for different values of the r/D_{int} -ratio, representing the different thicknesses of the outer oxide layer, are measured. For each polarization, bandstructures are calculated for every value of r/D_{int} with a series of dielectric constants of the outer oxide, taking into account that the porous alumina structure has duplex oxide layers. As shown in figure 3.13a, the duplex porous

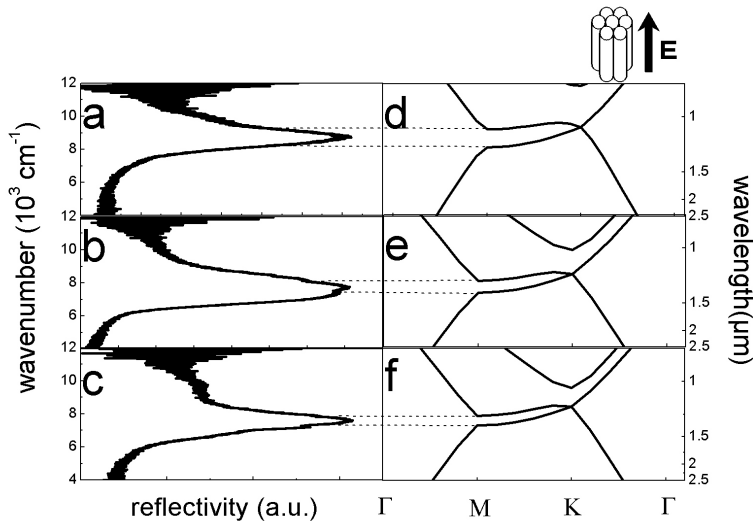


Figure 3.11: Comparison of the reflectivity measurements and bandstructure calculations of porous alumina (Γ -M direction, TM (E)-polarization) for different values of r/D_{int} ratio: (a) $r/D_{int} = 0.4$; (b) $r/D_{int} = 0.24$; (c) $r/D_{int} = 0.18$; (b), (e), and (f) are corresponding bandstructure calculations of (a), (b), and (c), respectively.

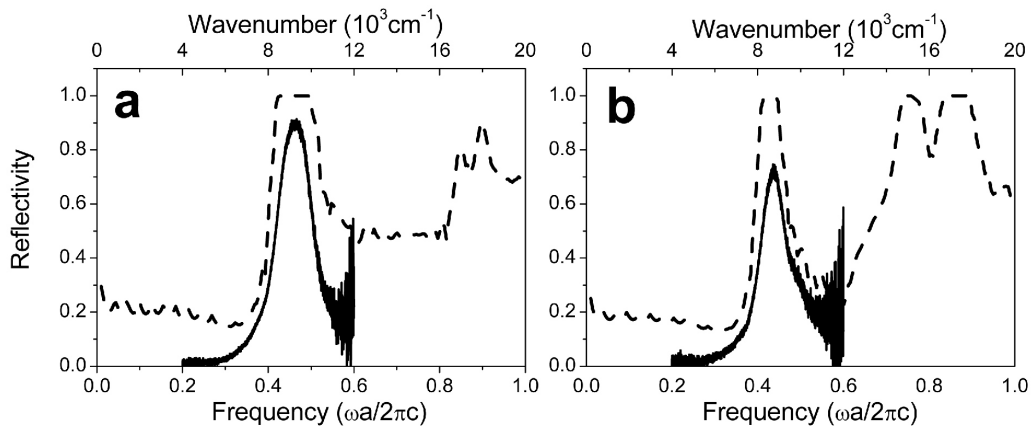


Figure 3.12: Reflectivity measured using an FTIR microscope (solid lines) and calculations computed by the transfer matrix method (dashed lines) in case of $r/D_{int} = 0.4$: (a) TE (H-) polarization and (b) TM (E-) polarization.

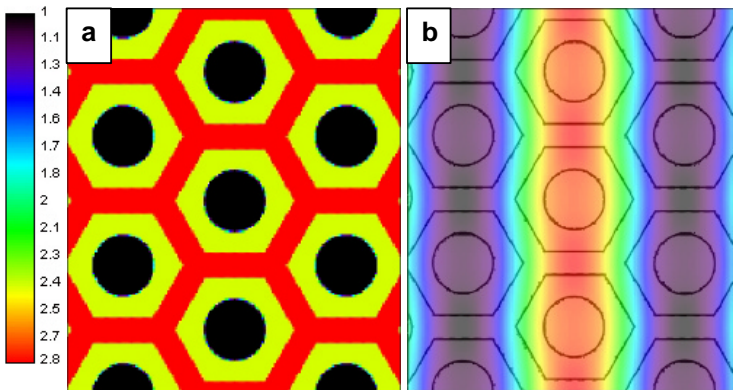


Figure 3.13: (a) Distribution of the dielectric constant for the theoretical calculation in which different values of dielectric constants are shown in the left scale bar. (b) The corresponding H-field distribution of the TE mode at the M -point of the air band of the fundamental bandgap.

alumina structure is composed of dielectric constants of the air pores ($\epsilon = 1$), the outer oxide layers (non-uniform values of ϵ , e.g., 2.4 ~ 2.7), and the inner oxide layers ($\epsilon \simeq 2.8$), which are represented by the black, yellow, and red colors, respectively. The corresponding magnetic field distribution at the M -point of the fundamental dielectric band is shown in figure 3.13b. The color indicates the amplitude of the magnetic field. Note that this mode has the tendency to concentrate most of its displacement energy in the high ϵ -area in order to lower its frequency. Since the displacement field is largest along the nodal planes of the magnetic field, the light blue regions are where the displacement energy is concentrated. These regions represent the alumina part, especially the inner oxide layer.

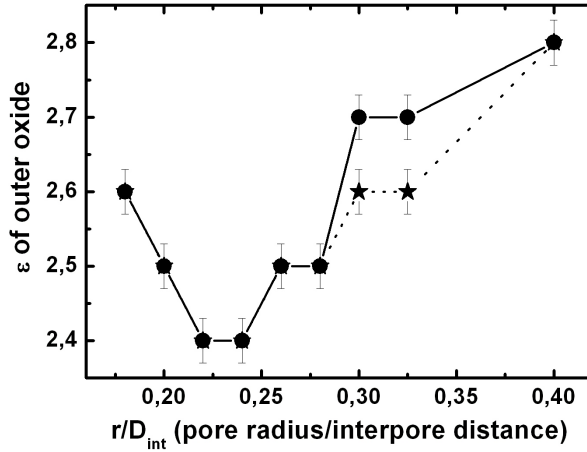


Figure 3.14: Effective dielectric constant of the outer oxide as a function of the r/D_{int} value (\star : TE mode and \bullet : TM mode). Note that the points where $r/D_{int} = 0.4$ represent the dielectric constant of the inner oxide.

For each polarization, the value of the supposed dielectric constant taken in the calculation which gives the best fitting to the measured bandstructure is selected as the effective refractive index of the outer oxide. This effective dielectric constant in the outer oxide, $\epsilon_{\text{eff,outer}}$, is not a constant for different r/D_{int} values. As shown in figure 3.14, for a value of the r/D_{int} -ratio between 0.18 and 0.33, $\epsilon_{\text{eff,outer}}$ varies from 2.6 to 2.4 and then to 2.6 for the TE mode, from 2.6 to 2.4 and then to 2.7 for the TM mode. Note that when the r/D_{int} value is between 0.28 and 0.40, the $\epsilon_{\text{eff,outer}}$ is different for E- and H- polarizations. This reveals the birefringence of the porous alumina structure.

Figure 3.15 shows the gapmap of the first stopgap positions in Γ - M direction calculated by MIT package [106] as well as measured by the FTIR microscope. The agreement between theory and measurement is very good. As the ratio r/D_{int} increases, the bandgap edges for both polarizations shift to higher frequency. The bandgap widths also increase due to the higher dielectric contrast of the whole structure. In figure 3.15a, the hatched area shows the calculated photonic bandgap frequency range for the TE mode. The maximum gap-midgap ratio⁶ is 9.73% for $r/D_{int} = 0.40$. The bandgap frequencies are higher compared to the results in reference [89]. This is due to the facts that the real structure of the porous alumina consists of the duplex oxide layers and that the interface between the two oxide layers has a hexagonal instead of a round shape.

In fact, Masuda *et al.* reported that stopgaps for both polarizations in the porous alumina PCs with $r/D_{int} = 0.18$ are observed, which are in a good agreement with theoretical predictions assuming a dielectric constant of 2.8 [108]. Note that if we take 2.8 as dielectric constant of the inner oxide and 2.6 as dielectric constant of the outer oxide, the effective dielectric constant of the whole oxide structure is only slightly lower than the value used by Masuda *et al.* [108].

⁶It is the ratio of $\frac{\Delta\omega}{\omega_0}$, where $\Delta\omega = \omega_c - \omega_v$. ω_v and ω_c are the lower and upper band edge frequencies of the gap, respectively. ω_0 is the midgap frequency. This parameter is dimensionless and independent on the scale of the

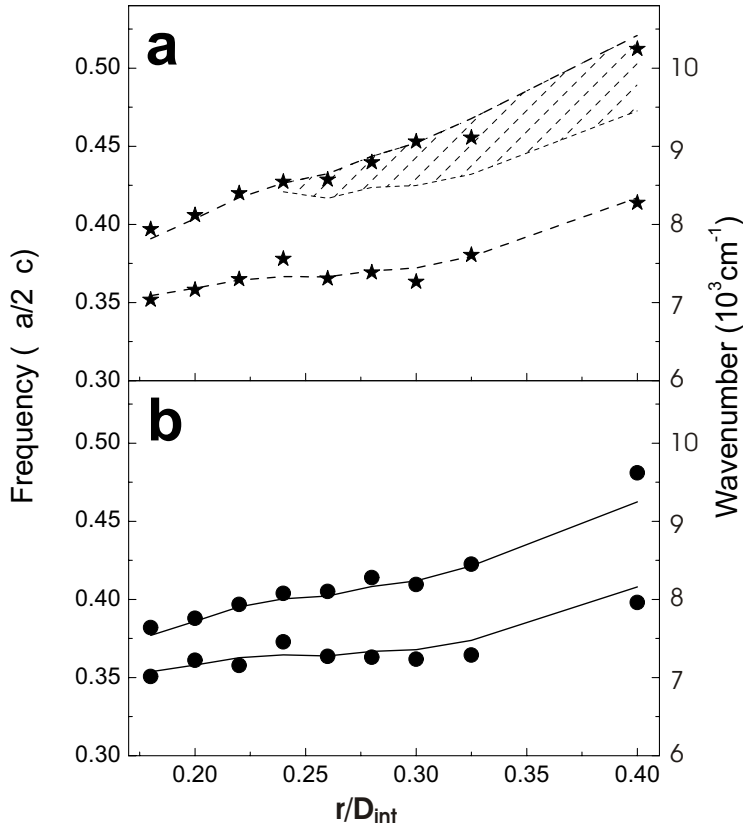


Figure 3.15: Maps of stopgaps as a function of the ratio r/D_{int} . (a) The TE-mode: stars (*) indicate stopgap from the reflectivity measurements in Γ -M direction. Dashed lines correspond to theoretical calculations of the stopgaps. The hatched area indicates the theoretical photonic bandgap in all in-plane directions which is deduced from bandstructure calculations. (b) The TM-mode: dots (•) represent the stopgap from the reflectivity measurements in Γ -M direction. The calculated stopgaps are shown in solid lines. Note that there is no photonic bandgap in all in-plane directions for the TM mode due to the low dielectric constant contrast between alumina and air.

Table 3.2: Possible alumina minerals with the different refractive indices [109]. n_α , n_β , and n_γ are the three coordinate axes in the order of least, intermediate, and greatest index.

Name	composition	Refractive index	Density(g/cm^3)
Wavellite	$\text{Al}_3(\text{OH})_3(\text{PO}_4)_2 \cdot 5\text{H}_2\text{O}$	$n_\alpha=1.527$ $n_\beta=1.535$ $n_\gamma=1.553$	2.36
Augelite	$\text{Al}_2(\text{PO}_4)(\text{OH})_3$	$n_\alpha=1.574$ $n_\beta=1.576$ $n_\gamma=1.588$	2.70
Gibbsite	$\alpha\text{-Al}(\text{OH})_3$	$n_\alpha=1.57$ $n_\beta=1.57$ $n_\gamma=1.59$	2.42
Diaspore	$\beta\text{-AlO}(\text{OH})$	$n_\alpha=1.694$ $n_\beta=1.715$ $n_\gamma=1.741$	3.4
Boehmite	$\alpha\text{-AlO}(\text{OH})$	$n_\alpha=1.64$ $n_\beta=1.65$ $n_\gamma=1.66$	3.44
Corundum	$\alpha\text{-Al}_2\text{O}_3$	$n_\alpha=1.761$ $n_\beta=1.769$	3.97

The inhomogeneities of the dielectric constant within the outer oxide layer might be explained by the nonuniform distribution of anions in the outer oxide layer. Several possible alumina minerals with different refractive indices could be considered as listed in table 3.2.

Compared to the dielectric constant of the pure alumina, the anion-incorporated alumina minerals have lower dielectric constants. The more anions are incorporated in the alumina, the lower the dielectric constant. In addition, as the degree of hydration, i.e., the amount of coordinated water, decreases, the corresponding refractive index increases. The density of the materials is increased in a similar way, so that the change in the effective dielectric constant can be attributed to a density modification. For example, for both augelite and wavellite containing phosphorus, the refractive index is similar to or smaller than that in hydrated alumina oxides. It is reasonable to assume that anion complexes containing phosphorous are concentrated in the intermediate part (c.f. figure 3.16). This region corresponds to the minimum dielectric constant in figure 3.14. As the anion-contamination decreases towards the inner oxide layer and the outermost oxide layer, the effective dielectric constants for both regions increase. This interpretation is in line with a model for the porous alumina structure suggested by Fukuda and Takahashi *et al.* [110, 111, 112, 113]. According to their model, the pore wall of porous alumina consists of an inner oxide layer composed of pure alumina and an outer oxide layer. The outer oxide layer again consists of an outermost oxide part and an intermediate oxide part. Takahashi *et al.* claim that the mobility of PO_4^{3-} is responsible for the nonuniform anion concentration [110, 111, 112]. Adsorbed anions, for example, PO_4^{3-} , OH^- and O^{2-} , are pulled into the alumina walls acting as negative electrode by the electric field. Since the size of the phosphate is larger than that of the other anions, the adsorbed PO_4^{3-} migrates more slowly compared with OH^- and O^{2-} . The phosphorus anion complex is trapped in the intermediate part since the attracting force in the intermediate part is weaker than that in electrolyte/outermost oxide interface. As a result, PO_4^{3-} is concentrated in the intermediate part of the outer wall.

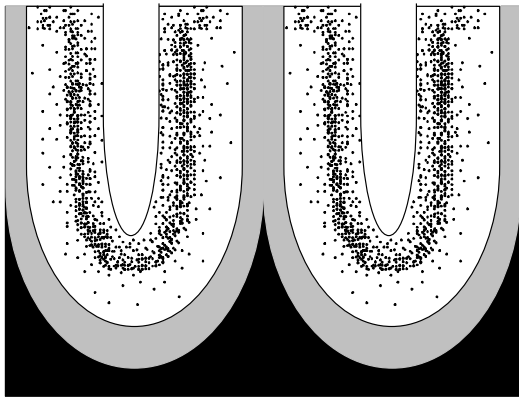


Figure 3.16: Schematic diagram of porous alumina oxide layers consisting of inner oxide and outer oxide. Anions (black points) are enriched in the intermediate part of the outer oxide. Note that the inner oxide in the center of the hemispheric scallop of barrier layer is twice as large as that in the edge of hemispheric scallop of the barrier layer or in the wall.

3.2 Macroporous silicon templates

Since the first successful preparation of macroporous silicon in the early 1990s [114], very regular pore arrays with a pore size of the order of $1 \mu\text{m}$ and a domain size up to wafer size have been obtained by photolithographic pre patterning. The so-obtained hexagonally arranged air pores in silicon are called macropores in contrast to micropores with a sponge-like structure with nanometer features and such properties as efficient photo-luminescence in the visible

photonic crystal [107].

range. The macroporous silicon can be either p-type or n-type, as described in the following two paragraphs.

p-type porous silicon

Porous silicon formed by anodization of p-type silicon in hydrofluoric acid has been studied widely [89]. Three different pore formation regimes as a function of the dopant concentration have been experimentally observed. For degenerately doped p-type silicon, a special type of mesopores has been observed experimentally and attributed to tunnelling of holes through the space-charge region. Their size is typically in the range of 5 to 50 nm. For moderately doped p-type silicon, micropore formation is observed with pores in the range of 2 nm – 5 nm. For highly resistive crystalline and amorphous p-type silicon (the resistivity is typically larger than 10 Ωcm), macropore formation (0.4 μm to 10 μm in diameter) is observed below a thin layer of micropores. Depending on the current density of HF concentration, these macropores can either grow in the current-limited regime (low-currents) or in the crystallographic regime (high-currents). To obtain ordered arrangements of pores for some applications such as photonic crystals, the crystallographic regime is typically used. A p-type silicon wafer with (100) orientation is first prepatterned by standard photo-lithography. Subsequent alkaline etching produces inverted pyramids acting as initial pores. Etching starts selectively at these etch pitches when self-ordering conditions and lithography match.

n-type porous silicon

In n-type silicon, holes (necessary for the dissolution reaction) are minority carriers so that they have to be generated by backside illumination. Then, they diffuse to the etch front through the wafer to promote dissolution of silicon, mainly at the pore tips. This technique has high requirements on the minority carrier diffusion length so that normally float-zone (FZ) wafers are used. Due to the fact that in this technique the holes move by diffusion and not by drift as in the p-type case, the strong boundary condition of a fully depleted pore wall is relaxed and thicker walls can be obtained up to 10 times the space-charge region width [89]. It is even possible to change the pore diameter during pore growth, which is hardly possible with p-type silicon in a controlled manner. To obtain ordered arrangements of pores, a n-type silicon wafer with (100) orientation is first prepatterned by standard photo-lithography. Subsequent alkaline etching produces inverted pyramids acting as initial pores. Under anodic bias and backside illumination, the wafer is then etched in hydrofluoric acid. As a result, pores grow straight along the (100) direction with a very high aspect ratio. The arrangement of these pores can be controlled by the lithographic mask and the pore diameter by the illumination intensity. By controlling these parameters, interpore distances in the range of $a = 500 \text{ nm}$ to a few tens of microns are possible. Figure 3.17 shows SEM images on the top-surface and cross-section views of a porous silicon sample having a photo-lithographically-defined hexagonal pore arrangement. It has an interpore distance of 1.5 μm and a depth of 100 μm .

3.3 Summary of the chapter

In this chapter, the fabrication process and physical characterization of two different ordered porous templates, respectively porous alumina and macroporous silicon, used in the template-wetting process have been described. Porous alumina structures can not only serve as sacrificing

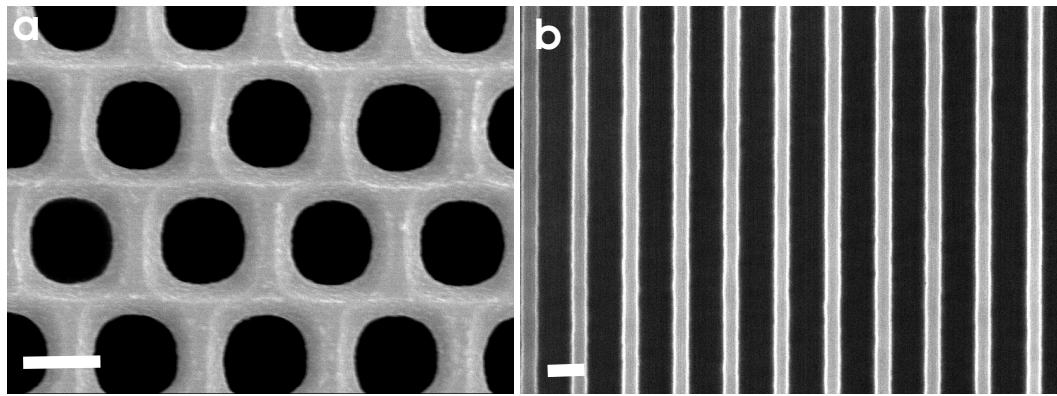


Figure 3.17: SEM images of perfectly-ordered n-type macroporous silicon of both (a) surface and (b) cross-section views. The interpore distance is $1.5 \mu\text{m}$. The scale bar in both images represents $1 \mu\text{m}$.

template for the fabrication of nano-objects within their channels of pores, but also possess surprising materials characteristics such as the coexistence of two oxide layers and optical features such as the existence of photonic bandgaps.

4. Experimental details

4.1 Preparation of tubes or wires from porous templates

As described in Chapter 2, 1D nano- or microtubes can be formed within the porous templates. The detailed preparation procedures of inorganic ferroelectric tubes are described in Chapter 5, of organic P(VDF-co-TrFE) tubes in Chapter 6 as well as metallic Pt and multi-layer tubes in Chapter 7. In order to study the morphology and application potentials of these structures, it is necessary to get released tubes or wires as powders or free-standing tubes or wires with one end embedded in a support. In case of macroporous silicon templates, they can be dissolved in a strong base such as aqueous potassium hydroxide (KOH). In the case of porous alumina templates, the selective etching can be realized via a controlled process by using solutions of either a base such as KOH , or an acid such as H_3PO_4 . The details are listed below:

- In case of macroporous silicon as template matrix, it can be etched with 30 – 40 wt % KOH at 60 °C for 30 to 40 minutes. To prepare arrays, we glued the wetted templates on conducting copper substrates prior to the removal of the matrix material using a conductive glue. The arrays could be handled with tweezers and thus be washed by immersing them into liquids. To remove residual KOH , the solution was washed several times with diluted hydrochloric acid, deionized water, and ethanol successively. To obtain released tubes as a powder, we removed the residual material on the top of the template prior to etching. We moved the wetted templates into cuvettes filled with aqueous KOH . The resulting suspension within the cuvettes was centrifuged after the complete decomposition of the matrix material. Then, the lye was removed with a syringe. The powder samples were washed by adding deionized water and ethanol. After centrifuging, the liquids were separated from the precipitation consisting of tubes with target materials. Finally, they were prepared as ethanolic suspensions which can lead to further characterizations. To prepare free-standing tubes or wires with one end fixed to the macroporous silicon template, a relatively shorter etching time, on the order of 5 – 10 min, was applied. Then, the whole wafer was immersed into de-ionized water to remove the residual KOH before further characterization.
- In case of porous alumina as template matrix, the underlying aluminium was first removed by dipping the whole sample into $CuCl_2 + HCl$ solution. After washing carefully the remaining alumina membrane, it was etched with 5 wt % H_3PO_4 solution for 10 hours in a beaker. Because of the interactions among the polymeric nanotubes, they still agglomerated as a membrane in the solution even after the complete removal of the alumina template. Then, the H_3PO_4 solution could be replaced by de-ionized water carefully until the pH value of the solution reached 7. A shaking of the beaker made the aggregation of the tubes disappear and a homogeneous suspension formed containing tubes with target materials and could be characterized further.

4.2 Characterization methods of 1D micro- and nanostructures

4.2.1 Electron microscopy

The first method to characterize the overall morphology of the nano- and micro-objects with different parameters was by electron microscopes, including scanning electron microscope (SEM) and transmission electron microscopy (TEM). As the tubes and wires could be obtained in desired forms, e.g., either free suspending in de-ionized water or in ethanol, or free-standing from a template, different investigation methods concerning the electron microscopes, as listed below, were explored to study their morphology:

- SEM (Scanning Electron Microscopy, *JSM-6300F*) with its basic unit consisting of an electron optical column mounted on the main console, a control and display system, a power supply unit, and a pump box. The main console incorporates a vacuum system, and the control and display system incorporates the control panels, keyboard, and display system. Tubes in different forms can be investigated directly under a SEM provided that they are attached to a highly conductive substrate, such as a doped silicon wafer or copper substrate. For the observation of non-conductive materials such as copolymer P(VDF-co-TrFE), low acceleration voltages, e.g., $1.5\text{ eV} \sim 5\text{ eV}$, are used in order to avoid severe electron charges at the sample surface. For inorganic and metallic tubes or wires such as PZT, BTO or Pt, higher acceleration voltages, e.g., $10\text{ eV} \sim 20\text{ eV}$, are used to get higher resolution in the images obtained.
- EDX (Energy-Dispersive X-ray Analysis), which is one of the most useful features of SEM analysis. This analytical tool allows simultaneous non-destructive elemental analysis of the sample. When the incident beam in the SEM bounces through the sample creating secondary electrons, it leaves the sample atoms with holes in the electron shells where the secondary electrons used to be. If these “holes” are in inner shells, the atoms are not in a stable state. To stabilize the atoms, electrons from outer shells will drop into the inner shells. However, the atom must lose some energy in this way because the outer shells are at a higher energy state. It does this in the form of X-rays. The X-rays emitted from the sample atoms are characteristic in energy and wavelength to the element of the parent atom, which shells lost electrons and which shells replaced them.
- TEM (Transmission Electron Microscopy, *JEM-1010*), which can be used to study the morphology of tubes both on their surface topology or cross-section. In the former case, released tubes are placed directly on a holey copper grid coated by carbon films. In the latter case, tubes either released or still residing in template membranes, are embedded in epoxy resin – a mixture of bisphenol A/M epoxy resin, a single component B which is a hardener, a single component C which is an accelerator and a dibutylphthalate D, all of them from *Durcupan ACM Fluka* – and subsequently cured under $60\text{ }^\circ\text{C}$ for 48 h. Slices measuring 70 nm or thinner can be prepared using an ultra-microtome equipped with a diamond knife. The slices were transferred onto carbon coated copper TEM grids for TEM investigations.
- ED (Electron diffraction), which provides important information on the atomic or molecular arrangement of crystalline nanotubes. The spacings between the spots or rings, much can be learned about the molecular structure and compositions of the samples investigated. The spacing between lattice planes on an ED pattern give information on the atomic structure of the samples investigated. The spacing between lattice planes can be

calculated from the diffraction pattern using the equation: $rd = L\lambda$, where d is the spacing between crystallographic planes, λ is the wavelength of electron, L is the camera length and R is the distance from center spot to bright dots on negative. The d calculated can be compared to the values obtained by the diffractogram of X-ray diffraction (XRD). Thus the crystalline direction of each bright spot can be determined.

4.2.2 X-ray diffraction (XRD)

XRD was performed by using a Philips X'pert MRD diffractometer with cradle and secondary monochromator for Cu $K\alpha$ radiation with a wavelength of $\lambda = 0.15405 \text{ nm}$. $\Theta/2\Theta$ scans are carried out in the reflection mode with a small 2Θ increment (0.05°) and a long integration time ($1s \sim 20s$). When the tubes are still residing in the pores of the template membrane, the sample is placed in the diffractometer in such a way that the template surface with the pore openings is arranged perpendicular with respect to the plane defined by the incident and the scattered X-ray beams (in figure 4.1, $\Psi = 0^\circ$). The tubes are well aligned within the templates during the measurements. If it is necessary to investigate the textures of the samples, an additional scan, so-called Ψ scan, can be carried out. The settings of Ψ (incident beam) and 2Ψ (detector) were fixed to specific values. The sample was tilted by an angle Ψ around the axis defined by the intersection of the plane of the incident and the scattered X-ray beams with the template surface. The setup is displayed schematically in figure 4.1. Ψ equals zero if the two planes are oriented perpendicularly. The scattering intensity is measured as a function of the tilting angle Ψ . This method allows to record a fiber diffractogram in reflection mode.

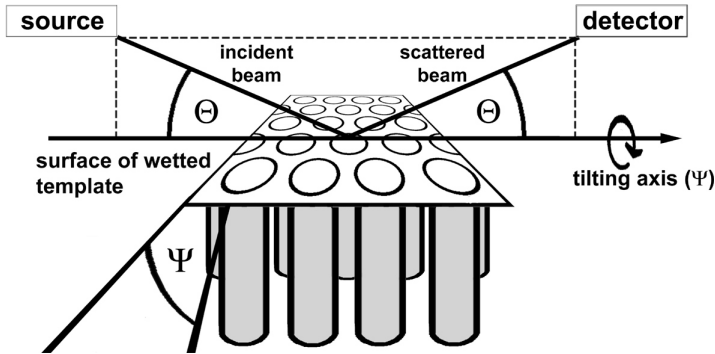


Figure 4.1: Schematic depiction of the setup used for the X-ray diffraction experiments. For the $\Theta/2\Theta$ scans, the samples were placed in the device in such a way that the surface of the wetted template was oriented perpendicular to the plane of incident and scattered X-ray beams. To perform the Ψ scans, the setup was adjusted to selected 2Θ angles. Then, the samples were tilted by an angle Ψ around an axis defined by the intersection of the template surface and the plane of the incident and the scattered X-ray beam. The scattering intensity was measured as a function of the tilting angle Ψ .

4.2.3 Scanning force microscopy (SFM)

The main technique used for the investigation of ferroelectric materials is the scanning force microscope (SFM). Several modes of operations can be used, including topography mode, friction mode, non-contact mode, lift mode and piezoresponse mode. By using SFM, such information as topology, spontaneous polarization, piezoelectric domain wall as well as phase on a ferroelectric material sample can be obtained.

Topology investigation by AFM

The AFM used consists of a cantilever with a sharp tip at its end. The tip is brought into mechanical contact to a sample surface. The force between the tip and the sample leads to a deflection of the cantilever according to Hooke's law. Typically, the deflection is measured using a laser spot reflected from the top of the cantilever. A feedback mechanism is employed to adjust the tip-to-sample distance to keep the force between the tip and the sample constant. This can be achieved by mounting the sample on a three-dimensional piezoelectric actuator.

The tip is then scanned across the sample surface and the vertical displacement necessary to maintain a constant force on the tip is recorded. The resulting map of $s(x, y)$ represents the topography of the sample (c.f. figure 4.2).

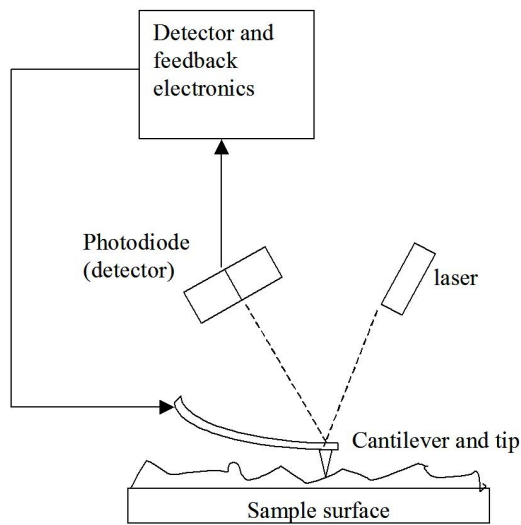


Figure 4.2: Schematic of the set-up of AFM.

Poling of ferroelectric domains

An unpoled ceramic initially displays no net piezoelectric response (as shown in figure 4.3a) because the piezoelectric tensors of the randomly oriented grains produced by the fabrication process average to close to zero over the volume of an engineering component such as a piezoelectric actuator. Poling endows the ceramic with its global piezoelectric properties. In this process a direct current (dc) electric field with a strength larger than the coercive field strength is applied to the ferroelectric ceramic at a high temperature, but below the Curie point. On application of the external dc field the spontaneous polarization within each grain gets orientated towards the direction of the applied field, as shown in figure 4.3b. During the poling process, ferroelectric switching occurs in many grains. The grains' crystallographic axes retain the orientation fixed by the sintering process. However, the high value of electric field applied during poling causes ferroelectric switching such that the average polarization becomes biased along the direction of the electric field vector E_i . After poling, there is an overall bias in the average of the grains' polarization vectors, which gives rise to an overall remanent polarization and a non-zero overall piezoelectric tensor. Note that poling is usually carried out at a temperature which is too low for significant creep or recrystallization to occur.

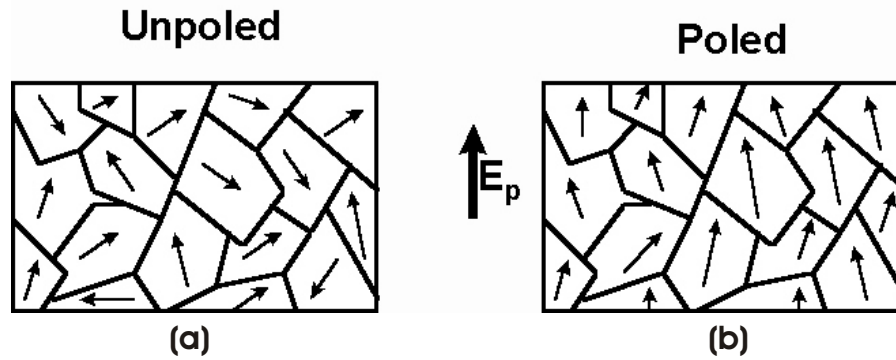


Figure 4.3: Schematic of the poling process in piezoelectric ceramics: (a) In the absence of electric field the domains have random orientation of polarization; (b) the polarization within the domains aligns in the direction of the applied field.

Piezoresponse Force Microscopy (PFM)

Among all the operation modes listed above, the one which interests us most is the last one: scanning force microscopy operated in the piezoresponse mode, first introduced by Gütthner and Dransfeld [115]. Integrated with a lock-in technique (as depicted in figure 4.5), SFM is a powerful tool to probe the local polarization status and electromechanical properties of ferroelectric structures in the above-mentioned piezoresponse mode.

In PFM, an ac voltage is applied between the conductive tip and the electrode on the back side of the ferroelectric. The electric field underneath the tip and the inverse piezoelectric effect causes a periodic thickness change with the same frequency as the applied voltage. This local vibration is transferred by the nanomechanical contact between tip and ferroelectric into a periodic cantilever bending and is detected by the laser deflection signal of the SFM. The further analysis of this signal is performed with a dual channel Lock-In amplifier which measures the values of amplitude(A)/phase(Φ) or real-part($A \sin \Phi$)/imaginary part($A \cos \Phi$) relative to the applied ac voltage. In piezoresponse mode the frequency of the imaging should be far lower than the cantilever resonant frequency to avoid mechanical resonance of the cantilever. The driving ac voltage should also be significant below the coercive voltage of the ferroelectric to avoid distortions of the original domain structure

Two intercalating types of information can be drawn from the SFM investigations on polarized domains:

- Information on domain orientation:

As pointed out earlier, the sign and magnitude of the piezoelectric constants depend on the value and vectorial orientation of the spontaneous polarization. Therefore, the phase lag between the excitation voltage and the piezoresponse of opposite domains amounts to 0° or 180° , respectively. This can be illustrated by figure 4.5, with two ferroelectric domains having opposite orientations of polarization, perpendicular to the sample surface and sandwiched between a bottom electrode and the conductive SPM tip. In figure 4.5a, no voltage is applied between the electrodes and the two ferroelectric domains have the same dimensions in z-direction, only governed by the spontaneous strain which is the same for the two domains. When a voltage is applied to the tip, the electric field generated in the sample causes the domains with the polarization parallel to the field to extend and the domains with opposite polarization to contract. The images (b) and (c) in figure 4.5 illustrate the z-deformation of the domains when a respectively positive and negative

voltage with respect to the bottom electrode is applied to the tip.

Figure 4.4 illustrates the principle of obtaining the information on the polarization state from the piezoresponse signal. It is based on the detection of the local electromechanical vibration of the ferroelectric sample caused by an external ac voltage. The voltage is applied through the probing tip, which is used as a movable top electrode. The modulated deflection signal from the cantilever, which oscillates together with the sample, is detected using the lock-in technique, as in the case of the noncontact imaging. However, in the piezoresponse mode the frequency of the imaging voltage should be far lower than the cantilever resonant frequency to avoid mechanical resonance of the cantilever. An external voltage with a frequency ω causes a sample vibration with the same frequency due to the converse piezoelectric effect. Vibration of the sample under the ac voltage also has a second harmonic component at 2ω due to the electrostrictive effect and dielectric constant. The domain structure can be visualized by monitoring the first harmonic signal (piezoresponse signal). The phase of the piezoresponse signal depends on the sign of the piezoelectric coefficient (and therefore, on the polarization direction) and reverses when the coefficient is opposite. This means that regions with opposite orientation of polarization, vibrating in counter phase with respect to each other under the applied ac field, should appear as regions of different contrast in the piezoresponse image.

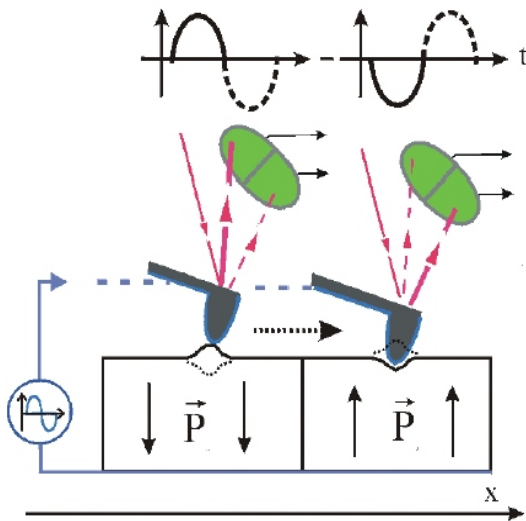


Figure 4.4: Demodulation of the information on the polarization state from the piezoresponse signal.

By this method, not only the cantilever movements normal to the sample surface but also lateral shear oscillations (piezoelectric d_{15} constant) can be measured, so that the direction of the spontaneous polarization is detected even when it is parallel to the surface.

It should be mentioned that the vibration of the sample under the ac voltage also has a second harmonic component due to the electrostrictive effect and dielectric constant. Therefore it would be possible to measure electrostrictive properties with the same experimental setup. However, the work in this thesis focuses on the characterization of ferroelectric and piezoelectric properties.

- Information on domain wall:

As the tip, held at some distance from the surface, scans over the ferroelectric sample, surface polarization charges induce an image charge Q_p in the probing tip, which results in an additional contribution to the attractive force due to Coulomb interaction. The resulting force gradient is proportional to the product of the electric field due to the polarization and the charge Q_p induced in the tip and, therefore, depends only on the polarization

magnitude and not the sign. This implies that the contrast of opposite 180° domains will be the same and that domain walls will only be visible due to the spatial variation of the charge density in the vicinity of a 180° domain boundary. The tip experiences a change in the force gradient when it is above the wall and the feedback loop alters the tip-sample distance to keep the gradient constant, thus producing a variation of contrast in the feedback signal image, which can be interpreted as an image of the domain wall. Image contrast depends essentially on the external bias voltage applied to the probing tip and on the tip material. By varying the bias voltage, the contrast of domain boundaries can be eliminated and contrast between opposite domains can be observed.

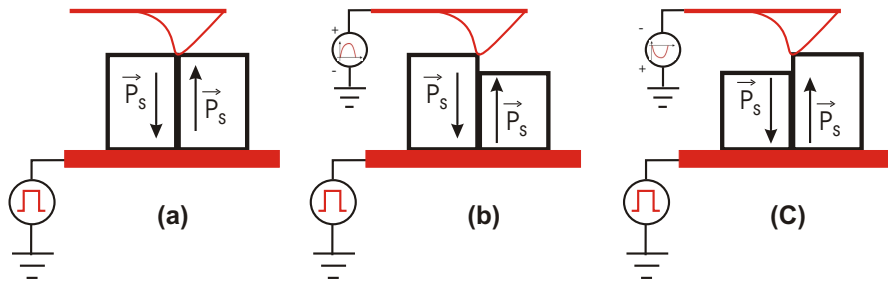


Figure 4.5: Principles of piezoresponse SFM. (a) No topographic contrast if no voltage is applied. (b) A change in thickness occurs for neighboring domains with opposite polarization in opposite directions during the positive half period and (c) during the negative half period.

4.2.4 Differential scanning calorimetry (DSC)

DSC is a thermoanalytical technique, by which the difference in heat flow (power) to a sample and reference is monitored against temperature while the temperature of the sample, in a specified atmosphere, is programmed. DSC is the most widely used thermoanalytical technique, which enables to determine a number of parameters connected with the physical or chemical processes in condensed phase. Temperatures of phase transitions of first and second order, enthalpies of phase transitions, polymorphism, liquid crystalline transitions, phase diagrams, thermoplastic polymer phase changes, glass temperatures, purity measurements and kinetic studies can be mentioned as examples where DSC is highly efficient.

In order to see the phase transition as well as the melting of ferroelectric materials such as P(VDF-co-TrFE) copolymer, power compensation DSC investigations were carried out. In such a calorimeter, the heat to be measured is compensated with electric energy by increasing or decreasing an adjustable *Joule's* heat. The measuring system consists of two microfurnaces of the same type made of platinum-iridium alloy, each of which contains a temperature (platinum resistance thermometer) and a heat resistor (made of platinum wire). For a *Perkin-Elmer DSC 7* used in the experiment, the microfurnace is about 9 mm in diameter, 6 mm in height and has a mass of approximately 2 g . The time constant is slightly smaller than 2 s , and the isothermal noise is about $2\mu\text{ W}$. The maximum heating power of a microfurnace is about 14 W and the maximum heating rate is $500\text{ K}/\text{min}$. For the evaluation of the curvatures obtained, the program *Pyris Manager* is used.

4.3 Summary of the chapter

In this chapter, the methods to get either released or arrays of 1D nano- and micro-objects, depending on the different porous templates used, were presented first. Then, several characterization techniques, including electron microscopy, energy-dispersive X-ray analysis, X-ray diffraction, scanning force microscopy and differential scanning calorimetry were depicted. These methods and techniques will be used in the next chapters during the fabrication and characterization procedures of 1D nano- and micro-objects.

5. Building Blocks I: Ferroelectric inorganic micro- and nano(shell) tubes

5.1 New candidates for nanoelectronics: ferroelectric nanotubes

In this chapter, one of the core elements for a complex building block proposed in this thesis towards a mass storage device, inorganic piezoelectric micro- and nano(shell) tubes, are presented. The fabrication of such ferroelectric nanoshell tubes is realized by wetting of porous templates. The ferroelectric switching behavior of an individual inorganic piezoelectric tube as-obtained will also be demonstrated by atomic force microscopy.

The most commonly used ferroelectric materials are members of the perovskite family of ferroelectric ceramics, which include barium titanate ($BaTiO_3$), lead titanate ($PbTiO_3$) and many alloys in the “PZT” system such as $PbZr_xTi_{1-x}O_3$. These ceramics are called “perovskite-type” because their crystal structures are similar to that of the mineral perovskite ($CaTiO_3$). They were discovered and came rapidly to prominence in engineering applications between the years of about 1940 and 1960, because they are chemically stable, relatively easy to produce, and display high values of piezoelectric coupling coefficients. Nowadays, they are among the best candidates for the development of FeRAMs.

The unit cell of the crystal structure of PZT is shown in figure 5.1. Note that the titanium ion Ti^{4+} is displaced from the geometric center of the unit cell, and that the six oxygen ions O^{2-} , which lie at the corners of an octahedron, are also displaced. The oxygen octahedra in perovskites are typically quite rigid, and displace as a unit. The source of the dipole moment is due to the fact that positively charged Ti^{4+} and negatively charged O^{2-} ions are displaced from the positions they would adopt in a regular cubic perovskite structure. Furthermore, the unit cell is stretched in the same direction as that in which the ions are displaced; the unit cell has a tetragonal shape. The displacement of ions and the tetragonality of the unit cell are exaggerated in figure 5.1. It is possible to make a crude estimate of the remanent polarization using the positions and charges of the ions in the unit cell, as established by X-ray diffraction and neutron diffraction studies. The displacement of the ions from central positions are [116]:

$$Ti^{4+} : +0.040 \times 4.150 \times 10^{-10} [m] \quad O^{2-} : +0.112 \times 4.150 \times 10^{-10} [m]$$

and the unit cell volume is: $4.150 \times 3.904 \times 3.904 \times 10^{-30} [m^3]$.

When an external electric field is applied to a crystal of PZT, small distortions of the unit cell occur. These distortions are approximately linear; reversing the sense of the applied field reverses the sense of the distortion, and doubling the magnitude of the field doubles the magnitude of the distortion. However, if a sufficiently large value of electric field (known as the *coercive field*) is applied, the direction of polarization in the unit cell may be “switched”, as shown in figure 5.1 from (a) to (b). In the distorted perovskite unit cell there are six positions which the

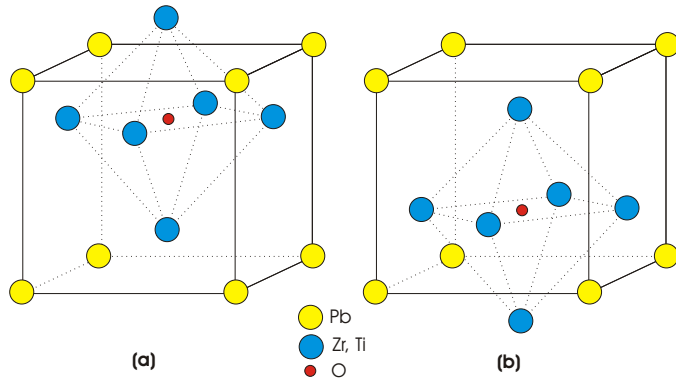


Figure 5.1: Unit cell of the crystal structure of $PbZr_xTi_{1-x}O_3$. Polarization can be switched from (a) (up) to (b) (down).

central cation could adopt, and from each of those positions, it could be switched into any of the other five positions giving a total of 30 different ferroelectric switching possibilities.

Many ferroelectric materials adopt the simple-cubic perovskite structure at high temperature and undergo structural phase transitions to distorted ferroelectric structures at lower temperatures. For example, upon cooling, $BaTiO_3$ undergoes a sequence of ferroelectric transitions: first from the cubic (C, space group $Pm3m$) to a tetragonal (T, space group $P4mm$), then to an orthorhombic (O, space group $Amm2$), and finally to a rhombohedral (R, space group $R3m$) phase. Passing through this sequence, the polarization P first vanishes in the C phase, and then becomes oriented in the [001], [011], and [111] directions in the T, O, and R phases, respectively. PZT undergoes a transition from the simple cubic C phase to a ferroelectric phase at a Curie temperature T_c that ranges from about 490 °C at $x = 1$ to 230 °C at $x = 0$. The transition occurs to the T phase for x greater than about 0.48, and to the R phase for smaller values of x [117].

5.2 Large-scale fabrication of inorganic ferroelectric nano(shell) tubes by template wetting

The fabrication approach of lead zirconate titanate, ($PbZr_{0.52}Ti_{0.48}O_3$ PZT) and barium titanate ($BaTiO_3$) nanotubes consists of wetting the pore walls of porous templates, such as macroporous silicon [118], or porous alumina [96], by oligomeric precursors and subsequent high temperature annealing.

Oligomers containing metals in the stoichiometric quantities (*PZT 9906 Polymer* and *BATIO 9101 Polymer* from *Chemat Technology, INC*) were used as precursors. After the precursors were brought into contact with the template, they wetted the pore walls under ambient conditions at room temperature and led to a reduction of the total energy of the system [119]. The wetting was so uniform that a complete coverage of the whole surface of the pore walls occurred. Then, the oligomeric precursors in the pores were transformed into an amorphous oxide layer by annealing in air at 300 °C. This amorphous layer was subsequently crystallized by a thermal treatment in air for one hour at 650 °C for PZT and 850 °C for $BaTiO_3$ to obtain the perovskite phase. The presence of this phase was confirmed by X-ray diffraction for both $BaTiO_3$ and PZT nanotubes (as will be shown in section 5.3). Either released or free-standing ferroelectric tubes can be obtained by a controlled etching of the template. A single step of infiltration yields a wall thickness of around 100 nm for both PZT and $BaTiO_3$ nanotubes in case that the template used has a pore diameter larger than about 200 nm.

5.3 Morphology and crystallinity of ferroelectric nano(shell) tubes

PZT nano(shell) tubes

Figure 5.2a shows the resulting ferroelectric PZT tubes released from a macroporous silicon template. In the image, the tubes appear straight and have a very high aspect ratio of about 100. The hollow nature is obvious from figure 5.2b, in which the open end of a PZT nano(shell) tube is depicted. Depending on the parameters of the templates used, the outer diameter ranges from 50 nm (at this point, ferroelectric nanoshell tubes become nanowires, as depicted in figure 5.2c) up to several micrometers and their length from a few micrometers up to more than $100\ \mu\text{m}$. When the pore diameters of the template used decrease to a critical point, which is estimated to be around 100 nm , the nanoshell tubes become nanowires. If the pore diameter decreases even more to the same order of magnitude as the crystallites of the ferroelectric materials, the obtained nanowires do not have smooth walls anymore. This can be seen in figure 5.2c in which the picture of a bundle of PZT nanowires with a diameter of 60 nm is taken by TEM (100 keV). It shows that the wires are still straight and have a high aspect ratio but are no longer smooth. This is because the crystallites, which are estimated to have a size of around 20 nm , do not take exactly the same curvature as the inner pore walls of the template. Highly ordered arrays of PZT nanoshell tubes can also be obtained by partial etching of the template. Figure 5.2d depicts such an array by a SEM image.

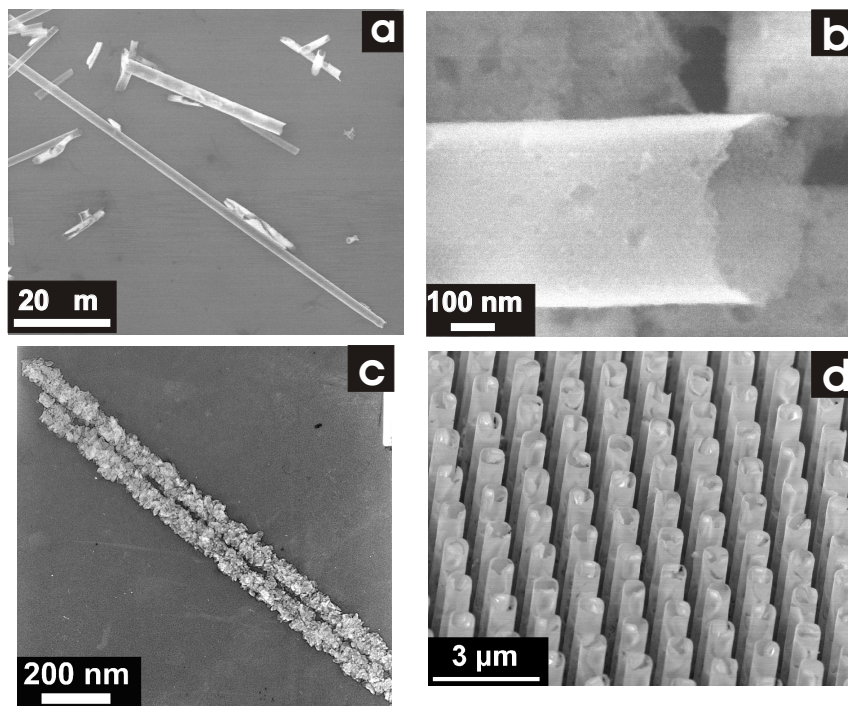


Figure 5.2: (a) SEM image of released ferroelectric nanoshell tubes consisting of PZT with a diameter of $1\ \mu\text{m}$. (b) Open end of a ferroelectric nanoshell tube with a diameter of 400 nm and composed of PZT. (c) TEM image of a bundle of ferroelectric nanowires consisting of PZT with a diameter of 60 nm . (d) An array of free-standing PZT nanoshell tubes of $1\ \mu\text{m}$ in diameter with the capped end fixed to a silicon substrate.

In order to get more information on the composing elements as well as on the crystallographic

structures of the PZT nanoshell tubes, EDX, XRD and high resolution TEM (HRTEM) investigations were employed. The existence of Pb, Ti, Zr and O elements in released PZT nanoshell tubes lying on a silicon wafer were confirmed by the EDX spectrum shown in figure 5.3. A point to note is that there always exists a deficiency in the Pb content as Pb is a very volatile element and could diffuse during the high temperature annealing of the sample. To investigate the formation of PZT crystallites, a wetted macroporous silicon template with a pore diameter of $2\ \mu\text{m}$ was investigated by XRD in the reflection mode. For all the XRD pattern shown in figure 5.3b, the reflections of PZT were assigned by using the JCPDS card *No.* 33 – 0784. The (100), (101), (110) and (201) reflections of tetragonal PZT occurred at $2\Theta = 22^\circ, 30.9^\circ, 31.4^\circ$ and 50.4° , respectively. The peak marked by a * comes from a different lead oxide formed during the annealing process. A HRTEM characterization can visualize crystallites. Figure 5.3c depicts a HRTEM image of a crystallite within the tube wall of PZT having a crystallographic direction of $\langle 110 \rangle$.

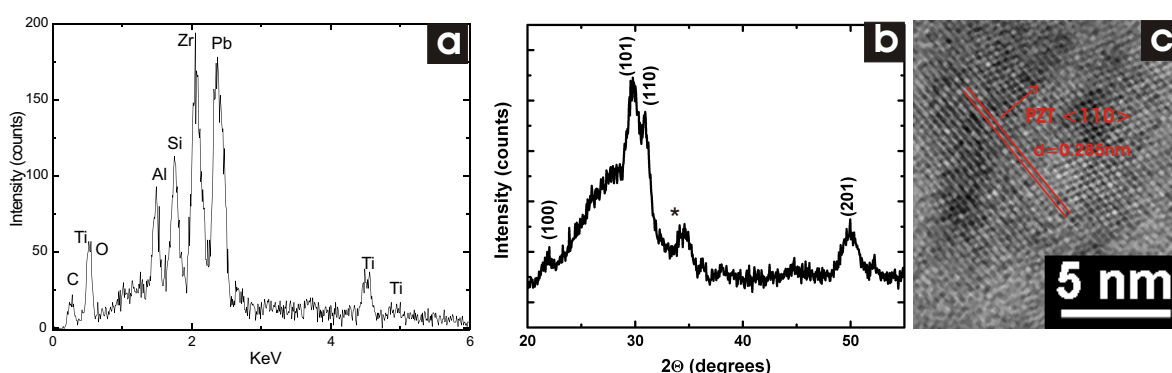


Figure 5.3: (a) Selected area EDX spectrum obtained on the PZT nano(shell) tubes shown in the figure 5.2 representing specific composing elements. (b) An XRD pattern of macroporous silicon with a pore diameter of $2\ \mu\text{m}$ containing PZT nanoshell tubes that was annealed shortly at 300°C in air and 650°C for $1\ \text{h}$ under lead oxide atmosphere, measured at room temperature. One scale division on the intensity axis corresponds to 200 counts. (c) High resolution TEM micrograph on the tube wall of a PZT nanoshell tube. The crystallographic $\langle 110 \rangle$ direction of the PZT grains is indicated.

BTO nano(shell) tubes

Figure 5.4a represents a bundle of ferroelectric nanoshell tubes consisting of BaTiO_3 with a diameter of $1\ \mu\text{m}$. The length of the nanotubes can be seen from the same picture, which is around $100\ \mu\text{m}$. The caps of BaTiO_3 nanotubes are exact replicas of the pore bottoms. XRD investigations were performed on BTO nanoshell tubes located within the template pores in the reflection mode (figure 5.4b). The reflections of BTO were assigned using the JCPDS cards *No.* 89 – 2475. The (100), (110), (111), (200), (210), (211), (120), (300), (310) and (311) reflections of the rhombohedral *BTO* occurred at $2\Theta = 22.2^\circ, 31.6^\circ, 38.9^\circ, 44.9^\circ, 50.9^\circ, 55.8^\circ, 65.8^\circ, 70.5^\circ, 74.7^\circ$ and 79.2° , respectively. Again, the peaks marked by a * come from a mixture of different oxides formed during the sample preparation processes.

A more detailed characterization of the ferroelectric nanotubes can be carried out also by TEM. Figures 5.5a and 5.5b show the cross-section image of BTO tubes still embedded in the silicon template. The tube walls consist of a crystalline layer sandwiched between two amorphous layers at the silicon-ferroelectric interface and at the internal ferroelectric surface. While the amorphous layer at the silicon-ferroelectric interface is the result of a reaction between the oxide and silicon due to the high crystallization temperature, the inner amorphous layer might be an

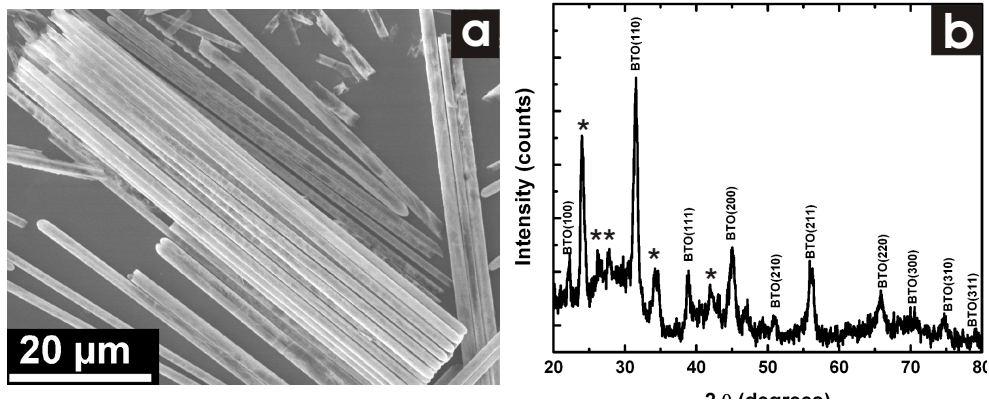


Figure 5.4: (a) SEM image of a bundle of ferroelectric nanoshell tubes consisting of $BaTiO_3$ with a diameter of $1 \mu m$. (b) An XRD pattern of macroporous silicon with a pore diameter of $2 \mu m$ containing BTO nanoshell tubes that was annealed shortly at $300^\circ C$ in and $850^\circ C$ for $1 h$ in air, measured at room temperature. One scale division on the intensity axis corresponds to 200 counts.

artifact during the TEM sample preparation, i.e., redeposition of amorphous materials during ion-milling thinning. A selected area electron diffraction pattern (SAED) is shown in figure 5.5c, confirming the rhombohedral structure of the BTO nano-crystallites.

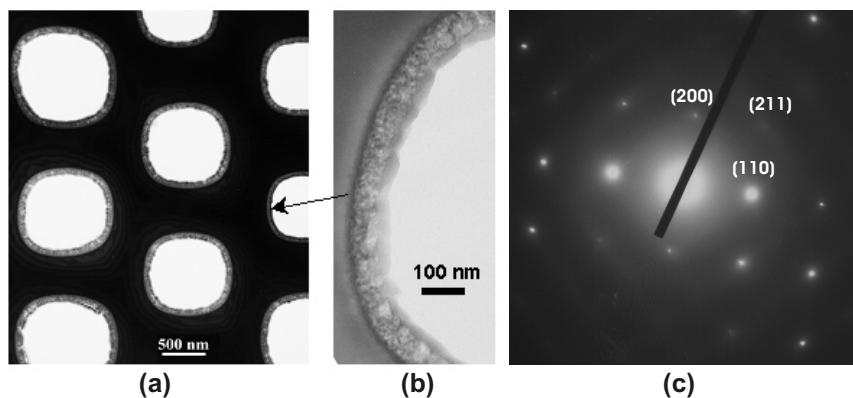


Figure 5.5: Planar TEM image on the cross-section of BTO nanotubes in silicon template. (a) Overview; (b) Zoomed-view on the tube walls; (c) SAED on BTO tube walls.

5.4 Occurrence of Rayleigh instabilities

As described in section 2.4.3 and section 2.6.2, if a porous template is wetted by a low molar mass compound, long-range intermolecular interactions can play a role and result in a wetting film consisting of several molecular layers. This is due to the interaction between the pore walls and the wetting molecules that are not in direct contact. This phenomenon could lead to the formation of undulations, which are referred to as Rayleigh instabilities (c.f. section 2.4.3). Figure 5.6 depicts such a situation in which a Rayleigh instability occurred in PZT nanoshell tubes where an oligomer was used as the precursor during the sample preparation. A zoomed view of figure 5.2d on the open-end of an array of free-standing PZT nanoshell tubes is shown in figure 5.6a in which the tube walls have an inhomogeneous thickness. The inhomogeneity can be seen more clearly in figure 5.6b in which a TEM micrograph on the cross-section of a

tube wall along the tube axis of a PZT nanoshell tube is shown. Both sides of the tube wall were coated by a layer of Pt to delineate the corresponding boundary.

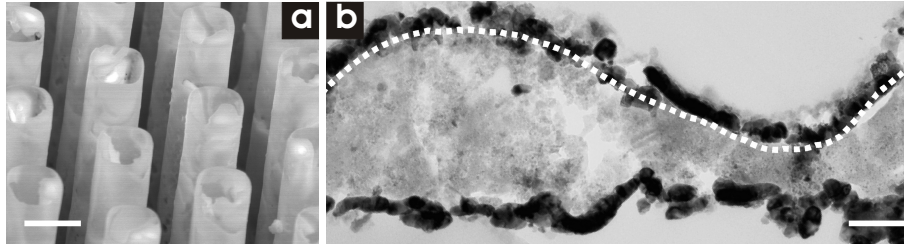


Figure 5.6: Occurrence of Rayleigh instability in PZT nanoshell tubes. (a) A zoomed view of figure 5.2d on the open-ends of an array of free-standing PZT nanoshell tubes where the tubes walls have an inhomogeneous thickness. (b) TEM micrograph of the cross-section of a tube wall along the tube axis of a PZT nanoshell tube with both sides coated by a layer of Pt to delineate the boundary of the tube wall. The scale bars in both images represent 100 nm .

5.5 Ferroelectric hysteresis of individual ferroelectric nano(shell) tubes

Although the tube walls of the ferroelectric PZT nanoshell tubes show an undulation in thickness as a result of the occurrence of a Rayleigh instability and have a poor crystallinity, the piezoelectric and ferroelectric properties can still be measured on a local scale. In order to measure the piezoelectric and ferroelectric properties, free PZT nanotubes were prepared, deposited onto platinum-coated silicon wafer, and subsequently annealed one hour in oxygen at $700\text{ }^{\circ}\text{C}$. The ferroelectric properties were measured using scanning force microscopy in the aforementioned piezoresponse mode [120]. Individual tubes, with their long axis parallel to the substrate surface, were probed by a conductive tip and characterized by measuring the local piezoelectric hysteresis. Figure 5.7 shows the piezoelectric hysteresis loop obtained on an individual PZT tube with an outer diameter of 700 nm and a wall thickness of 90 nm . The piezoelectric signal is an unambiguous proof of the piezoelectricity of the tubes and the hysteresis in the piezoresponse signal is directly associated with the polarization switching and ferroelectric properties of the sample. Moreover, the rectangular shape of the hysteresis loop showing a sharp ferroelectric switching at a coercive voltage of about 2 V is connected with a high quality of ferroelectric material. The effective remnant piezoelectric coefficient is about 90 pm/V and is comparable with usual values obtained on PZT thin films.

Here we point out that it is difficult to compare the above values to the piezoelectric coefficients of bulk material since the measurement was performed on a tube geometry which has a relatively complicated field distribution and vibrational modes. However, the suggested inference is that the polar axis lies primarily along the nanotube and not perpendicular to its walls, since the effective d_{33} -value is ca. 10% of the expected value for an oriented film.

If concentric electrodes can be applied to the tubes (that is, with a cathode inside the cylindrical tubes and an anode outside), the application potential as well as the understanding of the field geometry of the ferroelectric nanoshell tubes would be greatly enhanced. The ferroelectric hysteresis loop shown in figure 5.7 was obtained by laying individual tubes down on a metal ground plate, sputtering semicircular top electrodes from above, and measuring the switching across a small arc of the tube circumference. In Chapter 7, first steps towards a concentric electroding,

which consists of platinum inner and outer layers sandwiching a ferroelectric nanoshell tube will be described. Especially, the use of ordered arrays of pores from macroporous silicon templates has significant benefits over other porous substrates in that the coatings/tubes produced are also in a registered array ordered over several mm's or even cm's. This facilitates addressing of such an array for device applications.

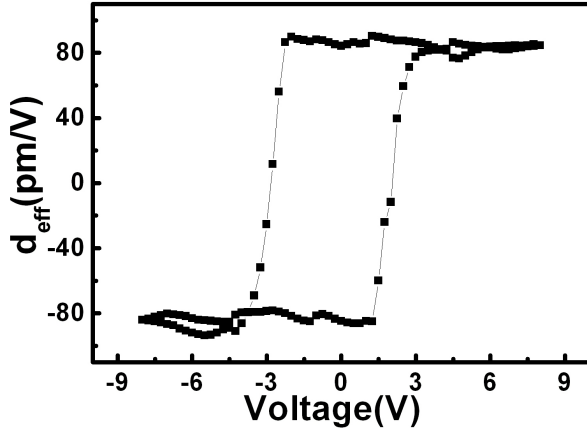


Figure 5.7: Piezoelectric hysteresis loop of an individual PZT tube measured by piezoresponse AFM.

As already mentioned earlier, the linear part of the hysteresis loop is due to a real increase of the piezoelectric constant and can be explored to estimate the local electrostriction coefficient Q by the following relationship: $\frac{\partial d_{33}}{\partial E} = 2Q\epsilon_{33}$. The slope of the linear part of hysteresis loop is $102.6 \pm 10.8 \text{ pm}/V^2$, which leads to a value of $Q = 684 \pm 7m^4/C^2$.

5.6 Summary of the chapter

In this chapter, a simple and inexpensive generic method was demonstrated to obtain ferroelectric nano(shell) tubes with sizes tunable over a relatively large mesoscopic range. Two different inorganic perovskite materials were explored in tubular structures, respectively PZT and BTO. Their morphologies were investigated by electron microscopies, crystallinity by XRD and piezo-/ferroelectric properties by PFM investigations. If the occurrence of Rayleigh instabilities can be suppressed, these ferroelectric nano(shell) tubes with diameters of several hundred nanometers and with wall thicknesses of a few tens of nanometers could be ideal candidates as core building blocks of a functional device for electromechanical systems such as mesoscopic actuators similar to current piezoelectric scanners as well as for mass storage device provided electrodes can be applied properly.

6. Building blocks II: Ferroelectric P(VDF-co-TrFE) copolymer nanotubes

In this chapter, ferroelectric nanotubes and nanorods consisting of P(VDF-co-TrFE) copolymers will be presented, which are also promising to be potentially used as core elements in more complex functional devices in such fields as mass storage. With respect to the inorganic ferroelectric tubes presented in Chapter 5, the 1D copolymer nano- and micro-structures are chemically more stable. Moreover, pyrolysis is not necessary during the fabrication, which avoids the formation of by-products. Because of the high molecular mass of the copolymers, Rayleigh instabilities can also be suppressed, thus leading to a homogeneous thickness of tube walls. In the following sections, these nano-structures will be studied in terms of their crystallinity, piezo- and ferroelectricity as well as their potential applications in light of their molecular structures.

6.1 Properties of PVDF and its copolymers

Ferroelectric PVDF

The occurrence of a pronounced piezoelectric effect in synthetic polymers can mainly be attributed to the presence of a non-centro-symmetric unit cell and a net polarization in the material. To achieve this in polymeric materials, one requires [121]: a large dipole moment in the repeating unit, feasibility of crystallization in a non-centrosymmetric unit cell, and alignment of molecular dipoles.

A dipole moment arises from a charge separation between adjacent atoms. In polymers this can occur between covalently bonded atoms along the polymer chain or between adjacent chains. For example, a significant dipole moment occurs when chlorine or fluorine atoms are incorporated in the carbon backbone. The fluorine atom, which has a van der Waals radius (1.35 \AA) only slightly larger than that of hydrogen (1.2 \AA), forms highly polar bonds with carbon having a dipole moment of 1.9 Debye ($1 \text{ Debye} = 3.34 \cdot 10^{-30} \text{ C.m}$).

A strong piezoelectricity was observed by Yagi in 1969 [27] after poling an uniaxially drawn PVDF film in a suitable electric field. In fact, each molecular unit of PVDF in the carbon backbone contains two hydrogen and two fluorine atoms and thus has net dipole moments, pointing from the relatively electronegative fluorine to the hydrogen. Furthermore, PVDF molecules have a choice of multiple conformations. Usually, the molecular chains of most polymers within a crystal lattice are restricted by steric and electrostatic intramolecular interactions into a regular conformation of lowest potential energy. However, since rotational energy barriers of PVDF are high, chains can also be stabilized into favorable conformations other than that of lowest energy. The most well-known conformations of PVDF include [122]:

- β -phase: All-trans (TTTT) conformation of the polar β phase crystallizes in a pseudo-hexagonal polar packing as shown in figure 6.1a. The highest piezoelectric response of

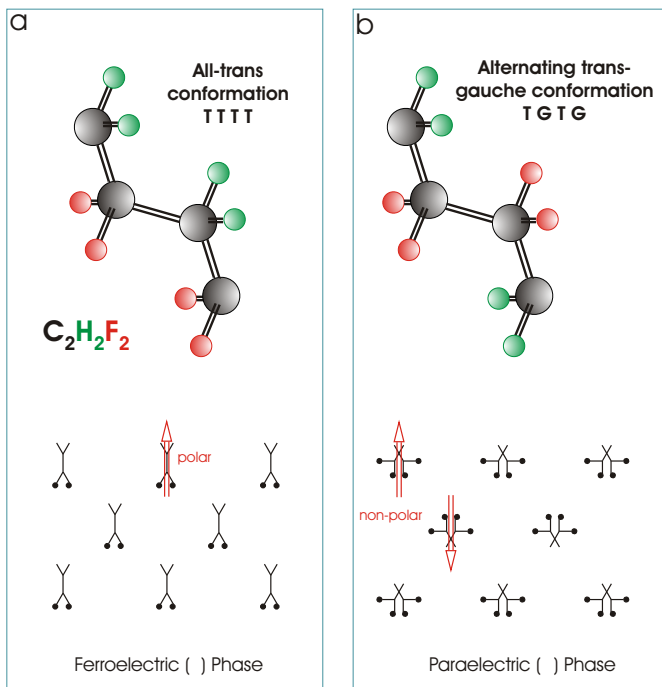


Figure 6.1: (a) All-trans TTTT conformation of the ferroelectric β phase (upper part) and the corresponding crystal structure (lower part); (b) Alternating trans-gauche TGTG conformation of the paraelectric α phase (upper part) and the corresponding crystal structure (lower part). The arrows indicate the dipole directions resulting from the difference in electronegativity between fluorine and hydrogen atoms.

this polymer is associated with this phase due to the alignment of all its dipoles in the same direction normal to the chain axis, the all-trans is the most highly polar conformation (2.1 Debye per unit) among all.

- α -phase: In this phase, PVDF crystallizes with two chains per unit cell with dipole component normal to the chain axes (so-called alternating trans-gauche TGTG conformation) which are, however, anti-parallel, as shown in figure 6.1b. In this type of packing, the dipoles of neighboring chains neutralize each other [123]. The α -phase is the most common polymorph of PVDF and can be easily obtained by melt crystallization.

By poling with a high voltage, the α -phase can be transformed into a new crystal form δ in which all dipole moments become parallel. In fact, this transformation involves a rotation of every second chain by 180° about its axis so that the molecules are now packed with the transverse components of their dipoles moments pointing in the same direction.

Ferroelectric copolymer P(VDF-co-TrFE)

In the last decade, copolymers of PVDF with trifluoroethylene (TrFE) containing different mole fractions of both components have been studied extensively as new polymeric materials with strong piezo- and pyroelectric response, because they exhibit certain advantages over pure PVDF. P(VDF-co-TrFE) is a random copolymer which is synthesized by copolymerization VDF and TrFE monomers.

In the composition of the P(VDF-co-TrFE) copolymer, the additional fluorine atoms in the chain reduce the influence of head-to-head and tail-to-tail defects [124]. Therefore, the crystallinity of the copolymers could be increased to 80% [123] after annealing for a certain duration [125, 126, 127, 128]. Since these copolymers contain a greater proportion of the comparatively bulky fluorine atoms than that of PVDF, rotation is sterically quite hindered, so that they are forced to adopt the conformation of least discomfort (such a conformation is invariably helical or quasi-helical). As a result, their molecular chains cannot accommodate the TGTG conformation of the α -phase and instead crystallize at room temperature in the ferroelectric phase [123]

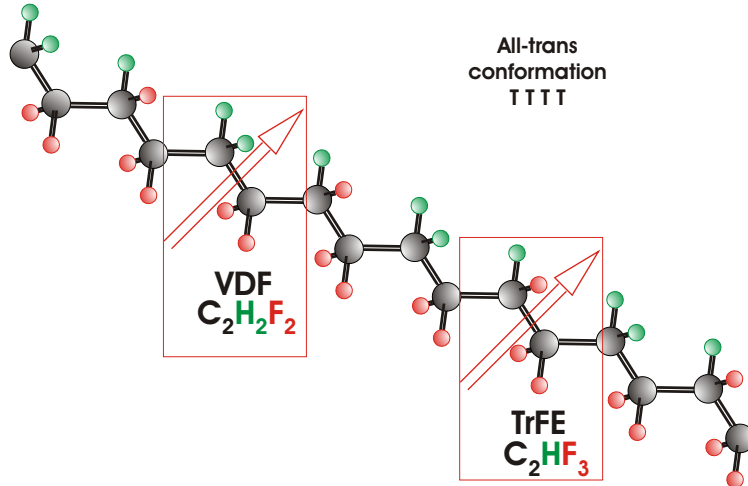


Figure 6.2: Schematic drawing of the molecule chain of P(VDF-co-TrFE) copolymer in all-trans conformation with a ratio of VDF and TrFE of 75 : 25. The arrows stand for the same meaning as in figure 6.1.

of the extended all-trans planar conformation with small statistical deviations away from the plane. This structure is widely assumed as orthorhombic with dimensions rendering it “pseudo-hexagonal”. The molecular chains with all-trans conformation are packed in a parallel array, forming a highly polar phase.

As shown in figure 6.2, in fact, the unit cell of the P(VDF-co-TrFE) copolymer, i.e., the intermolecular lattice structure, chain packing and dipolar alignment are almost the same as in the case of β -PVDF. The β -content can be enhanced under simultaneous stretching and corona poling [129]. The main structure difference between the homopolymer and its copolymers involves the intermolecular spacing and thus the lattice plane distances. This is mainly because of the larger fluorine atoms, the a and b axis of the unit cell of the copolymer are larger than that of β -PVDF [130]. This might also be one reason for the faster dipole alignment of the copolymer compared to β -PVDF [125, 131, 132, 133]. Despite the smaller dipole moment of the TrFE monomer unit, the polarization of the copolymers can be even higher than that in pure PVDF due to the higher crystallinity of the copolymers [125, 134].

The copolymers P(VDF-co-TrFE) exhibit a reversible Curie transition at which the ferroelectric polymers show a solid state transformation to a non-polar paraelectric state [29, 34] at a transition temperature below melting point ($T_c < T_m$). If P(VDF-co-TrFE) copolymers are heated, a first-order transition from a ferroelectric to a paraelectric phase appears [134, 135, 136]. The crystalline structure in the ferroelectric phase is composed of all-trans chains with their dipoles parallel to the b -axis. Above T_c , the paraelectric crystalline structure is hexagonal, essentially consisting of a statistical combination of TT , TG and TG' rotational isomers [34]. In the hexagonal (paraelectric) phase the chain molecules are very mobile along the chain axis as in a 1D liquid crystal [137]. Thick lamellar crystals (extended chain crystals) are grown extensively in the films when they are crystallized by annealing in the hexagonal phase. The Curie transition has been found to involve intra-molecular changes of dipole directions that modify the polar all-trans conformation to a somewhat disordered arrangement. The disappearance of the ferroelectric phase above T_c implicates drastic conformational changes from the *trans* to *gauche* states, accompanied by a rotational motion of the chains around the chain axis. It was shown that defects play an important role, so that the Curie temperature [138] has a strong dependence on composition ratios of VDF and TrFE [30, 35].

Although the ferroelectric phase occurs in the copolymer P(VDF-co-TrFE) at room temperature without the need of additional electric poling or stretching, the unit cells orientate randomly in the semicrystalline polymer. To induce the piezoelectricity or pyroelectricity, it must be electrically poled. Electrical poling can be accomplished by applying an electric field across

the polymer. Usually, an electric field on the order of $50 \text{ MV}/m$ is typically sufficient to effect crystalline orientation. Polymer poling can be accomplished using a direct contact method or a corona discharge. It has been shown by X-ray [139, 140, 141, 142], electric displacement [125, 143, 144] and infrared measurements [145, 139, 146] that the strong polarization imparted to the copolymer is mainly associated with ferroelectric dipole reorientation in the crystalline region. Ferroelectric switching of the polarization in the crystals has also been widely studied. Kepler and Anderson [141] have suggested a model related to the pseudo-hexagonal character of the β -phase crystals so that polarization occurs by rotations of the polar axis (which is the b axis in the orthorhombic unit cell) in 60° increments. A similar mechanism, proposed by Broadhurst *et al.* [147], argues for a six-site potential-well cooperative model. Much experimental evidence has since confirmed that the dipoles of β -phase of P(VDF-co-TrFE) are oriented by 60° steps in the direction of the poling field [148, 142, 30, 149, 150].

In many applications of P(VDF-co-TrFE) ferroelectric copolymers such as data storage and memory devices, the thickness of the polymer films should be as thin as possible so that the operation voltage can be low and this lower thickness limit is determined by the thickness at which the ferroelectric response remains relatively high. So, the issues of how the functional properties change as the film thickness is reduced and what is responsible for these changes are of great concern. It has been shown [151, 152] that there exists a threshold thickness (d_{th}) of crystallization below which the crystallinity of the films drops precipitously in spin cast films of P(VDF-co-TrFE) copolymer. The direction correlation between (d_{th}) and the crystal lamellar size D in the (200/110) direction suggests that the latter is the threshold size for the stable crystallites growing in the thin films with polymer chains preferably lying in parallel to the substrate [152]. When confined within the pores walls of porous templates, as we will see later by the XRD results (c.f. section 6.3.3), the (200/110) direction of P(VDF-co-TrFE) is along the tube axis which has a length on the order of tens of μm . That means, the ferroelectric properties of P(VDF-co-TrFE) are always conserved in 1D structures even though the thickness of the tubes or the diameter of the wires is smaller than the threshold thickness d_{th} .

6.2 Fabrication of P(VDF-co-TrFE) copolymer nanotubes

We selected random P(VDF-co-TrFE) copolymers of composition 75/25 as the target material. The copolymers were supplied by *Piezotech S.A. St. Louis - France*.

To prepare the P(VDF-co-TrFE) nano-objects by melt-wetting, a porous template was placed in the furnace under an argon atmosphere. Then, the P(VDF-co-TrFE), in the form of a thin film, was placed on the top side of the porous template at a temperature of 180°C well above its melting point. After a short exposure time ($\sim 10 \text{ min}$) at this temperature, a cooling protocol was applied with a properly chosen rate. In order to assist good crystallization, we selected a cooling rate of $1 \text{ K}/\text{min}$ under argon atmosphere. After the sample was cooled completely to room temperature, the residual material on the top surface of the template was carefully removed by a scalpel. A subsequent solvent dip N,N-dimethylformamide (DMF) at 60°C was applied, if necessary. At this point, the P(VDF-co-TrFE) embedded porous alumina chips with different parameters were ready for XRD or DSC experiments. The latter can also be performed on released tubes (as will be discussed in section 6.3.2). Instead of nanotubes, solid nanowires are found when the diameter is below 60 nm .

6.3 Characterization of P(VDF-co-TrFE) copolymer nanotubes

6.3.1 Morphology

Figure 6.3 depicts bundles of nanotubes made from P(VDF-co-TrFE) with different diameters from different templates. Those with $1\ \mu\text{m}$ diameter (figure 6.3a) were obtained from macroporous silicon and those with $180\ \text{nm}$ (figure 6.3b) from porous alumina. All of them have very smooth outer pore walls and high aspect ratios. As these P(VDF-co-TrFE) copolymer nanotubes are non-conductive, which leads to an accumulation of electrons at their surface during the SEM investigations, relatively low acceleration voltages ($1.5 \sim 5\ \text{eV}$) were employed. Similarly to the results obtained in case of nanotubes consisting of α -PVDF [40], the wall thickness of the P(VDF-co-TrFE) nanotubes is estimated to be around $30\ \text{nm}$ provided their diameter is larger than $60\ \text{nm}$.

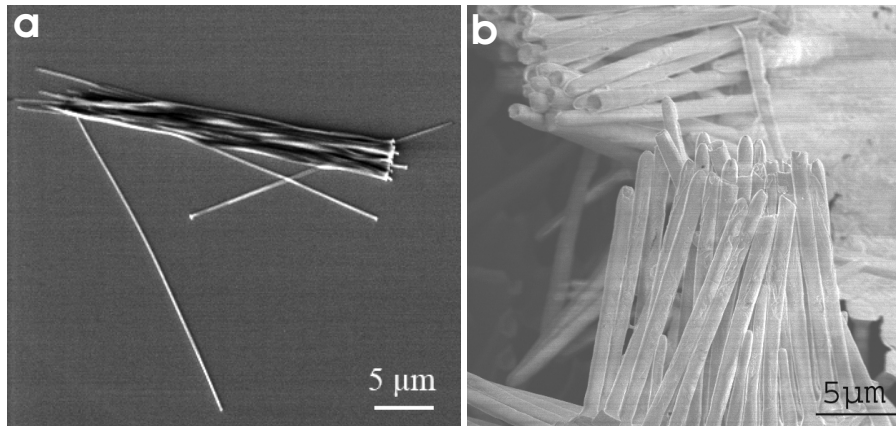


Figure 6.3: SEM image on bundles of P(VDF-co-TrFE) nanotubes with a diameter of (a) $180\ \text{nm}$ and (b) $1\ \mu\text{m}$.

6.3.2 DSC investigations

DSC of P(VDF-co-TrFE) nanotubes embedded in porous templates

A first series of samples used for DSC measurements was prepared in such a way that the P(VDF-co-TrFE) nanotubes and nanowires were still embedded in the porous alumina templates with the top surface film carefully removed by a sharp scalpel. The sizes of all the samples were adjusted to fit into the DSC pan. As a reference sample, a thin film of P(VDF-co-TrFE) copolymer was first measured in the DSC furnace. Then, P(VDF-co-TrFE) nanotubes and nanowires embedded in the porous alumina templates with different D_p -values, respectively $25\ \text{nm}$, $60\ \text{nm}$, $180\ \text{nm}$, and $400\ \text{nm}$, were consecutively measured within the template for a temperature range from 30°C to 200°C . As the DSC signal depends on the thermal history, a first heating run was performed on the P(VDF-co-TrFE) nanotubes prepared in the manner described in section 6.2. It was followed by a cooling run and consecutively a second heating run. The heating and cooling rates were $20\ \text{K}$ per minute. The results are listed in the tables 6.1, 6.2 and figures 6.4, 6.5. For reason of clarity, in all the DSC curves in this section (figures 6.4, 6.5, 6.6), both of the endothermic peaks in the heating runs and the exothermic peaks in the cooling runs point upwards.

	1 st heating run		Upon cooling		2 nd heating run	
	T_m	T_c	T_{cryst}	T_c	T_m	T_c
thin film	149.5°C	126.8°C	133.1°C	78.8°C	146.8°C	126.7°C
25 nm	145.5°C	104.2°C	132.8°C	78.1°C	145.2°C	123.0°C
60 nm	139.3/150.9°C	97.6°C	132.8°C	78.1°C	148.3/150.6°C	127.6°C
180 nm	150.0°C	129.0,° C	114.4°C	76.5°C	149.0°C	129.0°C
400 nm	149.6°C	127.0°C	133.4°C	78.7°C	150.6°C	126.6°C

Table 6.1: Characteristic temperatures of P(VDF-co-TrFE) copolymer as bulk thin film as well as nanotubes and nanorods with different diameters. T_m stands for the peak temperature for melting in the heating run. T_{cryst} stands for the peak temperature for solidification. T_c stands for the temperature where the phase transition ferroelectric-paraelectric happens in the heating runs and paraelectric-ferroelectric happens in the cooling run.

In all the curves in figure 6.4 and figure 6.5, on heating, the thermograms show two endothermic peaks, one at Curie transition, T_c (on heating up run 1), and the other one at the melting temperature T_m (on heating up run 1). These copolymers present a thermal hysteresis behavior. During cooling, the exothermic peaks appearing upon solidification, the crystallization peak at T_{cryst} (on cooling down run) and the paraelectric-ferroelectric transition at the Curie point T_c (on cooling down run), are shifted towards the lower temperature side. The Curie transition appears in all the DSC curves as a broad peak, extending over a temperature range, especially upon cooling. At room temperature, one observes the ferroelectric phase. With increasing temperature, the paraelectric phase appears, and at higher temperatures one obtains the disordered molten state.

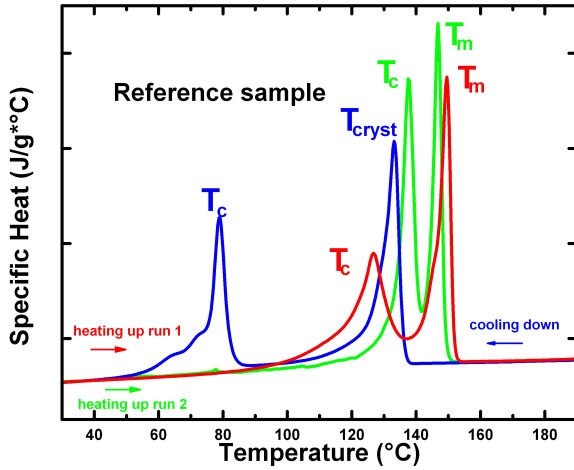


Figure 6.4: DSC curves (during first heating up run then followed by a cooling down run and a second heating up run) copolymer in the form of bulk thin film. All the heating up and cooling down rates were 20K per minute. One scale division represents 2 J/g * C.

Table 6.1 summarizes the ferroelectric-paraelectric and paraelectric-ferroelectric phase-transition temperatures (T_c), as well as peaks of melting and solidification temperatures (T_m and T_{cryst}) which are determined by the temperature at which the heat capacity has the highest value. The onset temperatures of melting and solidification temperatures (T'_m and T'_{cryst}), which are determined as the intersection between the rising and the dropping slopes of the peak and the base line, are listed in the table 6.2. These values were obtained upon both heating up and cooling down runs for P(VDF-co-TrFE) polymer as bulk as well as in the pores of porous alumina. The T_m and T_{cryst} values of the copolymers nanotubes and nanorods are close to those of bulk thin film, but much lower than those of both homopolymers.

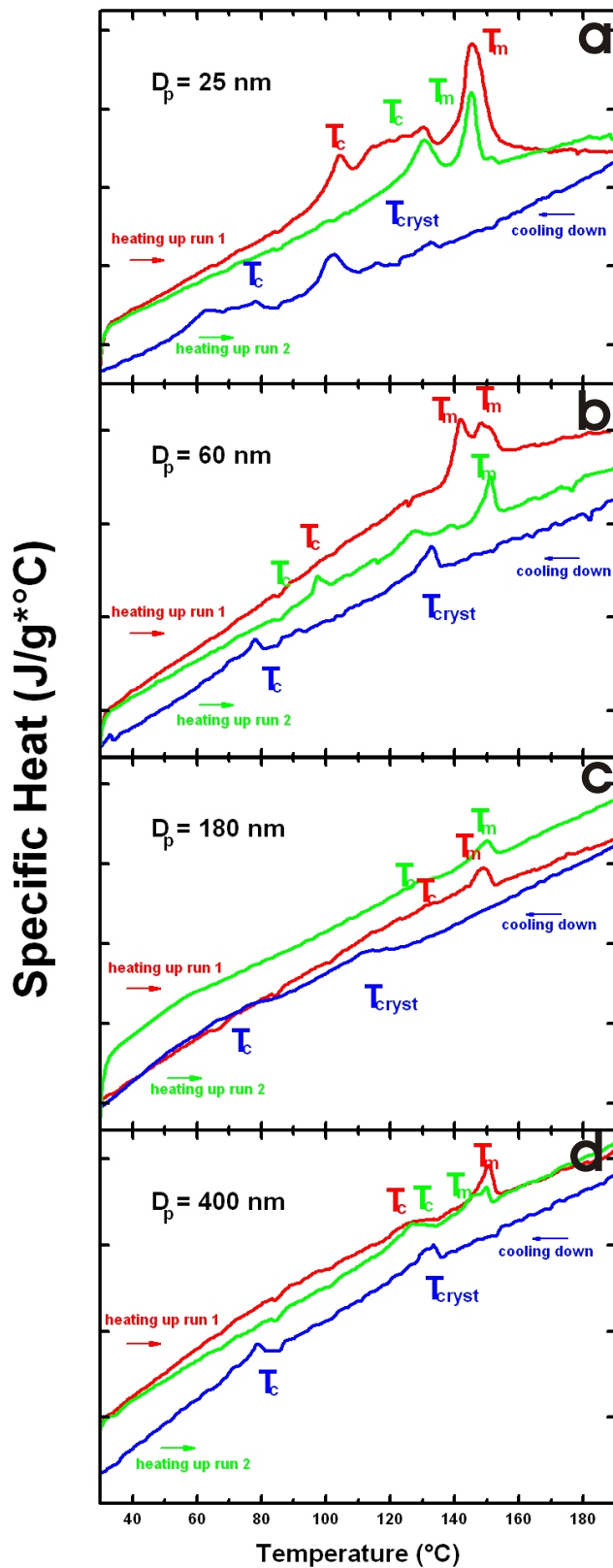


Figure 6.5: DSC curves (during first heating up run then followed by a cooling down run and a second heating up run) for P(VDF-co-TrFE) copolymer either in the form of nanotubes or nanowires embedded in porous alumina templates with different D_p -values, respectively: (a) 25 nm, (b) 60 nm, (c) 180 nm, and (d) 400 nm. All the heating up and cooling down rates were 20K per minute. One scale division in (a), (b), (c) and (d) represents 0.04, 0.04, 0.03 and 0.03 $J/g * C$ respectively.

	1 st heating run	Upon cooling	2 nd heating run
	T'_m	T'_{cryst}	T'_m
thin film	141.2°C	136.0°C	145.7°C
25 nm	140.1°C	108.1°C	130.2°C
60 nm	145.1/127.6°C	135.6°C	147.5°C
180 nm	142.3°C	120.2°C	142.3°C
400 nm	149.6°C	135.5°C	141.5°C

Table 6.2: Characteristic temperatures of P(VDF-co-TrFE) copolymer as bulk thin film as well as nanotubes and nanorods with different diameters. T'_m stands for the onset temperature for melting in the heating run which is determined by the intersection temperature between the rising slope of the peak and the base line. T'_{cryst} stands for the onset temperature for solidification which is determined by the intersection temperature between the dropping slope of the peak and the base line.

	1 st heating run		Upon cooling		2 nd heating run	
	T_m	T_c	T_{cryst}	T_c	T_m	T_c
25 nm	143.8°C	132.1°C	127.3°C	77.9°C	143.8°C	130.8°C
60 nm	144.0/151.0°C	131.0°C	126.7/133.3°C	79.7°C	144.3/150.0°C	130.6°C
180 nm	146.7°C	123.1°C	130.3°C	78.3°C	145.1°C	129.5°C
400 nm	150.4°C	123.8°C	132.7°C	79.3°C	149.0°C	127.7°C

Table 6.3: Characteristic temperatures of released P(VDF-co-TrFE) nanotubes and nanorods with different diameters. T_m stands for the peak temperature for melting in the heating run. T_{cryst} stands for the peak temperature for solidification. T_c stands for the temperature where the phase transition ferroelectric-paraelectric happens in the heating runs and paraelectric-ferroelectric happens in the cooling run.

DSC of released P(VDF-co-TrFE) nanotubes and their relative crystallinity

DSC scans were also performed on released P(VDF-co-TrFE) nanotubes and nanowires with different D_p -values, respectively 25 nm, 60 nm, 180 nm, and 400 nm. The suspension of P(VDF-co-TrFE) in HPLC-grade ethanol was first dropped into the pan of the microfurnace. After the ethanol had evaporated, the weight of the P(VDF-co-TrFE) nanotubes was measured. Then, the DSC was carried out for a temperature range from 30°C to 200°C in three steps:

- A first heating run with a rate of 20 K/min, during which the specific heat was measured on freely released tubes. When this step was over, the tubes were molten.
- A cooling run with a rate of 20 K/min.
- A second heating run with a rate of 20 K/min, during which the calorimetry from the molten state of P(VDF-co-TrFE) was measured.

The results are presented in the tables 6.3, 6.4 and figure 6.6.

Tables 6.3 summarizes the values of T_c , T_m and T_{cryst} (which are defined and determined as in the case of the hybrid system in table 6.1) for released P(VDF-co-TrFE) polymer nanotubes prepared by the protocols described in section 6.2. The corresponding values of T'_m and T'_{cryst} (which are defined and determined as in the case of the hybrid system in table 6.2) are listed in the table 6.4.

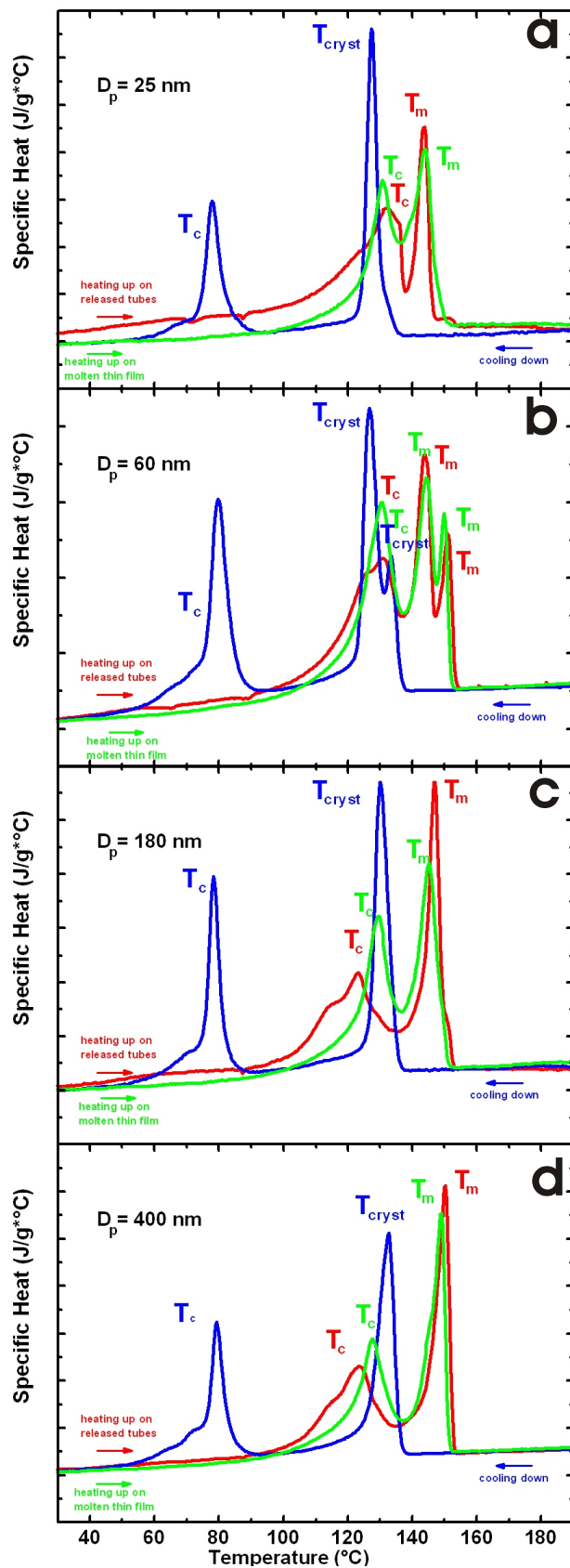


Figure 6.6: DSC curves (during first heating up run then followed by a cooling down run and a second heating up run) for P(VDF-co-TrFE) copolymer either in the form of released tubes or in the molten state for different D_p -values, respectively: (a) 25 nm, (b) 60 nm, (c) 180 nm, and (d) 400 nm. The red, blue and green curves represent the heating on released tubes, cooling from the molten state and second heating on the molten state, respectively. One scale division in all the images represents 1 J/g * C.

	1 st heating run	Upon cooling	2 nd heating run
	T'_m	T'_{cryst}	T'_m
25 nm	139.6°C	124.1°C	135.2°C
60 nm	138.1/144.1°C	122.6/136.3°C	136.7/143.5°C
180 nm	142.9°C	126.8°C	137.2°C
400 nm	143.6°C	125.8°C	139.2°C

Table 6.4: Characteristic temperatures of released P(VDF-co-TrFE) nanotubes and nanorods with different diameters. T'_m stands for the onset temperature for melting in the heating run which is determined by the intersection temperature between the rising slope of the peak and the base line. T'_{cryst} stands for the onset temperature for solidification which is determined by the intersection temperature between the dropping slope of the peak and the base line.

Discussion of DSC results

In both figures 6.5 and 6.6, the peaks of T_c and T_m are not correlated. The specific heat curves in figure 6.5 of the P(VDF-co-TrFE) copolymer nanotubes and nanorods with different D_p -values have different signal-to-noise ratios. The reason is that different pore sizes and porosities of the templates induce different filling factors for the copolymer, that is, the volume fraction of the sample occupied by the polymer. The filling ratio decreases in the following sequence: $D_p = 60\text{ nm} > D_p = 25\text{ nm} > D_p = 400\text{ nm} > D_p = 180\text{ nm}$. The different filling factors result from the fact that the tubes coating the porous alumina always have a wall thickness of around 30 nm for $D_p \geq 60\text{ nm}$ while the porous alumina templates with a D_p -value of 25 nm is completely filled. Thus, the quantities of materials measured for different values of D_p are different, leading to a different signal-to-noise ratio.

In figure 6.6 where only released copolymer tubes or wires were measured, the combined area of the melt-paraelectric phase as well as the paraelectric/ferroelectric phase transitions can be regarded as a measure of the relative crystallinity, even though both transitions cannot be separated. So, in the calculations on the ratios of the areas below the melt-paraelectric phase as well as below the paraelectric/ferroelectric phase for the P(VDF-co-TrFE) in their released state prepared by the protocols described in section 6.2 and after being heated up at a rate of 20 K per minute, the sum of the areas were taken into account. An estimation on the relative crystallinity of the released tubes to their molten states gives 2.56, 1, 1.31 and 1.16 for different D_p -values of 25 nm , 60 nm , 180 nm and 400 nm , respectively.

The melting points T_m , which are related to the paraelectric high-temperature phase, are influenced by the curvatures and geometric constraints imposed by the pore shape which act as strong confinement. As stated earlier, whereas tubes are being expected for D_p -values of 180 nm and 400 nm , the template pores accommodate solid P(VDF-co-TrFE) nanorods when D_p is decreased to a value smaller than twice the wall thickness of the tubes. The D_p -value of 60 nm lies in the crossover range from nanotubes to nanorods, and in case of a D_p -value of 25 nm a complete filling of the pore space is to be expected. Thus, the growing crystallites within the pores are subjected to different degrees of geometric constraint. The pores are infinite in the direction of their long axes, but any direction perpendicular to the structure formation processes are confined. This should influence the actual size of the P(VDF-co-TrFE) crystallites and in turn their melting temperature T_m , which we define as the position of the maxima of the melting endotherms in the DSC curves.

As shown in figure 6.6, and listed in table 6.3, for D_p -values of 25 nm , 180 nm and 400 nm , single melting peak appears with T_m -values of 144°C , 147°C , and 150°C . However, a double

peak with $T_m = 144^\circ\text{C}$ and 151°C occurs in case of the sample liberated from ordered porous alumina with a D_p -value of 60nm . We interpret these findings as a signature of a crossover from a solid to a tubular structure, as D_p -value increases. Even in case of ordered porous alumina, the distribution of the D_p -values exhibits a certain dispersity, calculated by dividing the standard deviation by the mean pore diameter, of around 8%. Therefore, some pores are large enough to accommodate tubes (as sketched in figure 6.7a) whereas the hollow space of the smaller pores is completely filled (as sketched in figure 6.7b). The low temperature peak of the 60nm sample and the single peak of the 25nm sample virtually have the same position ($T_m = 144^\circ\text{C}$), indicating that they originate from the melting of crystallites with the essentially the same size. We conclude that the low-temperature peak originates from tubes formed in the larger fraction of the porous alumina templates with a mean D_p -value of 60nm , where the thickness of the tube wall is of the order of 30nm , which leads along with the strong wall curvature to a confinement similar to that in the 25nm pores. The position of the high-temperature melting peak of the 60nm sample ($T_m = 151^\circ\text{C}$) corresponds to the single melting endotherms of the bulk reference sample (6.4) and the 400nm sample. Thus, the confinement exerted on the crystallites is not as pronounced and consequently the crystallites can adopt a larger size. This is because in case of a complete filling of the pore volume the additional confinement due to the inner tube wall vanishes so that the lamellae can grow across the entire pore diameter of 60nm . The important conclusion one can draw from these results is that the thickness of the tube walls must be in the order of 30nm . The peak T_m -values of the melting peak we ascribe to the tube fraction of the 60nm sample and the single melting endotherms of the 180nm and 400nm samples are shifted from 144°C to 147°C to 150°C as D_p -value increases. Since previous investigations on PVDF homopolymer tubes revealed that there is no fundamental change in the wall thickness as D_p -value increases to 400nm [40], we conclude that a decrease in curvature facilitates the growth of the crystallites.

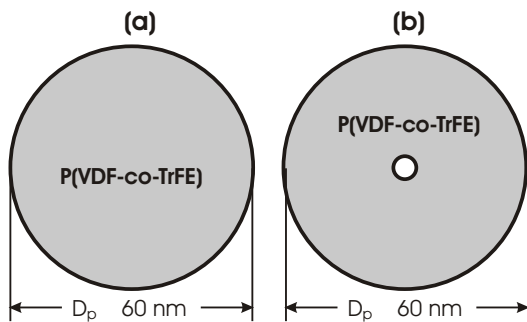


Figure 6.7: A sketch of P(VDF-co-TrFE) copolymer within the confinement of porous alumina with a pore diameter D_p of 60nm . The copolymer could either adopt a form (a) as wires or (b) as tubes.

Moreover, an endothermic peak occurs which can be assigned to the characteristic first order transition from the pseudo-hexagonal ferroelectric to the paraelectric phase in all DSC scans for different D_p -values of 25nm , 60nm , 180nm , and 400nm . The Curie point T_c , which is defined as the position of the peak maximum, amounts to 132.1°C , 131.0°C , 123.1°C and 123.8°C for D_p -values of 25nm , 60nm , 180nm , and 400nm , respectively. It is obvious that the Curie point is shifted to lower values when the crossover from a rod-like (in case of D_p -values of 25nm and 60nm) to a tubular structure (in case of D_p -values of 180nm and 400nm) occurs. This confirms again our conclusion that an increase in curvature is less favorable for the growth of the crystallites.

6.3.3 XRD results on unpoled P(VDF-co-TrFE) embedded in porous alumina

To gain further information on the internal morphology of the as-prepared P(VDF-co-TrFE) nanotubes before any electrical poling, XRD experiments were performed on nanorods and nanotubes of P(VDF-co-TrFE) aligned within the template pores. We used alumina templates for this purpose since there are no disturbing reflections originating from the template material at 2Θ values smaller than 43° . Samples were prepared in such a way that only the internal pore walls were coated by P(VDF-co-TrFE) but not the surface with pore openings. The residual P(VDF-co-TrFE) film on the template surface was removed from the top of the template completely by a scalpel. The P(VDF-co-TrFE) nanotubes and nanowires embedded in the template are perfectly aligned, and textures should be able to be detected, if there are any. The XRD set-up used was the same as depicted in figure 4.1. Both 2Θ and Ψ scans were carried out. The experimental procedures were described in section 4.2.2.

The 2Θ scans

In all the 2Θ scans obtained, no other crystal phase than the low-temperature phase was present. The XRD patterns for pore diameters of 25 nm , 60 nm , 180 nm and 400 nm are shown in figure 6.9. The obtained peak intensities depend not only on the degree of crystallinity of the nano-objects, but also on the filling ratio. The pseudo-hexagonal symmetry of the low-temperature phase results in several composite diffraction peaks. In a single low-temperature crystal, the crystalline planes of the (110/200) and of the (310/020) composite reflections are inclined at approximately 60° to each other (as schematically depicted in figure 6.8).

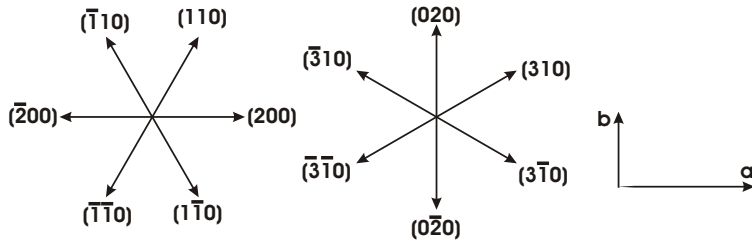


Figure 6.8: The directions of the plane normals in the crystal as seen along the c axis [153].

The unit cell of this phase contains two monomer units from two molecular chains. There is 75 % probability that each monomer unit is a VDF segment and a 25 % probability that it is a TrFE segment. The orthorhombic unit-cell dimensions were then taken to be $a = 8.82\text{ \AA}$, $b = 5.13\text{ \AA}$ and $c = 2.55\text{ \AA}$ (see table 6.5). According to these values, all the peaks appearing on the diffraction diagram can be assigned to specific crystal planes by the relation: $\sin \Theta = \frac{\lambda}{2} \sqrt{\left(\frac{h}{a}\right)^2 + \left(\frac{k}{b}\right)^2 + \left(\frac{l}{c}\right)^2}$, where Θ is the diffraction angle, $\lambda = 1.5405\text{ \AA}$ is the Cu $K\alpha$ radiation and (hkl) represents the Miller indices of lattice planes.

As can be noted in figure 6.9, the broad shoulder on the low-angle side of the peak ($2\Theta \sim 18.1^\circ$) is due to scattering from the amorphous regions of the material [153]. It is particularly pronounced in the diffractograms of P(VDF-co-TrFE) nanotubes with a diameter of 25 nm and 60 nm . This is related to the increasing contribution of amorphous interfaces as the interface-to-volume ratio increases with decreasing D_p . Similar observations have been made when the thickness of thin P(VDF-co-TrFE) films was decreased [154]. The peak positioned at $2\Theta = 19.8^\circ$ corresponds to the reflections from the (200/110) planes. At $2\Theta = 35.25^\circ$, the position of both the (001) and (310/020) reflections, only very weak peaks appear, if at all. According to the literature, at $2\Theta = 40.85^\circ$, reflections also appear which correspond to the (400) and

(220) planes. The different signal-to-noise ratios for the XRD patterns come again from the fact that different pore sizes and porosities of the templates induce different filling factors for the copolymer (c.f. section 6.3.2).

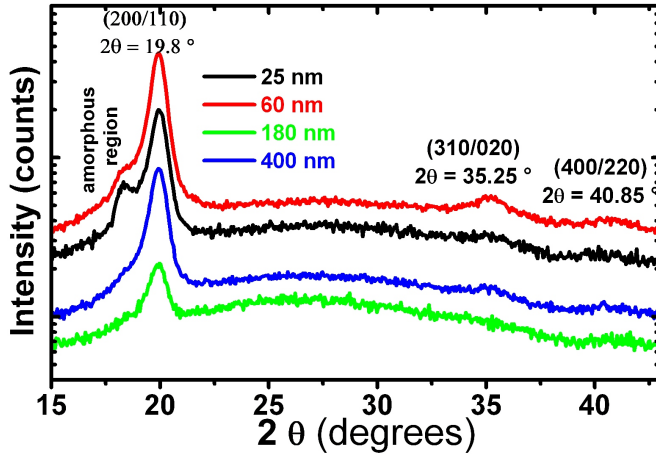


Figure 6.9: $\Theta/2\Theta$ scans of porous alumina templates wetted by P(VDF-co-TrFE) copolymer with different pore diameters: $D_p = 25 \text{ nm}$ in black, $D_p = 60 \text{ nm}$ in red, $D_p = 180 \text{ nm}$ in green and $D_p = 400 \text{ nm}$ in blue. Three different sets of peaks can be seen in comparison to the literature [153], respectively the (200/110) plane with $2\Theta = 19.8^\circ$, the (310/020) plane with $2\Theta = 35.25^\circ$ and the (400/220) plane with $2\Theta = 40.85^\circ$. One scale division represents 1000 counts.

Table 6.5: Unit cell dimensions of β -form PVDF, TrFE and P(VDF-co-TrFE) copolymer in a proportion of 75/25 [155].

β -form of PVDF	TrFE	P(VDF-co-TrFE) 75/25
a=5.58Å	a=9.52Å	a=8.82Å
b=4.91Å	b=5.78Å	b=5.13Å
c=2.56Å	c=2.55Å	c=2.55Å

The Ψ scans

In accordance with literature [34], Ψ scans were performed for values of 2Θ corresponding to reflections having a relatively large intensity, respectively 18.3° , 19.8° , 35.25° and 40.85° corresponding to the amorphous region, (200/110), (310/020) and (400/220) composite reflections, in turn, for the samples with $D_p = 25 \text{ nm}$, 60 nm , 180 nm and 400 nm . The scattered intensities versus the tilting angle Ψ are shown in figure 6.10 for P(VDF-co-TrFE) nanotubes and nanorods with different diameters. The obtained results were qualitatively the same for all the D_p -values.

In the diffractograms of all the four samples, for a 2Θ value of 19.8° corresponding to the (200/110) reflections, an intensity maximum occurred at $\Psi = 0^\circ$. This means that either the (200) or the (110) lattice planes are arranged parallel to the template surface and thus perpendicular to the long axes of the template pores and the P(VDF-co-TrFE) copolymer nanotubes, respectively. Therefore, the a axis, or the $\langle 110 \rangle$ direction of the unit cell of P(VDF-co-TrFE) is predominantly oriented parallel to the long axis of the nanotubes, and most of the crystallites are arranged such that they contribute to the scattering intensity only if Ψ equals to zero. Considering the geometric confinement of the pore walls, the only direction which has zero curvature is along the long axis of the nanotube walls. If a cross-section of P(VDF-co-TrFE) nanotubes perpendicular to the long axis is considered, the orientation of the $\{h00\}$ or $\{110\}$ lattice planes remain invariant for any position within the wall, respectively. In contrast, all the other lattice planes alter their orientation relative to that at a reference point on the nanotube wall.

For a 2Θ value of 40.85° , a pronounced peak around $\Psi = 60^\circ$ occurred. Theoretically, the interplanar angles among different crystallite planes can be calculated (results listed in the table

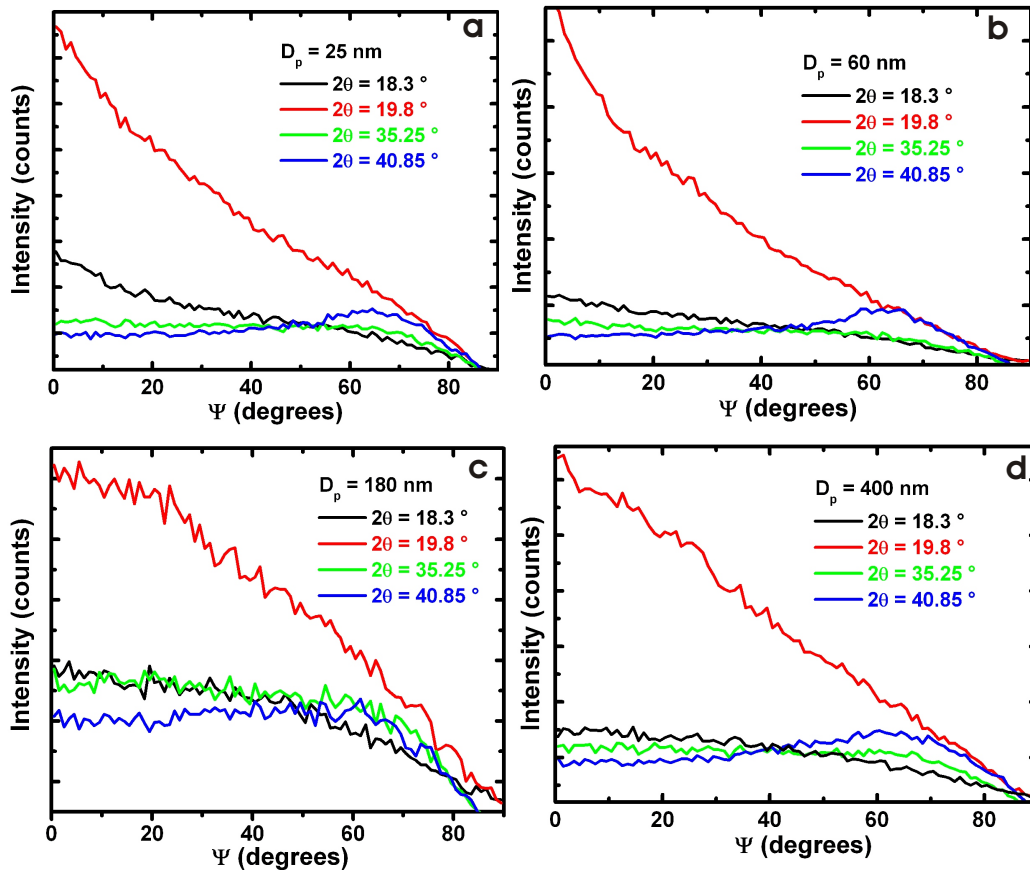


Figure 6.10: Ψ scans of P(VDF-co-TrFE) coated porous alumina templates with different D_p -values, respectively: (a) 25 nm, (b) 60 nm, (c) 180 nm and (d) 400 nm, respectively, in the reflection mode with fixed 2θ values of 18.1° , 19.8° , 35.25° , and 40.85° , correspondingly.

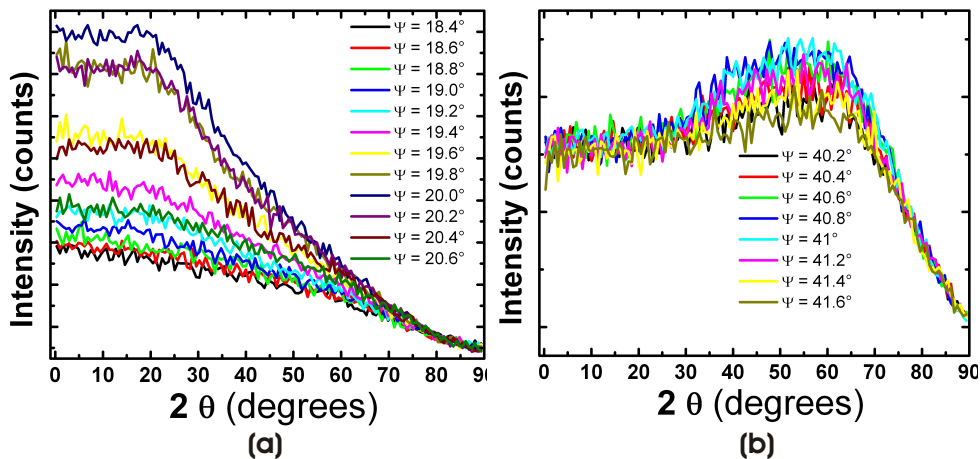


Figure 6.11: Ψ scans of P(VDF-co-TrFE) embedded in porous alumina templates with a pore diameter of $D_p = 400$ nm, in the reflection mode as described before and with series of 2θ values from (a) 18.4° to 20.6° , and (b) 40.4° to 41.6° respectively, both with a 2θ increment of 0.2° . One scale division corresponds to 100 counts.

6.6). From the table, five different Ψ values, respectively 0° , 19.2° , 59.8° , 79.03° and 90° can be present on the Ψ scan diagram. Among them, $\Psi = 59.8^\circ$ can be obtained from the highest number of possible combinations of different crystal planes. This explains partially that peak in the experimental Ψ scan diagram is most pronounced.

Note that the Ψ scan curves for $2\Theta = 19.8^\circ$ and $2\Theta = 40.85^\circ$ do not show the same textures, even though the sinusoidal value of the latter is almost double the corresponding value of the former. Considering the pseudo-hexagonal polar packing of the crystallites in P(VDF-co-TrFE), we speculate that the Ψ scan for $2\Theta = 19.8^\circ$ might hit more on one of the two planes, either (200) or (110), while the Ψ scan for $2\Theta = 40.85^\circ$ hits more on the complementary one of the corresponding higher order planes, either (220) or (400). In order to check this, two series of Ψ scans were carried out additionally for the P(VDF-co-TrFE) copolymer nanotubes embedded in the porous alumina template with $D_p = 400 \text{ nm}$. As shown in figure 6.11a and 6.11b, 2Θ angles were fixed for a series of values from 18.4° to 20.6° , and 40.4° to 41.6° respectively, both with a 2Θ increment of 0.2° . In both figures, qualitatively similar curves are seen. As stated in [153], the relative intensity (~ 10) of (400)-plane to (220)-plane when $2\Theta = 40.85^\circ$ is much higher than that (~ 0.625) of (400)-plane to (110)-plane when $2\Theta = 19.8^\circ$, we conclude that both of the corresponding Ψ scans are superpositions of two different curves, as sketched in figure 6.12. The superposition of two first order peaks, respectively (110) and (200), give the form of the Ψ scan curve for $2\Theta = 19.8^\circ$ (c.f. figure 6.12a). While the corresponding second order peaks, respectively (220) and (400), having smaller intensities but with a different relative intensity than the first order ones, the Ψ scan curve for $2\Theta = 40.85^\circ$ adopts the form as in the figure figure 6.12b.

Table 6.6: Interplanar angles between different couples of crystal planes.

Crystal planes	(200)	(110)	(310)	(020)	(400)	(220)
(110)	59.8°					
(310)	79.03°	19.21°				
(020)	90°	59.8°	79.03°			
(400)	0°	59.8°	79.03°	90°		
(220)	59.8°	0°	19.21°	59.8°	59.8°	
(001)	90°	90°	90°	90°	90°	90°

For 2Θ values of 18.3° (correspondingly amorphous region) and 35.25° (correspondingly (001) and (310/020) reflections), no peaks appear in the Ψ scans. However, this cannot exclude the possibility that the (001) reflection shows a texture. This is because the sensibility of XRD set-up dramatically decreases at that point as the X-ray spot size increases strikingly as long as the tilting angle (Ψ value) is larger than 70° .

Proposed structure models of the P(VDF-co-TrFE) within the template wall confinement

Taking into account the orthorhombic crystalline form of the unit cell of the P(VDF-co-TrFE), two structural models, as shown in figure 6.13, can be proposed from the results of the XRD investigations. The growth mechanism of the crystal within the pore walls can be speculated to occur in such a way that the crystallographic c axis is always perpendicular to the long axis of the pores. In the first model, depicted in figure 6.13a, the a axis as the major growth axis is oriented parallel to the long axis of the pores, while b and c axes can adopt any orientation as long as being perpendicular to the a axis. An alternative model, depicted in figure 6.13b, the

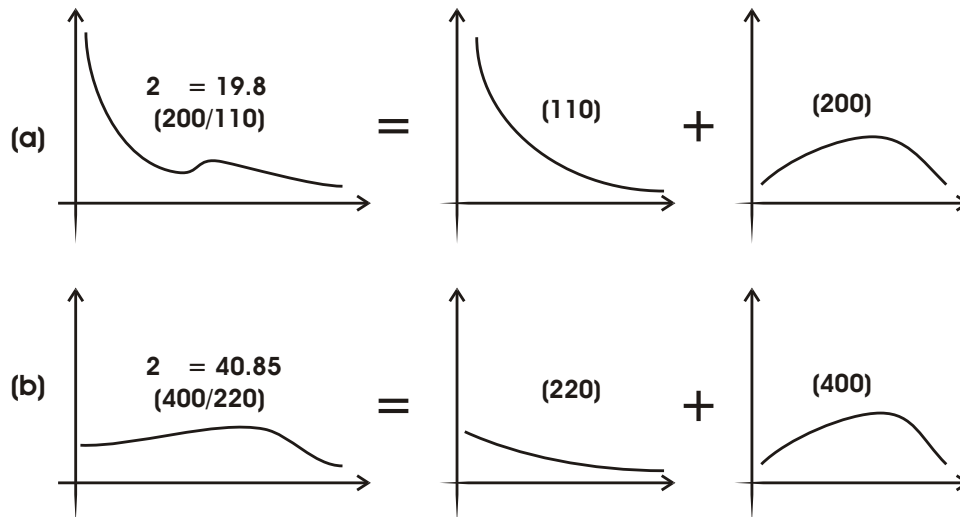


Figure 6.12: Sketches to show that the Ψ scans for (a) $2\theta = 19.8^\circ$ and (b) $2\theta = 40.85^\circ$ could be superpositions of two different curves with different relative intensities.

a axis and the b axis have an angle of 60° and 30° to the long axis of the pores while both are perpendicular to the c axis, and the $\langle 110 \rangle$ direction is aligned with the long axis of the tubes.

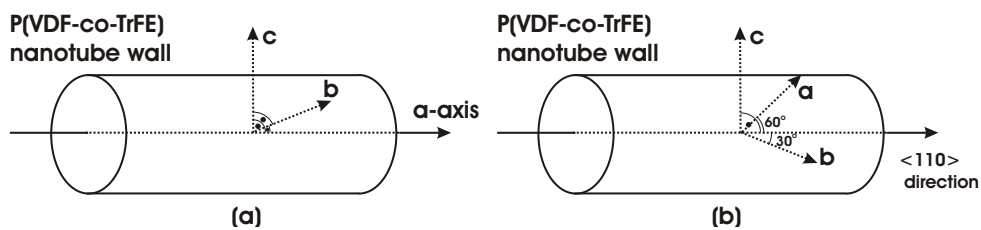


Figure 6.13: Proposed structural models for the growth of P(VDF-co-TrFE) crystallites within the confinement of pore walls.

6.3.4 Ferroelectric properties

Prior to poling, ferroelectric polymers usually do not show a net polarization and are thus not piezo- or pyroelectric. This must be attributed to the fact that the semicrystalline materials have randomly oriented crystalline domains in the unpoled state. This is an important difference from ferroelectric crystals in which the residual polarization arises from the displacement of specific atoms within the unit cell. To get a residual polarization in ferroelectric polymers, the dipoles must be rotated together around the chain axis. This can be realized by electric field poling. The process does not involve a reorientation of the domains as a whole since neighboring crystallites are interconnected by the chains and thus hindered in their motion. As a result, the conformation changes locally.

In order to characterize the electric properties of P(VDF-co-TrFE) nanotubes, topology investigations by AFM, poling and piezoelectric characterization adopted by PFM were carried out. Different information on the morphology, domain walls and orientation was obtained on the individual P(VDF-co-TrFE) nanotubes.

Topology investigation of P(VDF-co-TrFE) nanotubes by AFM

AFM performed in contact mode with a conductive TiN-coated cantilever (*MakroMasch*), a force constant of about 0.25 N/m and a tip with a radius of curvature of $R < 30 \text{ nm}$, was used to investigate the morphology of the nanotubes lying on a mica plane. They were deposited on gold-coated mica by dip coating from a suspension of ethanol. Figure 6.14a and 6.14d show the topography of a bundle of P(VDF-co-TrFE) nanotubes with a diameter of 180 nm and an individual P(VDF-co-TrFE) nanotube with a pore diameter of around 400 nm recorded by AFM, respectively. The different color contrasts represent the height of the measured point relative to the surface of the glass slide.

Poling of P(VDF-co-TrFE) nanotubes

In order to obtain a piezoelectric behavior, the P(VDF-co-TrFE) copolymer nanotubes, which showed no net piezoelectric activities as-prepared, have to be polarized by a strong electrical field. This can also be done by AFM with a conductive probing tip in the contact mode. By applying a small dc voltage between the tip and bottom electrode, an electric field of several hundred kV per cm can be generated, which is high enough to induce local polarization reversal in most ferroelectrics. A tip, when positioned at a distance d from the surface, generates a nonuniform electric field, and its normal component at the sample surface, E_z , can be estimated as a function of distance x from the tip axis as $E_z = 2RUd/(d^2 + x^2)^{3/2}$, where U is the applied voltage. A series of successive applications of rectangular voltage pulses were applied to the P(VDF-co-TrFE) copolymer nanotubes to pole them. This polarization induced in the sample remains after the removal of the electric field.

SFM characterization after poling

After poling, the resulting ferroelectric domains could be imaged by SFM. In the PFM mode, the voltages applied are much smaller than that used for poling. Information on both domain wall and orientation can be obtained:

- Domain wall information:

Figures 6.14b and 6.14e show well-resolved sub- μm domains along the long axes of the tubes (for 180 nm and 400 nm diameter P(VDF-co-TrFE) nanotubes, respectively) after the voltage had been switched back to zero subsequently to several poling procedures obtained at the same time as the topographical imaging of the same area. The domains were polarized by applying $\pm 15 \text{ V}$ for 180 nm and $\pm 36.5 \text{ V}$ for 400 nm P(VDF-co-TrFE) nanotubes, with a time duration of 2 s , respectively.

As mentioned in section 4.2.3, when the tip is passing a domain wall the piezoresponse is changing its sign, because domains with 180° phase lag respond oppositely to the application of an external electric field. As a result, the dark stripes in figure 6.14b that separate the white domains represent the domain walls. They have lateral dimensions on the order of $< 10 \text{ nm}$. In the measurement on the amplitude of piezoresponse, the domain wall is imaged with nearly zero response. Therefore, unpolarized regions beside the domains do not show a contrast as the brightness of the domains correlate with the magnitude of the piezoelectric constant. The resolution of detected domain wall is limited by the cantilever size. The domain walls also delineate the sizes of the domains, which are on the order of $0.5 \mu\text{m}$ for both the bundles of 180 nm and individual 400 nm P(VDF-co-TrFE)

nanotubes. That means, when the diameter of the tubes is much smaller than $0.5 \mu\text{m}$, domains comprising several tubes can be manipulated as an ensemble. In contrary, if the tubes adopt a diameter much larger than $0.5 \mu\text{m}$, domain structures can be created locally on different places on the outer tube walls.

- Information on domain orientation:

Figure 6.14c and 6.14f present the phase image of the same nanotubes shown in figure 6.14a and 6.14d respectively. It can be concluded that protrusions (bright areas) and depressions (dark areas) seen represent regions with antiparallel polarization vectors. By monitoring the phase of the piezoresponse signal, it was determined that bright regions in figure 6.14c and 6.14f, which vibrate in phase with the ac imaging voltage, represent negative domains (polarization is toward the bottom electrode), whereas dark regions correspond to positive domains with the polarization vector oriented upward, in contrast to figure 6.14b and 6.14e.

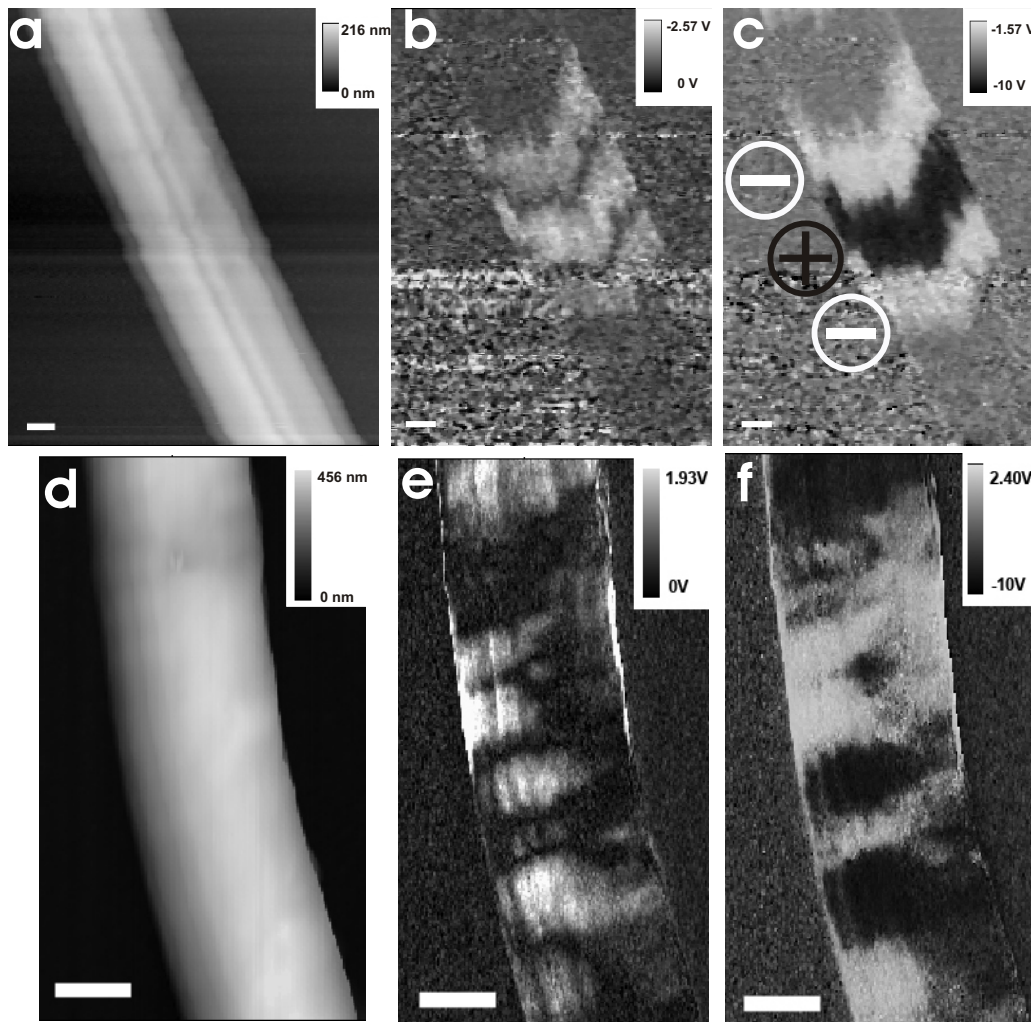


Figure 6.14: AFM and PFM characterization on a bundle of and on an individual P(VDF-co-TrFE) nanotubes with a 180 nm and 400 nm pore diameter, respectively. (a) AFM topography image; (b) PFM amplitude image; and (c) PFM on phase image on a bundle of 180 nm P(VDF-co-TrFE) nanotubes. The scale bar represents 100 nm in (a), (b) and (c). (d) AFM topography image; (e) PFM amplitude image; and (f) PFM on phase image on an individual P(VDF-co-TrFE) nanotube of a diameter of 400 nm . The scale bar represents 200 nm in (d), (e) and (f).

Note that the information on the orientation of domain regions detected by SFM in contact mode has not been detected in the charge image in figure 6.14b and 6.14e, where adsorbed charges completely screened polarization charges and hid the domain structure. These locally poled P(VDF/TrFE) nanotubes may be used as nanobarcodes with different domain orientations as the basic elements carrying information.

The possibility that the dipole moments can be poled by an external electric field and thus show a pronounced domain structure is related to the existence of a strong texture of P(VDF-co-TrFE) in tubular forms. As proposed in figure 6.13, two structure models could be adopted by P(VDF-co-TrFE) crystallites within the confinement of pore walls. In considering the six-site model [147] as well as that the b -axis is the polar axis, we conclude that only the model presented in figure 6.13b is possible. In this model, the b -axis, as the polar axis, could rotate freely when an external electric field is approaching by an AFM tip and give polarization domain structures on the outer tube walls.

Piezoelectric characterization of P(VDF-co-TrFE) nanotubes by PFM

High electric fields between the back electrode of the sample and the conductive AFM tip for poling induce significant capacitive forces which cause a cross talk [156] to the intended piezoresponse of the ferroelectric domains. Therefore, piezoelectric hysteresis loops were recorded by applying a series of rectangular voltage pulses with an interval of usually > 2 s in a triangular envelope. For the PFM signal used for the hysteresis loop, we selected only values after the individual voltage pulse already passed by. Thus the mentioned cross talk can be cancelled out because measurements were carried out under zero external (dc) voltage. The measured piezoresponse represents only the remanent polarization and thus these hysteresis loops are named *remanent loops*.

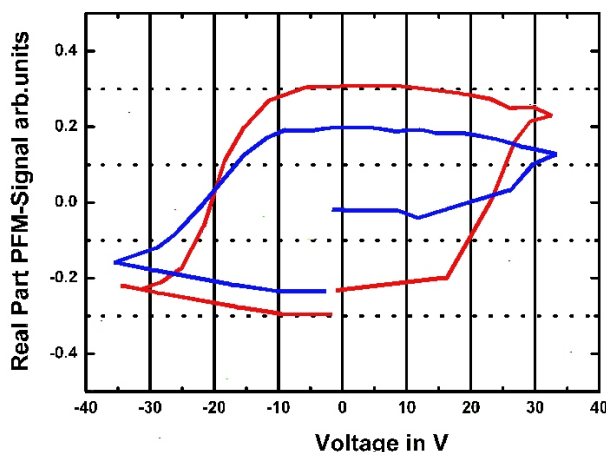


Figure 6.15: Ferroelectric hysteresis loop of an individual 400 nm P(VDF-co-TrFE) nanotube. The blue and red curves represent the hysteresis loops before and after poling, respectively.

Local (remnant) piezoelectric hysteresis loops were measured by PFM after the poling voltage was switched back to zero. Figure 6.15 shows the hysteresis loops obtained on an individual P(VDF-co-TrFE) nanotube with a diameter of 400 nm before (in blue) and after (in red) poling, respectively. The piezoelectric signals are associated with local polarization switching and ferroelectric properties of the copolymer nanotubes. Both curves show a ferroelectric switching at a coercive voltage of about 15 V, which is on the same order of magnitude as in the case of copolymer thin film [157]. As expected, poling process increases the local piezoelectric response. The effective remnant piezoelectric coefficient after poling has an increase of about 65%. As piezoelectric polymers belong to the category of lossy piezoelectric materials, the fact

that the hysteresis loops are not closed is related to relaxation phenomenon, which is reduced to 30% in poled state compared to the pristine state.

6.4 Summary of the chapter

In this chapter, ferroelectric copolymer nanotubes made from P(VDF-co-TrFE) with different diameters were studied with an emphasis on the main structural features and properties which are related to the ferroelectric behavior of these nano-objects. The studies included morphology characterizations, thermal investigations, crystallinity studies and most important, the ferroelectric properties, which unveiled the domain structures of the copolymer nanotubes. According to the results, we conclude that the pore walls, which act as a strong confinement, yield specific textures of P(VDF-co-TrFE). Thus, a structural model was proposed for the growth of P(VDF-co-TrFE) crystallites. We expect that these functional organic 1D nano-objects will find their way into the already existing operating systems of ferroelectric ceramics and will lead to more flexibility, easier operation and lower cost.

7. Building blocks III: metallic micro- and nano(shell) tubes and multi-layer tubes

After the core elements, 1D functional ferroelectric nano- and micro-elements have been realized in Chapter 5 and Chapter 6, it is still necessary to apply electrodes on them at appropriate places. We propose that it could be realized via metallic nanoshell tubes. By consecutively wetting the pore walls of porous materials by electrode metal, ferroelectric material and again with electrode metal, the ferroelectric nano- and micro-tubes obtained are coated by metal layers at both of the inner and the outer walls. In this chapter, the fabrication of metallic nano(shell) tubes via organometallic precursor with various parameters as well as their properties will be described. Large-scale production of metallic nanoshell tubes either aligned within a template or released without support as a powder is carried out. The important features for these metallic nano- and microtubes lie in their potential to be used not only as electrodes for integrated functional devices but also more generally as catalyst and sensors as a result of their properties such as plasmon resonances.

7.1 Pt nano(shell) tubes via organometallic composite precursors

Sun *et al.* [46] recently reported on an elegant method to prepare Pt nanotubes involving the reductive deposition of a Pt salt on a silver nanowire along with the oxidation of silver. However, one obtains dispersed nanotubes that are difficult to align or to attach to a support, or to be combined with ferroelectric layers.

Polymeric liquids can be loaded with considerable proportions of low molar mass compounds. Metal tubes may be accessible via composite tubes containing a metal precursor. For example, palladium nanotubes with adjustable porosity [158] were prepared using polylactide (PLA)/palladium(II) acetate solutions that were originally introduced by Hou *et al.* to fabricate PLA/palladium composite nanofibers by electrospinning [159]. PLA completely degrades at elevated temperatures, and it can be conveniently removed by pyrolysis. Template wetting with solutions containing PLA and a low molar mass compound acting as a metal source should be a promising and general route towards metallic tubes. First, the solutions are dropped on the template at ambient conditions. Subsequent annealing transforms the precursor into the respective metal, and PLA degrades completely. As a result, metal tubes remain within the template pores.

As Pt source, we used 99.99 % 2,4-pentanedione platinum(II) ((Pt(C₅H₇O₂)₂, Pt(acac)₂). It was mixed with either poly(*D,L*-lactide) (PDLLA) or polystyrene (PS) from Sigma-Aldrich in a ratio of 3:1, and dissolved in CH₂Cl₂ or CHCl₃. The light yellow solutions were then dropped onto a macroporous silicon or porous alumina templates at ambient conditions. After the solvent had been evaporated, the solidified polymer/metal precursor mixture formed a thin

film covering both the pore walls and the surface of the template. The residual material on the template surface was carefully removed with a sharp scalpel. SEM investigations confirmed that the pore openings were uncovered. $\text{Pt}(\text{acac})_2$ degrades at 200°C along with a reduction of Pt(II) to Pt. Ostwald ripening results in the growth of Pt crystallites within the liquid polymeric matrix. Eventually, the crystallites sinter and form a tubular structure that is stable even after the removal of the PDLA or PS and the template. The ripening process is very important for the formation of tubular structures as only discrete particles could be found without this ripening (c.f. section 2.5 and section 2.6.3).

7.1.1 Crystallinity of Pt nano(shell) tubes

To investigate the formation of the Pt crystallites, wetted macroporous Si samples (pore diameter $D_p = 1\ \mu\text{m}$) were first annealed at 200°C for 24 h, then at 350°C for 1 h and finally at 600°C for 1 h. All the annealing steps were realized in air. $\Theta/2\Theta$ scans (figure 7.1) were performed in the reflection mode with a 2Θ resolution of 0.05° and an integration time of 1 s subsequently to each annealing step. The sample was placed in the diffractometer in such a way that the aligned nanoshell tubes within the template were oriented parallel to the plane defined by the incident and the reflected X-ray beams. For all the XRD diffractograms shown in figure 7.1, the reflections of platinum were assigned by using the JCPDS card No.04-0802. The first annealing step at 200°C led to the formation of polycrystalline platinum within the PDLA matrix. The (111) and the (200) reflections of face-centered cubic Pt occurred at $2\Theta = 39.88^\circ$ and $2\Theta = 46.38^\circ$, respectively. Assuming a spherical shape of the crystallites, we estimated their size (d) from the full widths at half maximum (FWHM) of both reflections using the Debye-Scherrer equation [160]: $d = 0.89\ \lambda / \text{FWHM} \cos \Theta$, where λ is the wavelength of $\text{CuK}\alpha$ radiation ($= 0.1541\ \text{nm}$) and Θ is the diffraction angle.

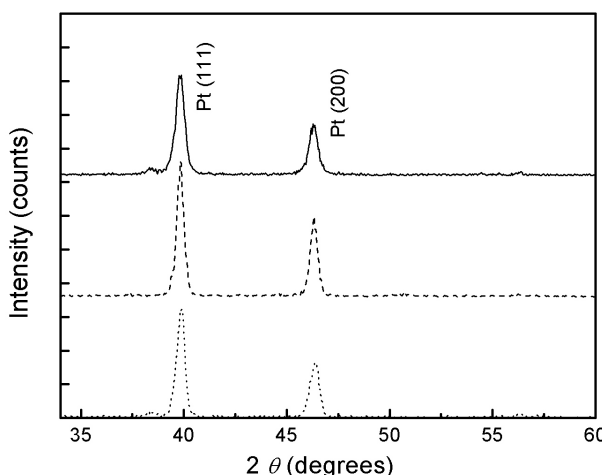


Figure 7.1: XRD patterns of macroporous silicon containing Pt nanoshell tubes that were annealed at 200°C for 24 h, then at 350°C for 1 h and finally at 600°C for 1 h, measured at room temperature. The solid line denotes the diffractogram obtained after the first annealing step at 200°C . The dashed line corresponds to the diffractogram obtained after the second annealing step at 350°C , and the dotted line to the diffractogram obtained after a third annealing step at 600°C . One scale division on the intensity axis corresponds to 200 counts.

The calculated diameter of the particles was of the order of 8 nm (table 7.1). The subsequent annealing at 350°C for one hour removed the PDLA completely. Moreover, the crystallite size increased significantly to 10 nm. For both diffractograms measured after annealing at 200°C and 350°C , the values of the crystallite sizes estimated from the two evaluated reflections coincide well. Contrary to our expectations, further annealing at 600°C led to a decrease of crystallite size. We obtained values of 9.2 nm by evaluating the (111) reflection and 8 nm by evaluating the (200) reflection. We speculate that mechanical stress occurring during cooling to room temperature could have disturbed the crystal structure.

	Annealed at 200 °C	Annealed at 350 °C	Annealed at 600 °C
Plane (111)	8.1 nm	10 nm	9.2 nm
Plane (200)	7.7 nm	10 nm	8 nm

Table 7.1: Crystal sizes of Pt nanoparticles within the walls of Pt nanoshell tubes obtained after the successive annealing steps estimated by using the Debye-Scherrer method.

7.1.2 Morphology characterization of Pt nano(shell) tubes

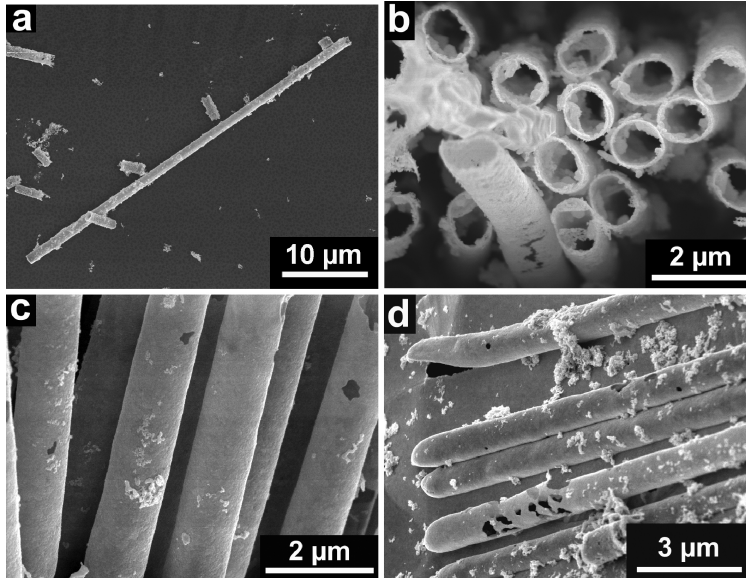


Figure 7.2: SEM images of Pt nanoshell tubes prepared by annealing at 200 °C for 24h and at 350 °C for 1 h. (a) An unsupported Pt nanoshell tube on a silicon substrate; (b) top view of the openings of Pt nanoshell tubes emanating from a partially etched silicon template. The sample is contaminated with KOH; (c) middle section of some aligned Pt nanoshell tubes; (d) tips of Pt nanoshell tube that are replicas of the blind ends of the pores.

Figure 7.2 shows SEM micrographs of Pt nanoshell tubes lying on silicon substrates prepared by annealing the Pt/PDLLA composite tubes at 200 °C for 24 h and 350 °C for 1 h. Subsequently, the silicon template was etched either partially or completely. An individual Pt nanoshell tube with an aspect ratio of 50 is depicted in figure 7.2a. The openings of Pt nanoshell tubes that are partially embedded in the macroporous silicon matrix are shown in figure 7.2b. Using the image analysis program *DIPS* we estimated the thickness of the tube walls to approximately 40 nm. Figure 7.2c shows the middle sections of some aligned Pt nanoshell tubes. Figure 7.2d represents their capped tips, which are exact replicas of the blind ends of the template pores. The Pt nanoshell tubes have smooth walls showing only few defects.

The cross-sections of Pt nanoshell tubes embedded in epoxy resin can be investigated by TEM. A TEM bright field micrograph of a cross-section of a Pt nanoshell tube is shown in figure 7.3a. Figure 7.3b displays the tube wall at a higher magnification. It is obvious that the wall consists of sintered Pt nanoparticles. However, the wall thickness cannot be estimated from figure 7.3b since the shape of the nanoshell tube was considerably deformed during preparation. Moreover, for a precise measurement of the thickness, the angle between the plane of the section and the long axis of the tube had to be adjusted to 90°. It is obvious that the Pt tubes having diameters in the micron range have a nanostructured wall. Consequently, they represent a hierarchical system, combining features in the 10 nm and the micrometer range.

Figure 7.3c shows another TEM micrograph of a Pt nanoshell tube at low magnification. Figure 7.3d depicts a part of the wall at a higher magnification. It is composed of nanoparticles with a size of the order of 8 ~ 10 nm, which is in line with the data obtained by evaluating the XRD measurements with the Debye-Scherrer method. Image analysis using the program *scion image 4.0.2* revealed that no short-range-order exists. This indicates that a mechanism

based on nucleation led to the formation of the tube walls. The corresponding selected-area electron diffraction on the area shown in figure 7.3d yielded multi-ring patterns, confirming the polycrystalline nature of the nanoshell tubes.

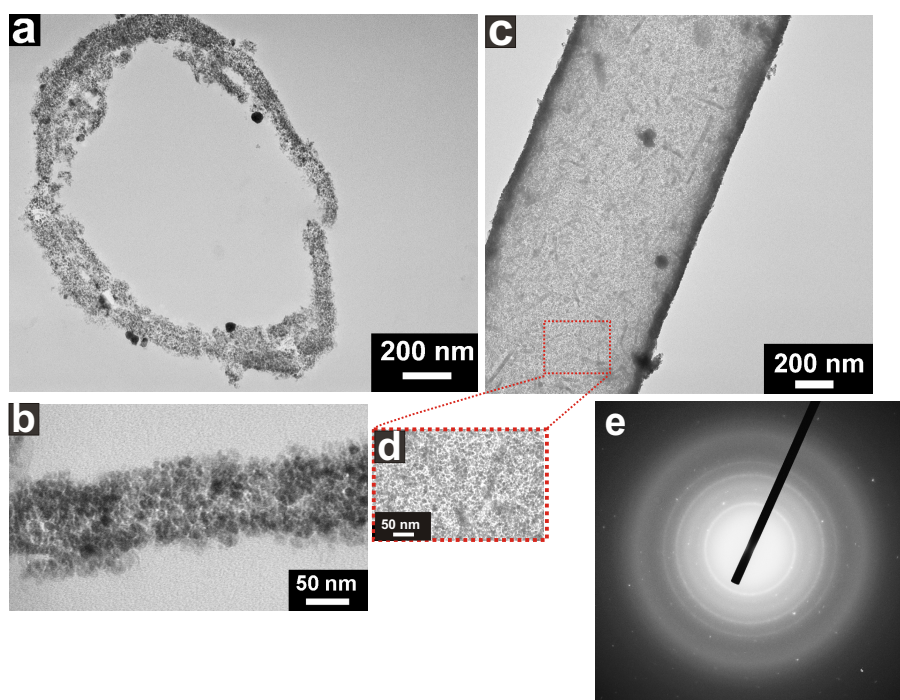


Figure 7.3: TEM micrographs of Pt nanoshell tubes. (a) TEM micrograph of an ultra-thin slice showing the cross-section of a Pt nanoshell tube embedded in epoxy resin. (b) Detail of the tube wall at higher magnification. (c) Snapshot of a Pt nanoshell tube wall at low magnification. (d) A part of the tube wall shown in (c) at a higher magnification. (e) Selected-area electron diffraction (SAED) pattern on the area shown in (d).

7.1.3 Metal/organic composite tubes

In order to evaluate if Pt/polymer tubes are accessible, which would be the first step toward functional multi-layer systems such as Pt/P(VDF-co-TrFE)/Pt tubes, polystyrene with a density of 1.05 g/cm^3 was used as the first experiment for feasibility. It is wetted as the second reinforcing wetting layer. The condition required for the first method is that the metal should have a surface energy that is sufficiently high to wet templates having metal-coated pore walls once again. This condition is commonly fulfilled.

We dropped a solution of polystyrene dissolved in chloroform on a macroporous silicon template containing Pt nanoshell tubes within its pores. The sample was then annealed for 1 h at 100°C to accomplish the formation of a defect-free PS wetting layer on the inner surface of the Pt nanoshell tubes. As a result, we obtained core/shell tubes consisting of a Pt shell and a PS core (figure 7.4). Sonification resulted in the partial removal of the Pt shell, so that the PS core was uncovered (the upper tube in figure 7.4a).

Energy dispersive X-Ray microanalysis (EDX) was used to verify the presence of Pt and PS in both methods. For example, figure 7.4b describes the EDX spectrum of the composite Pt/PS tubes shown in figure 7.4. The $K\alpha$ carbon peak at 0.3 keV indicating the presence of PS and three Pt peaks ($2.1 \text{ keV: } M\alpha$, $M\beta$: $9.4 \text{ keV: } L\alpha$; $11.2 \text{ keV: } L\beta$) were detected. The

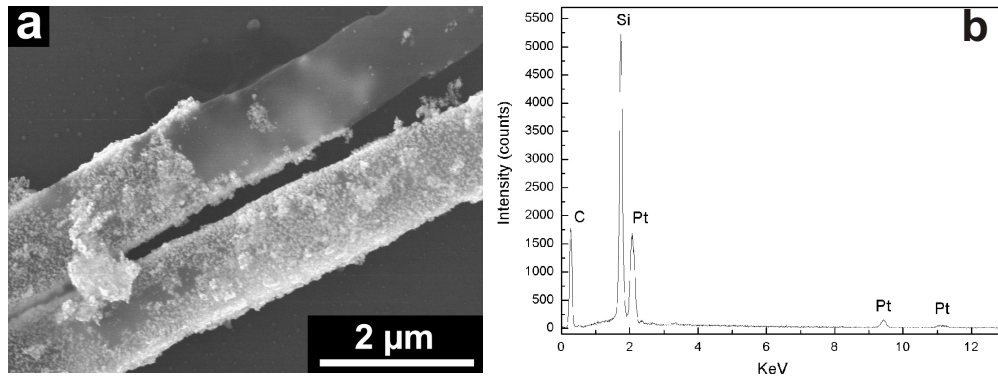


Figure 7.4: (a) SEM image of core/shell nanoshell tubes composed of an inner PS core and an outer Pt shell, obtained by successive wetting steps. Top right, the PS core is partially uncovered. (b) Energy dispersive X-ray spectrum of PS/Pt core/Shell nanotubes obtained by method I.

most intensive silicon peak (1.7 keV: $K\alpha$, $K\beta$) originates from the silicon wafer on which the core/shell tubes were placed.

7.2 Multi-layer nano(shell) tubes

After the realization of all the nano- and micro-elements, including functional ferroelectric tubes as core objects and metallic tubes as electrodes, we propose the following primary complex structure which could serve as a more intricate building blocks for functional device: multi-layer nanoshell tubes with tube walls consisting of metal/oxide/metal layers consecutively.

Preparation of tri-layer metal/oxides/metal nanoshell tubes

In the template-wetting method, if the obtained tubes within the template pores resulting from a first wetting step consist of an inorganic material having a sufficiently high surface energy, further wetting steps may be performed. Complex multi-layer architectures are thus accessible. To prepare successfully the multi-layer structures, we consecutively applied procedures described in the sections 5.2 and 7.1. Tubes having walls that consist of an oxide intermediate layer sandwiched between two platinum layers have been prepared.

To prepare the first Pt layer, macroporous silicon with a D_p -value $1 \mu m$) was used and subsequently processed by the protocol described in section 7.1. Subsequently, we wetted the Pt/Si hybrid structure with the commercially available polymeric PZT precursor (PZT 9906, *Chemat Technology*) and the protocol depicted in section 5.2 was employed to get a second layer of PZT. Finally, the inner Pt layer was added in the same manner as described above.

A SEM image of such a Pt/BTO/Pt nanoshell tube lying on a silicon wafer, having a radius of $1 \mu m$ and a length of $100 \mu m$ is presented in figure 7.5. The outer Pt layer is smooth and virtually defect-free. Figure 7.6 shows a free-standing array of Pt/PZT/Pt nanoshell tubes both as top view (figure 7.6a) and as side view (figure 7.6b). Such free-standing hybrid structures are promising to be used as building blocks in the MEMS.

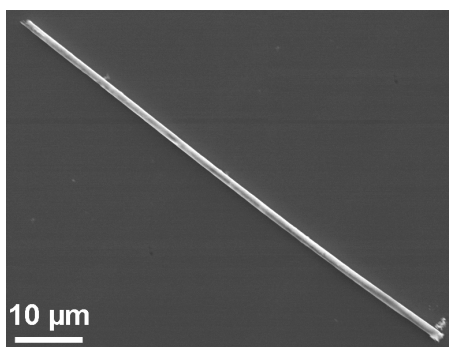


Figure 7.5: SEM image of a released Pt/BTO/Pt nanoshell tube lying on a silicon wafer

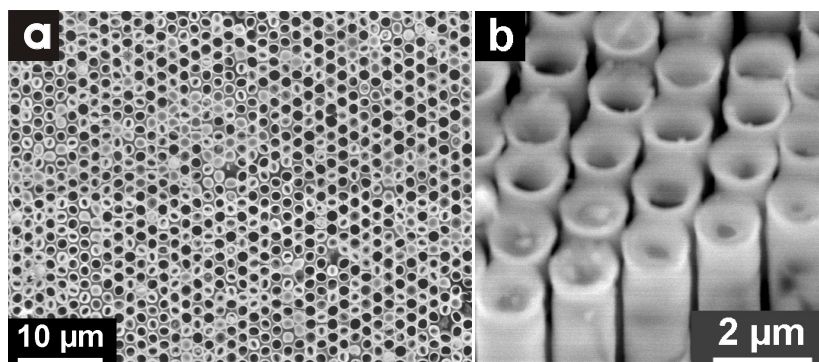


Figure 7.6: SEM images of ordered arrays of partly released Pt/PZT/Pt nanoshell tubes obtained by selective, partial etching of the porous silicon template: (a) top view; (b) side vies.

Characterization of tri-layer nanoshell tubes

We performed XRD investigations on the hybrid Pt/PZT/Pt nanoshell tubes located within the template pores in the reflection mode as described in the section 4.2.2. As denoted in figure 7.7, the reflections of platinum and PZT were assigned using the JCPDS cards *No.*04 – 0802 and *No.*33 – 1784, respectively. The (111) and (200) reflections of face-centered cubic (fcc) Pt at $2\Theta = 39.8^\circ$ and $2\Theta = 44.2^\circ$ as well as the (100), (101), and (110) reflections of PZT at 2Θ values of 21.7° , 29.8° , and 30.9° were detected. As Pb is a highly diffusive material, it might form crystals of oxides during the high temperature annealing process. According to the corresponding JCPDS files, the rather broad, weak reflections at $2\Theta = 33^\circ$, 34.9° and 38.2° (marked *) can be assigned to a mix of different lead oxides (PbO , $\text{Pb}_{12}\text{O}_{19}$, $\text{PbO}_{1.57}$, PbO_{32}). The rather sharp, strong peak at $2\Theta = 6.3^\circ$ (marked \times) most probably corresponds to a single phase. For this phase, three lead-oxide options exist, viz. Pb_2O ($2\Theta = 36.356^\circ$), PbO_2 ($2\Theta = 36.2^\circ$), and $\beta\text{-PbO}_2$ ($2\Theta = 36.5^\circ$). The rather high background between $2\Theta = 23^\circ$ and 35° most probably points to the presence of an amorphous phase.

A cross-sectional bright field TEM image of an ultra-thin section of a Pt/PZT/Pt nanoshell tube perpendicular to its long axis is shown in figure 7.8. Its circular shape has been distorted during the preparation. However, the inner and the outer Pt layers, which consist of crystallites that appear dark, are clearly discernible. The brighter region in-between corresponds to the intermediate PZT layer. The corresponding selected-area electron diffraction pattern encompassing the whole cross-section yielded multi-ring patterns (inset of figure 7.8), confirming the polycrystalline nature of both the Pt and PZT layers.

We investigated the spatial distribution of Pt, lead (Pb), zirconium (Zr) and titanium (Ti) within a tube wall by EDX attached to a TEM along a line in the radial direction, with respect to the long axis of the tube, as indicated by the white arrow shown in the inset of figure 7.9a. The Pt layers

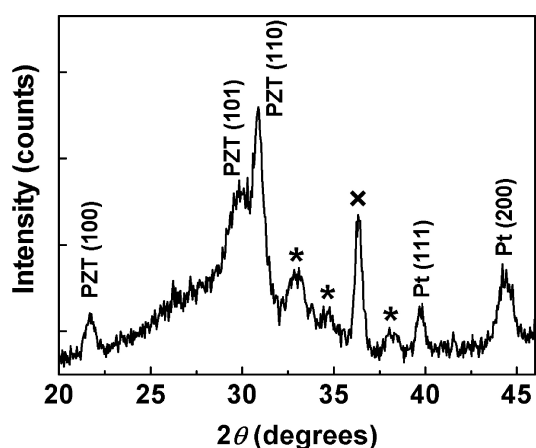


Figure 7.7: X-ray diffraction (XRD) pattern of macroporous silicon containing Pt/PZT/Pt nanoshell tubes. The reflections marked by *) and × can be assigned to a mix of different lead oxides. For details see text. One scale division on the intensity axis corresponds to 200 counts.

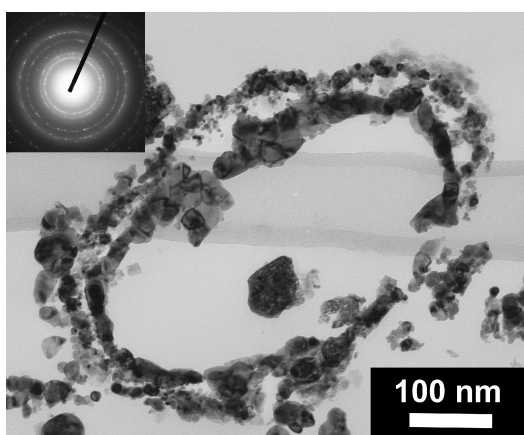


Figure 7.8: TEM micrograph of an ultra-thin slice showing the cross-section of a Pt/PZT/Pt nanoshell tube embedded in epoxy resin. The shape of the tube has been distorted during the preparation of the TEM specimen. The inset displays the corresponding selected-area electron diffraction (SAED) pattern.

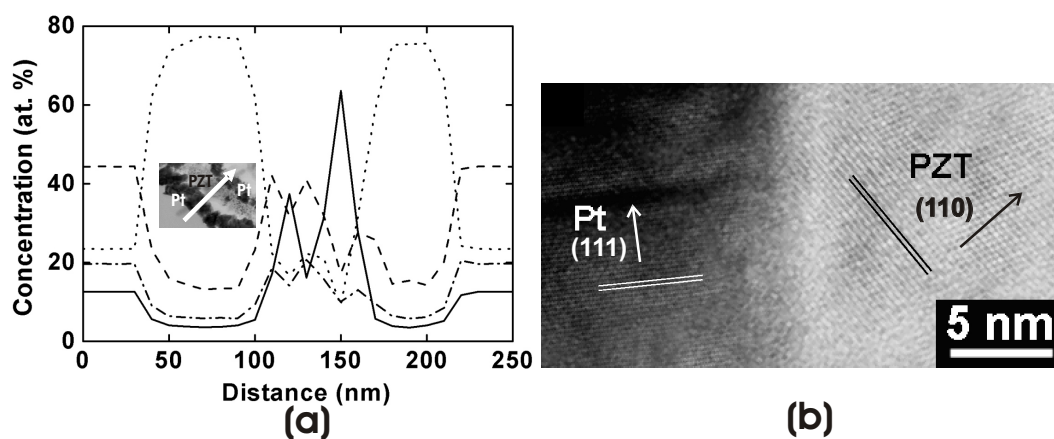


Figure 7.9: (a) Spatial distribution of Pt, Pb, Ti and Zr within the wall of a Pt/PZT/Pt tube, recorded by an EDX line scan along the path indicated by the arrow in the inset (solid line: Ti, dashed line: Zr, dotted line: Pt, and dashed-dotted line: Pb). (b) HRTEM micrograph of the interface between a Pt (dark area on the left) and a PZT layer (brighter area on the right). The crystallographic (111) and (110) directions of the Pt and PZT grains are indicated, respectively.

are discernible as darker stripes compared to the brighter intermediate PZT layer. By recording the intensity of the respective $K\alpha$ lines, the presence of each element was semi-quantitatively determined, as depicted in figure 7.9a. The outer regions exclusively consist of Pt, sandwiching an inner layer containing Pb, Zr and Ti, the metals contained in PZT. The overall thickness of the wall at this place amounts to approximately 150 nm. Note that the content of lead is lower than expected because of the aforementioned volatility of Pb during the high temperature annealing. There is, however, a sharp interface between the neighboring layers, suggesting that no substantial interdiffusion occurred. This is obvious from figure 7.9b, where the dark area on the left side corresponds to the Pt and the bright area on the right side to the PZT layer. The marked lattice fringes of the Pt crystallite correspond to the (111) lattice planes of fcc Pt, and those of the PZT grain to the (110) lattice planes of the perovskite phase. The crystallite sizes for Pt and PZT were estimated to be 15 nm and 10 nm, respectively.

Figure 7.10 shows an ultra-thin section of a Pt/PZT/Pt nanoshell tube along its long axis. It is also obvious that the Pt layers actually have a uniform thickness of about 30 nm whereas the PZT layer exhibits, however, pronounced thickness undulations. As already discussed in Chapter 5, such inhomogeneity in wall thickness can be ascribed to the occurrence of Rayleigh instabilities [76].

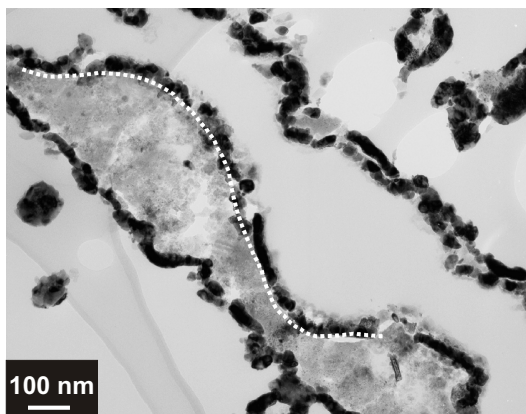


Figure 7.10: TEM micrograph of the cross-section along the tube axis of a trilayer Pt/PZT/Pt nanoshell tube. The profile of the PZT layer is designated by a white dotted curve.

7.3 Summary of the chapter

Fabrication of metallic (Pt) nanoshell tubes as the inner and outer electrodes for ferroelectric inorganic nanoshell tubes has been accomplished. Porous templates are wetted at ambient conditions with solutions containing PDLLA or PS as a sacrificial polymer and the metallic precursor $Pt(acac)_2$ and subsequent annealing steps yield Pt nanoshell tubes. By performing consecutive steps of wetting of porous templates, tri-layer tubes composed of Pt, ferroelectrics and Pt as tube walls are accessible. Either unsupported or free-standing tri-layer tubes are accessible by selectively removing the templates. The tube diameter is adjustable by using templates with respective pore diameters. Such structures should be of considerable interest as building blocks for more delicate functional devices such as a cantilever or mass storage devices. Approaches to overcome Rayleigh instabilities leading to uniform wall thickness have been suggested.

8. Conclusions and outlook

8.1 Conclusions

1D ferroelectric micro- and nanostructures can be building blocks for a multitude of functional device architectures. In this thesis, the properties of inorganic nano(shell) tubes consisting of PZT and BTO, as well as polymeric nanotubes consisting of copolymer P(VDF-co-TrFE), have been studied. These micro- and nano-objects were obtained by template-wetting method. The ability of polymer melts or solutions to wet the inner pore walls of a porous template, including ordered macroporous silicon and porous alumina, have been exploited.

First of all, the optical properties and wall morphologies of highly ordered porous alumina templates were investigated, both experimentally and theoretically. It was found that the dielectric constants in the pore walls of porous alumina are inhomogeneous, which results from a non-uniform anion concentration. A model concerning the distribution of the anions was proposed.

Based on the wetting phenomena of polymers or polymeric solutions on the inner pore walls of porous templates, two different types of ferroelectric nano(shell) tubes were obtained successfully, consisting of perovskite oxides (e.g., lead zirconate titanate and barium titanate oxide) and copolymer P(VDF-co-TrFE), respectively.

In case of inorganic ferroelectric tubes consisting of perovskite oxides, *X-ray diffraction* and *Transmission electron microscopy* investigation revealed polycrystalline nature. A ferroelectric switching behavior was demonstrated by *Piezoresponse force microscopy* on an individual PZT nano(shell) tube with a diameter of 700 nm. Snapshots of Rayleigh instabilities were observed during the formation of perovskite oxide nano(shell) tubes, which extend the knowledge on the mechanism underneath. It is also proposed that the Rayleigh instabilities might be suppressed by mixing the oligomeric precursor with high-molecular weight polymers.

In case of organic copolymer nanotubes consisting of ferroelectric P(VDF-co-TrFE), the ferroelectric/paraelectric phase transition as well as the melting behavior was investigated by *Differential scanning calorimetry* with different pore diameters D_p . By the evaluation of the melting endotherms of the paraelectric high-temperature phase, which are related to the crystallite size, the thickness of the tube wall was estimated to be around 30 nm. The existence of a cross-over of nanotubes and nanorods was also confirmed when the pore diameter is reduced below 60 nm. Moreover, the interpretation on the Curie temperatures where a ferroelectric/paraelectric phase transition takes place also shows a signature of this cross-over. By comparing the crystallite size for different D_p -values, it was concluded that a decrease in curvature facilitates the growth of the crystallites. By way of $\Theta/2\Theta$, especially Ψ scans, a pronounced crystalline texture was detected: the $\langle 110 \rangle$ direction of the ferroelectric pseudo-hexagonal phase is predominantly oriented parallel to the long axes of the nanotubes. The ferroelectric properties of a bundle of and individual P(VDF-co-TrFE) nanotubes were investigated by *Piezoresponse force microscopy*. Polings were realized for P(VDF-co-TrFE) nanotubes as segments in case of a bundle of 180 nm nanotubes as well as domains in case of individual 400 nm nanotubes. Information on the polarization domain walls and orientations after poling as well as the piezoelectric re-

sponse before and after poling were obtained. A pronounced enhancement in effective remnant piezoelectric coefficient as well as a reduction in relaxation phenomenon after the poling of P(VDF-co-TrFE) nanotubes was revealed. By relating the results obtained by *Piezoresponse force microscopy* and the diffractograms given by *X-ray diffraction*, a structural model for the growth of P(VDF-co-TrFE) crystallites within the confinement of pore walls was proposed. The results we get from the texture suggest that the structures are even more feasible for longitudinal poling as a result of the direction of the polar b -axis.

A possible mounting of electrodes at both the inner and outer walls of the ferroelectric tubes has been proposed. A prototype of tri-layer tubes with tube-walls composed of metal/ferroelectrics/metal consecutively has been shown. The realization of such tri-layer tubular structures opens up the possibility to control 3D movements of cantilevers based on ferroelectric nano(shell) tubes.

8.2 Outlook

In order to be integrated into existing functional devices to act as a component for the mass storage device, a better control on the quality of the ferroelectric nano- and micro-objects is needed. Especially the following tasks have to be tackled:

- Overcome the undulations of the profiles of pore walls caused by Rayleigh instabilities. As stated several times earlier in the thesis, Rayleigh instabilities occurred during the formation of perovskite oxide nano(shell) tubes while an oligomeric precursor was used. The resulting local variation in wall thickness will cause problems for electroded nanotubes. For example, when the metallic electrodes are attached to the inner and outer pore walls, the application of an external electric field can induce an inhomogeneous distribution of electric field across the ferroelectric tube walls. It is proposed that by mixing the oligomeric precursor with high-molecular weight polymers might suppress the occurrence of Rayleigh instabilities.
- Pole macroscopic arrays of P(VDF-co-TrFE) nanotubes in an external electric field during the crystallization. For applications, it is often required that the functional elements possess uniform structural features on a macroscopic scale. For ferroelectric P(VDF-co-TrFE) nanotubes, either in their released states or as ordered free-standing arrays, it is desired that their polarization could adopt a homogeneous distribution, i.e., either perpendicular or parallel to the tube walls. We propose that this can be done by the application of an external electric field in a specific direction during the crystallization of the P(VDF-co-TrFE) copolymer within the confinement of the porous templates.
- Connect electrodes properly to the specific places on the ferroelectric tubes. In order to realize applications such as a tubular cantilever which can be moved controllably in all the x , y , and z directions (similar to the more macroscopic scanner of an STM), electrodes need to be attached at specific places on the tubes in order to control the movement of bending in different directions as well as up/down movements. For example, as shown in figure 8.1a, in which a sub-micron piezoelectric cantilever is depicted, an inner electrode can be obtained by coating uniformly the inner tube walls while the outer electrodes are realized via four homogeneously distributed stripe electrodes. Presently, it is an unsolved problem on how strip-electrodes could be attached to millions of tubes in parallel.

Several applications based on piezoelectric nano(shell) tubes could be proposed [10]. First of all, a strongly miniaturized scanner tube can be fabricated from a single piezoelectric nanotube

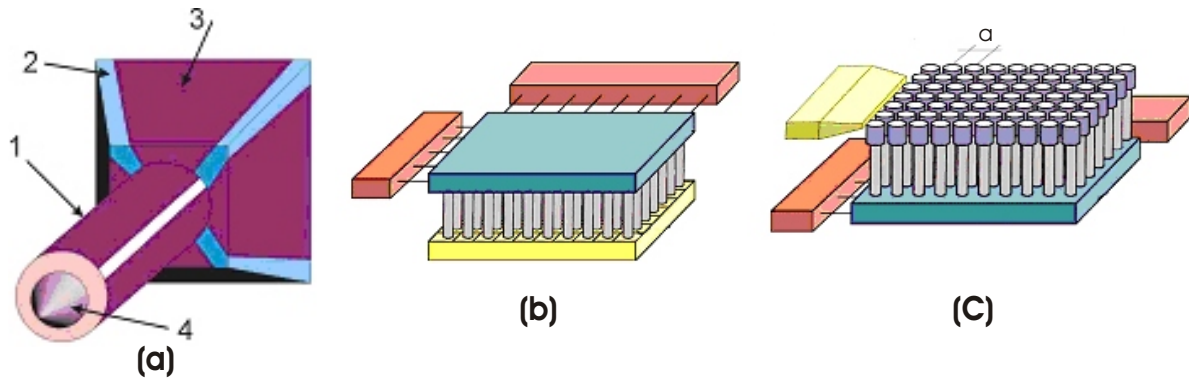


Figure 8.1: Envisioned devices based on piezoelectric nanoshell tubes. (a) Schematic of active sub-micron piezoelectric scanners. 1. piezoelectric tube, 2. electrodes, 3. substrate, 4. tip. (b) Mass storage devices. (c) Tunable photonic crystals.

(figure 8.1a) with properly attached metallic electrodes. Inner and outer electrodes in the same configuration as the classical piezoelectric scanner used in nowadays scanning probe microscopes will allow a 3D movement of the free end of the tube. As the tube walls are very thin, the deflection of the nanotube can be controlled precisely by small voltages applied to the electrodes. Moreover, such a scanner-tube could also act as a detector due to its interaction with the sample surface.

Ordered arrays of ferroelectric nanotubes also have large application potential in the field like mass storage devices (figure 8.1b) similar to IBM “Millipede” storage devices [161]. In such devices, all the micro-cantilevers (piezoelectric tubes) scan independently their individual area and write/read data in an associated section of the storage medium, which is called a bit array of a storage field. Compared to conventional mass storage devices the ferroelectric probe arrays permit a fully random read/write process with an increased access speed since the individual storage field is not read out in series, but in parallel.

Photonic bandgap (PBG) structures [90] may also be formed by highly ordered two-dimensional arrays of ferroelectric nanotubes (figure 8.1c). By applying an external electric field, each nanotube can be deflected in several ways, thus leading to periodicity and/or symmetry changes or introduction of well-defined defects in the arrays. All these shifts will allow the tuning of both the position and the width of the photonic bandgap .

Bibliography

- [1] E. Grochowski and R. F. Hoyt, "Future trends in hard disk drives," *IEEE Trans. Magn.*, vol. 32, p. 1850, 1996.
- [2] H. J. Mamin and D. Rugar, "Thermomechanical writing with an atomic force microscope tip," *Appl. Phys. Lett.*, vol. 61, p. 1003, 1992.
- [3] R. P. Ried, H. J. Mamin, B. D. Terris, L. S. Fan, and D. Rugar, "6-MHz 2-N/m piezoresistive atomic-force-microscope cantilevers with incisive tips," *J. Microelectromech. Syst.*, vol. 6, p. 294, 1997.
- [4] H. J. Mamin, B. D. Terris, L. S. Fan, S. Hoen, R. C. Barrett, and D. Rugar, "High-density data storage using proximal probe techniques," *IBM J. Res. Develop.*, vol. 39, p. 681, 1995.
- [5] H. J. Mamin, R. P. Ried, B. D. Terris, and D. Rugar, "High-density data storage based on the atomic force microscope," *Proc. IEEE*, vol. 87, p. 1041, 1999.
- [6] P. Vettiger, J. Brugger, M. Despont, U. Drechsler, U. Dürig, W. Häberle, M. Lutwyche, H. Rothuizen, R. Stutz, R. Widmer, and G. Binnig, "Ultrahigh density, high-data-rate NEMS-based AFM data storage system," *J. Microelectron. Eng.*, vol. 46, p. 111, 1999.
- [7] W. G. Cady, "Piezoelectricity," *Dover Publications, Inc.*, 76th edition, p. 1063, 1964. New York.
- [8] K. Aizu, "Second-order ferroic state shifts," *J. Phys. Soc. Japan*, vol. 34, p. 121, 1973.
- [9] M. Abplanalp, "Piezoresponse scanning force microscopy of ferroelectric domains," *PhD thesis*, 2001. Swiss Federal Institute of Technology.
- [10] M. Alexe, Y. Luo, I. Szafraniak, R. B. Wehrspohn, and M. Steinhart, "A method of operating and manufacturing a nanotube based cantilever arm, and a storage device and a photonic crystal based on an array of nanotube based cantilever arms," *European Patent Application*, no. 03000969.0/2002, 2002.
- [11] J. Jorritsma, M. A. M. Gijs, J. M. Kerkhof, and J. G. H. Stenen, "General technique for fabricating large arrays of nanowires," *Nanotechnology*, vol. 7, p. 263, 1996.
- [12] E. Olson, G. C. Spalding, A. M. Goldman, and M. J. Rooks, "New method for fabricating ultra-narrow metallic wires," *Appl. Phys. Lett.*, vol. 65, p. 2740, 1994.
- [13] H. Ringsdorf, B. Schlarb, and J. Venzmer, "Molecular architecture and function of polymeric oriented systems - models for the study of organization, surface recognition, and dynamics of biomembranes," *Angew. Chem. Int. Ed. Engl.*, vol. 27, p. 113, 1988.
- [14] S. O. Obare, N. R. Jana, and C. J. Murphy, "Preparation of polystyrene- and silica-coated gold nanorods and their use as templates for the synthesis of hollow nanotubes," *Nano Lett.*, vol. 1, p. 601, 2001.
- [15] J. C. Hulteen and C. R. Martin, "A general template-based method for the preparation of nanomaterials," *J. Mater. Chem.*, vol. 7, p. 1075, 1997.

- [16] C. R. Martin, "Template synthesis of electronically conductive polymer nanostructures," *Acc. Chem. Res.*, vol. 28, p. 61, 1995.
- [17] C. R. Martin, "Nanomaterials: a membrane-based synthetic approach," *Science*, vol. 266, p. 1961, 1994.
- [18] C. A. Huber, T. E. Huber, M. Sadiqi, J. A. Lubin, S. Manalis, and C. B. Prater, "Nanowire array composites," *Science*, vol. 263, p. 800, 1994.
- [19] X. Zhang, L. Zhang, G. Meng, G. Li, N. Jin-Phillipp, and F. Phillipp, "Synthesis of ordered single crystal silicon nanowire arrays," *Adv. Mater.*, vol. 13, p. 1238, 2001.
- [20] M. Zheng, L. Zhang, X. Zhang, J. Zhang, and G. Li, "Fabrication and optical absorption of ordered indium oxide nanowire arrays embedded in anodic alumina membranes," *Chem. Phys. Lett.*, vol. 334, p. 298, 2001.
- [21] S. A. Sapp, D. T. Mitchell, and C. R. Martin, "Using template-synthesized micro- and nanowires as building blocks for self-assembly of supramolecular architectures," *Chem. Mater.*, vol. 11, p. 1183, 1999.
- [22] C. G. Wu and T. Bein, "Conducting polyaniline filaments in a mesoporous channel host," *Science*, vol. 264, p. 1757, 1994.
- [23] J. F. Scott and C. A. P. de Araujo, "Ferroelectric memories," *Science*, vol. 246, p. 1400, 1989.
- [24] J. J. Urban, W. S. Yun, Q. Gu, and H. Park, "Synthesis of single-crystalline perovskite nanorods composed of barium titanate and strontium titanate," *J. Am. Chem. Soc.*, vol. 124, p. 1186, 2002.
- [25] W. S. Yun, J. J. Urban, Q. Gu, and H. Park, "Ferroelectric properties of individual barium titanate nanowires investigated by scanned probe microscopy," *Nano Lett.*, vol. 2, p. 447, 2002.
- [26] G. R. Fox, "Lead-zirconate-titanate micro-tubes," *J. Mater. Sci. Lett.*, vol. 14, p. 1496, 1995.
- [27] H. Kawai, "Piezoelectricity of poly(vinylidene fluoride)," *Japan J. Appl. Phys.*, vol. 8, p. 975, 1969.
- [28] T. Yagi, M. Tatemoto, and J. I. Sako, "Transition behavior and dielectric properties in trifluoroethylene and vinylidene fluoride copolymers," *Polym. J.*, vol. 12, p. 209, 1980.
- [29] Y. Higashihata, J. I. Sako, and T. Yagi, "Piezoelectricity of vinylidene fluoride - trifluoroethylene copolymers," *Ferroelectrics*, vol. 32, p. 85, 1981.
- [30] T. Furukawa, G. E. Johnson, H. E. Bair, Y. Tajitsu, A. Chiba, and E. Fukada, "Ferroelectric phase-transition in a copolymer of vinylidene fluoride and trifluoroethylene," *Ferroelectrics*, vol. 32, p. 61, 1981.
- [31] T. Yamada, T. Ueda, and T. Kitayama, "Ferroelectric-to-paraelectric phase-transition of vinylidene fluoride - trifluoroethylene copolymer," *J. Appl. Phys.*, vol. 52, p. 948, 1981.
- [32] J. F. Legrand, J. Lajzerowicz, B. Berge, P. Delzenne, F. Macchi, C. Bourgaux-Leonard, A. Wicker, and J. K. Kruger, "Ferroelectricity in VF₂-based copolymers," *Ferroelectrics*, vol. 78, p. 151, 1988.
- [33] Y. Murata and N. Koizumi, "Ferroelectric behaviour in vinylidene fluoride-tetrafluoroethylene copolymers," *Ferroelectrics*, vol. 92, p. 47, 1989.

- [34] T. Tashiro, K. Takano, M. Kobayashi, Y. Chatani, and H. Tadokoro, "Structural study on ferroelectric phase-transition of vinylidene fluoride-trifluoroethylene random copolymers," *Polymer*, vol. 22, p. 1312, 1981.
- [35] T. Tajitsu, A. Chiba, T. Furukawa, M. Date, and E. Fukoda, "Crystalline phase-transition in the copolymer of vinylidene fluoride and trifluoroethylene," *Appl. Phys. Lett.*, vol. 36, p. 286, 1980.
- [36] H. Yamazaki, J. Ohwaki, T. Yamada, and T. Kitayama, "Temperature-dependence of the pyroelectric response of vinylidene fluoride trifluoroethylene copolymer and the effect of its poling conditions," *Appl. Phys. Lett.*, vol. 39, p. 772, 1981.
- [37] R. Betz, "The advantages of bioriented piezoelectric film," *Ferroelectrics*, vol. 75, p. 397, 1987.
- [38] J. M. Vignolle, E. Chambost, and F. Micheron, "Simulation of matrix addressing in thin P(VDF-TrFE) 70/30 film for neural network application," *Ferroelectrics*, vol. 93, p. 5, 1989.
- [39] M. U. Smith and A. A. Shanlov, "Modified lead-titanate polymer composites for hydrophone applications," *Ferroelectrics*, vol. 76, p. 215, 1988.
- [40] M. Steinhart, S. Senz, R. B. Wehrspohn, and U. Gösele, "Curvature-directed crystallization of poly(vinylidene difluoride) in nanotube walls," *Macromolecules*, vol. 36, p. 3646, 2003.
- [41] S. J. Oldenburg, G. D. Hale, J. B. Jackson, and N. J. Halas, "Light scattering from dipole and quadrupole nanoshell antennas," *Appl. Phys. Lett.*, vol. 75, p. 1063, 1999.
- [42] S. W. Kim, M. Kim, W. Y. Lee, and T. Hyeon, "Fabrication of hollow palladium spheres and their successful application to the recyclable heterogeneous catalyst for Suzuki coupling reactions," *J. Am. Chem. Soc.*, vol. 124, p. 7642, 2002.
- [43] T. S. Ahmadi, Z. L. Wang, T. C. Green, A. Henglein, and M. A. El-Sayed, "Shape-controlled synthesis of colloidal platinum nanoparticles," *Science*, vol. 272, p. 1924, 1996.
- [44] J. D. Aiken and R. G. Finke, "A review of modern transition-metal nanoclusters: Their synthesis, characterization, and applications in catalysis," *J. Mol. Catal. A - Chem.*, vol. 145, p. 1, 1999.
- [45] H. Bönemann and R. M. Richards, "Nanoscale metal particles - synthetic methods and potential applications," *Eur. J. Inorg. Chem.*, p. 2455, 2001.
- [46] Y. G. Sun, B. T. Mayers, and Y. N. Xia, "Template-engaged replacement reaction: A one-step approach to the large-scale synthesis of metal nanostructures with hollow interiors," *Nano Lett.*, vol. 2, p. 481, 2002.
- [47] Y. G. Sun, B. T. Mayers, and Y. N. Xia, "Metal nanostructures with hollow interiors," *Adv. Mater.*, vol. 15, p. 641, 2003.
- [48] C. R. Sides, N. Li, C. J. Patrissi, B. Scrosati, and C. R. Martin, "Nanoscale materials for lithium-ion batteries," *MRS Bull.*, vol. 27, p. 604, 2002.
- [49] T. M. Whitney, T. S. Jiang, P. C. Searson, and C. L. Chien, "Fabrication and magnetic properties of arrays of metallic nanowires," *Science*, vol. 261, p. 1316, 1993.
- [50] Y. Zhang and H. Dai, "Formation of metal nanowires on suspended single-walled carbon nanotubes," *Chem. Mater.*, vol. 77, p. 3015, 2000.

- [51] B. H. Hong, S. C. Bac, C. W. Lee, S. Jeong, and K. S. Kim, "Ultrathin single-crystalline silver nanowire arrays formed in an ambient solution phase," *Science*, vol. 294, p. 348, 2001.
- [52] J. A. Song, Y. Wu, B. Messer, H. Kind, and P. Yang, "Metal nanowire formation using $\text{Mo}^3\text{Se}^{3-}$ as reducing and sacrificing templates," *J. Am. Chem. Soc.*, vol. 123, p. 10397, 2001.
- [53] M. P. Zach, K. H. Ng, and R. M. Penner, "Molybdenum nanowires by electrodeposition," *Science*, vol. 290, p. 2120, 2000.
- [54] F. J. Himpsel, T. Jung, A. Kirakosian, J. L. Lin, D. Y. Petrovykh, H. Rauscher, and J. Viernow, "Nanowires by step decoration," *MRS Bull.*, vol. 24, p. 20, 1999.
- [55] S. Moring, A. Lachenwitzer, O. M. Maagnussen, and R. J. Behm, "Potential-controlled step flow to 3d step decoration transition: Ni electrodeposition on Ag(111)," *Phys. Rev. Lett.*, vol. 83, p. 5066, 1999.
- [56] J. S. Rowlinson and B. Widom, "Molecular theory of capillarity," *Clarendon Press*, 1984.
- [57] P. G. de Gennes, "Wetting: Statics and dynamics," *Rev. Mod. Phys.*, vol. 57, p. 827, 1985.
- [58] L. H. Tanner, "Spreading of silicone oil drops on horizontal surfaces," *J. Phys. D*, vol. 12, p. 1473, 1979.
- [59] J. Lopez, M. C. A., and E. Ruckenstein, "Spreading kinetics of liquid-drops on solids," *J. Colloid. Interface Sci*, vol. 56, p. 460, 1976.
- [60] H. W. Fox, E. F. Hare, and W. A. Zisman, "Wetting properties of organic liquids on high energy surfaces," *J. Phys. Chem.*, vol. 59, p. 1097, 1955.
- [61] A. Marmur, "Equilibrium and spreading of liquids on solid-surfaces," *Adv. Colloid. Interf. Sci.*, vol. 19, p. 75, 1983.
- [62] J. F. Joanny and P. G. de Gennes, "Upward creep of a wetting fluid - a scaling analysis," *J. Phys.*, vol. 47, p. 121, 1986.
- [63] J. Israelachvili *Intermolecular and Surface Forces*, 1992. Academic Press.
- [64] J. Visser, "On Hamaker constants: A comparison between Hamaker constants and Lifshitz-van der Waals constants," *Adv. Colloid Interface Sci.*, vol. 3, p. 331, 1972.
- [65] F. Heslot, A. M. Cazabat, and P. Levinson, "Dynamics of wetting of tiny drops: Ellipsometric study of the late stages of spreading," *Phys. Rev. Lett.*, vol. 62, p. 1286, 1989.
- [66] E. Pérez, E. Schäffer, and U. Steiner, "Spreading dynamics of polydimethylsiloxane drops: Crossover from Laplace to van der Waals spreading," *J. Colloid. Interf. Sci.*, vol. 234, p. 178, 2001.
- [67] G. F. Teletzki *Thesis, University of Minnesota, unpublished*, 1983.
- [68] P. J. Flory, "Molecular configuration of polyelectrolytes," *J. Chem. Phys.*, vol. 21, p. 162, 1953.
- [69] D. Ausserré, A. M. Picard, and L. Léger, "Existence and role of the precursor film in the spreading of polymer liquids," *Phys. Rev. Lett.*, vol. 57, p. 2671, 1986.
- [70] L. Léger, M. Erman, A. M. Guinet-Picard, D. Ausserré, and C. Strazielle, "Precursor film profiles of spreading liquid drops," *Phys. Rev. Lett.*, vol. 60, p. 2390, 1988.

- [71] D. Glick, P. Thiansathaport, and R. Superfine, "In-situ imaging of polymer melt spreading with a high-temperature atomic force microscope," *Phys. Rev. Lett.*, vol. 60, p. 2390, 1988.
- [72] J. M. di Meglio, D. Quéré, and F. Brochard-Wyart, "Films mouillants dans les capillaires," *C. R. Acad. Sci. Paris, Série II*, vol. 309, p. 19, 1989.
- [73] M. G. Bernadiner, "A capillary microstructure of wetting front," *Transport Porous Med.*, vol. 30, p. 251, 1998.
- [74] J. Plateau, "Statique expérimentale et théorique des liquides soumis aux seules forces moléculaire," *Gauthier-Villars*, 1873. Paris.
- [75] F. Vollrath and D. J. Edmonds, "Modulation of the mechanical-properties of spider silk by coating with water," *Nature*, vol. 340, p. 305, 1989.
- [76] L. Rayleigh *Scientific Papers*, vol. 3, p. Cambridge University Press, 1902.
- [77] D. Quéré, J. M. di Meglio, and F. Brochard-Wyart, "Spreading of liquids on highly curved surfaces," *Science*, vol. 249, p. 1256, 1990.
- [78] J. W. Cahn, "Critical point wetting," *J. Chem. Phys.*, vol. 66, no. 8, p. 3667, 1977.
- [79] R. A. L. Jones, L. J. Norton, E. J. Kramer, F. S. Bates, and P. Wiltzius, "Surface-directed spinodal decomposition," *Phys. Rev. Lett.*, vol. 66, pp. 1326,3087, 1991.
- [80] J. W. Cahn, "Phase separation by spinodal decomposition in isotropic systems," *J. Chem. Phys.*, vol. 42, p. 93, 1965.
- [81] A. Budkowski, "Interfacial phenomena in thin polymer films: Phase coexistence and segregation," *Adv. Polym. Sci.*, vol. 148, p. 1, 1999.
- [82] K. Binder, "Phase transitions of polymer blends and block copolymer melts in thin films," *Adv. Polym. Sci.*, vol. 138, p. 1, 1999.
- [83] R. C. Ball and R. L. H. Essery, "Spinodal decomposition and pattern-formation near surfaces," *J. Phys. Condens. Mat.*, vol. 2, p. 10303, 1990.
- [84] G. Krausch, "Surface-induced self-assembly in thin polymer-films," *Mater. Sci. Eng.*, vol. R14, p. 1, 1995.
- [85] L. Sung, A. Karim, J. F. Douglas, and C. C. Han, "Dimensional crossover in the phase separation kinetics of thin polymer blend films," *Phys. Rev. Lett.*, vol. 76, p. 4368, 1986.
- [86] A. J. Liu, "Wetting transitions in a cylindrical pore," *Phys. Rev. Lett.*, vol. 65, p. 1897, 1990.
- [87] S. Wu, "Polymer interfaces and adhesion," *Marcel Dekker*, 1982. New York.
- [88] W. Barthlott and C. Neinhuis, "Purity of the sacred lotus, or escape from contamination in biological surfaces," *PLANTA*, vol. 202, p. 1, 1997.
- [89] R. B. Wehrspohn and J. Schilling, "Electrochemically prepared photonic crystals," *Mater. Res. Bull.*, vol. 8, p. 623, 2001.
- [90] J. D. Joannopoulos, R. D. Meade, and J. N. Winn, "Photonic crystals," *Princeton University Press*, 1995. New Jersey.
- [91] A. P. Li, F. Müller, A. Birner, K. Nielsch, and U. Gösele, "Hexagonal pore arrays with a 50-420 nm interpore distance formed by self-organization in anodic alumina," *J. Appl. Phys.*, vol. 84, p. 6023, 1998.

- [92] B. Vanderlinden, H. Terryn, and J. Vereecken, "Investigation of anodic aluminum-oxide layers by electrochemical impedance spectroscopy," *J. Appl. Electrochem.*, vol. 20, p. 798, 1990.
- [93] R. B. Wehrspohn, A. P. Li, K. Nielsch, F. Müller, W. Erfurth, and U. Gösele, "Highly ordered alumina films: Pore growth and applications," *Oxide Films in The Electrochemical Society Proceeding Series*, vol. PV 2000-4, p. 271, 2000. Pennington, NJ: Marcel Dekker.
- [94] J. Choi, "Fabrication of monodomain porous alumina using nanoimprint lithography and its applications," *Thesis, Martin-Luther-Universität Halle-Wittenberg*, 2004.
- [95] H. Masuda and K. Fukuda, "Ordered metal nanohole arrays made by a 2-step replication of honeycomb structures of anodic alumina," *Science*, vol. 268, p. 1466, 1995.
- [96] K. Nielsch, J. Choi, K. Schwirn, R. B. Wehrspohn, and U. Gösele, "Self-ordering regimes of porous alumina - the 10% porosity-rule," *Nano Lett.*, vol. 2, p. 677, 2002.
- [97] J. Choi, K. Nielsch, M. Reiche, R. B. Wehrspohn, and U. Gösele, "Fabrication of monodomain alumina pore arrays with an interpore distance smaller than the lattice constant of the imprint stamp," *J. Vac. Sci. Techn. B*, vol. 21, p. 763, 2003.
- [98] J. Choi, G. Sauer, K. Nielsch, R. B. Wehrspohn, and U. Gösele, "Hexagonally arranged monodisperse silver nanowires with adjustable diameter and high aspect ratio," *Chem. Mater.*, vol. 15, p. 776, 2003.
- [99] G. E. Thompson and G. C. Wood, "Porous anodic film formation on aluminum," *Nature*, vol. 290, p. 230, 1981.
- [100] J. Choi, Y. Luo, R. B. Wehrspohn, R. Hillebrand, J. Schilling, and U. Gösele, "Perfect two-dimensional porous alumina photonic crystals with duplex oxide layers," *J. Appl. Phys.*, vol. 94, p. 8, 2003.
- [101] F. L. Pedrotti and L. S. Pedrotti, "Introduction to optics," *Prentice Hall*, 1993. New Jersey.
- [102] K. Huber, "Pore volume of electrolytically produced protective coating on aluminum," *J. Coll. Sci.*, vol. 3, p. 197, 1948.
- [103] G. Hass, "On the preparation of hard oxide films with precisely controlled thickness on evaporated aluminum mirrors," *J. Opt. Soc. Am.*, vol. 39, p. 532, 1949.
- [104] S. Nakamura, M. Saito, L. F. Huang, M. Miyagi, and K. Wada, "Infrared optical-constants of anodic alumina films with micropore arrays," *Jpn. J. Appl. Phys.*, vol. 31, p. 3589, 1992.
- [105] A. L. Reynolds, "<http://ab-initio.mit.edu/mpb/>, translight package," University of Glasgow.
- [106] S. G. Johnson, "<http://ab-initio.mit.edu/mpb/>," MIT.
- [107] M. Woldeyohannes and S. John, "Coherent control of spontaneous emission near a photonic band edge," *J. Opt. B - Quantum S. O.*, vol. 5, p. R43, 2003.
- [108] H. Masuda, M. Ohya, K. Nishio, H. Asoh, M. Nakao, M. Nohtomi, A. Yokoo, and T. Tamamura, "Photonic band gap in anodic porous alumina with extremely high aspect ratio formed in phosphoric acid solution," *Jpn. J. Appl. Phys. 2*, vol. 39, p. L1039, 2000.
- [109] D. R. Lide, "CRC handbook of chemistry and physics," vol. 76th edition, p. 841, 1992.

- [110] Y. Fukuda, "Role of oxalate ion in formation of oxide film of aluminum in oxalic-acid electrolyte," *Nippon Kagaku Kaishi*, vol. 10, p. 1868, 1974.
- [111] Y. Fukuda, "Effect of pH and concentration of oxalic-acid bath on formation and dissolution of aluminum-oxide film," *T. Natl. Res. Inst. M.*, vol. 18, p. 197, 1975.
- [112] H. Takahashi and M. Nagayama, "Distribution of phosphate ions in porous anodic oxide film formed on aluminum in phosphoric-acid solution," *Nippon Kagaku Kaishi*, vol. 3, p. 453, 1974.
- [113] S. Ono, H. Ichinose, and N. Masuko, "The high-resolution observation of porous anodic films formed on aluminum in phosphoric-acid solution," *Corr. Sci.*, vol. 33, p. 841, 1992.
- [114] V. Lehmann and H. J. Föll, "Formation mechanism and properties of electrochemically etched trenches in n-type silicon," *Electrochem. Soc.*, vol. 137, p. 653, 1990.
- [115] P. Güthner and D. Dransfeld, "Local poling of ferroelectric polymers by scanning force microscopy," *Appl. Phys. Lett.*, vol. 61, no. 9, p. 1137, 1992.
- [116] F. Jona and G. Shirane, "Ferroelectric crystals," 1962. Pergamon Press.
- [117] D. Vanderbilt and M. H. Cohen, "Monoclinic and triclinic phases in higher-order Devonshire theory," *Phys. Rev. B*, vol. 63, p. 094108, 2001.
- [118] V. Lehmann, "The physics of macropore formation in low doped n-type silicon," *J. Electrochem. Soc.*, vol. 140, p. 2836, 1993.
- [119] M. Steinhart, J. H. Wendorff, A. Greiner, R. B. Wehrspohn, K. Nielsch, J. Schilling, J. Choi, and U. Gösele, "Polymer nanotubes by wetting of ordered porous templates," *Science*, vol. 296, p. 1997, 2002.
- [120] O. Auciello, A. Gruverman, H. Tokumoto, S. A. Prakash, S. Aggarwal, and R. Ramesh, "Nanoscale scanning force imaging of polarization phenomena in ferroelectric thin films," *MRS Bull.*, vol. 23, p. 33, 1998.
- [121] M. G. Broadhurst and G. T. Davis, "Topics in applied physics: Electrets, chap 5," 1980.
- [122] F. J. B. Calleja, A. G. Arche, and T. A. Ezquerro, "Structure and properties of ferroelectric copolymers of poly(vinylidene fluoride)," *Adv. Polym. Sci.*, vol. 108, p. 1, 1993.
- [123] J. B. Lando and W. W. Doll, "The polymorphism of poly(vinylidene fluoride) I. The effects of head-to-head structure," *J. Macromol. Sci. Phys. B*, vol. 2, p. 205, 1968.
- [124] G. Eberle, H. Schmidt, and W. Eisenmenger, "Piezoelectric polymer electrets," *IEEE Trans. Electr. Ins.*, vol. 3, p. 624, 1996.
- [125] Y. Tajitsu, H. Ogura, A. Chiba, and T. Furukawa, "Investigations on switching characteristics of vinylidene fluoride/trifluoroethylene copolymers in relation to their structure," *Jpn. J. Appl. Phys.*, vol. 26, p. 554, 1987.
- [126] W. L. Bongiani, "Effect of crystallization and annealing on thin films of vinylidene fluoride-trifluoroethylene (VF₂/F₃E) copolymers," *Ferroelectrics*, vol. 103, p. 57, 1990.
- [127] L. Jie, C. Baur, and K. Dransfeld, "Microscopic decoration of ferroelectric polymer surfaces by gold films," *Ferroelectrics*, vol. 171, p. 103, 1995.
- [128] S. Ikeda, Z. Shimojima, and M. Kutani, "Correlation between ferroelectric phase transition and crystallisation behavior of ferroelectric polymers," *Ferroelectrics*, vol. 109, p. 297, 1990.

- [129] A. Kumar and M. M. Perlman, "Simultaneous stretching and corona poling of PVDF and P(VDF-TrFE) films," *J. Phys. D: Appl. Phys.*, vol. 26, p. 469, 1993.
- [130] A. J. Lovinger, "Polymorphic transitions in ferroelectric copolymers of vinylidene fluoride induced by electron irradiation," *Macromolecules*, vol. 18, p. 910, 1985.
- [131] T. Furukawa and G. E. Johnson, "Measurements of ferroelectric switching characteristics in polyvinylidene fluoride," *Appl. Phys. Lett.*, vol. 38, p. 1027, 1981.
- [132] M. Womes, E. Bihler, and W. Eisenmenger, "Dynamics of polarization growth and reversal in PVDF films," *IEEE Trans. Electr. Ins.*, vol. 24, p. 461, 1989.
- [133] G. Eberle, E. Bihler, and W. Eisenmenger, "Polarization dynamics of P(VDF-TrFE) copolymers," *IEEE Trans. Electr. Ins.*, vol. 26, p. 69, 1991.
- [134] T. Furukawa, "Piezoelectricity and pyroelectricity in polymers," *IEEE Trans. Electr. Ins.*, vol. 24, p. 375, 1989.
- [135] A. J. Lovinger, G. T. Davis, T. Furukawa, and M. Broadhurst, "Crystalline forms in a copolymer of vinylidene fluoride and trifluoroethylene (52/48 mol-percent)," *Macromolecules*, vol. 15, p. 323, 1982.
- [136] K. Tashiro, K. Takano, M. Kobayashi, Y. Chatani, and H. Tadokoro, "Structural study on ferroelectric phase-transition of vinylidene fluoride-trifluoroethylene co-polymers (III): Dependence of transition behavior on vdf molar content," *Ferroelectrics*, vol. 57, p. 297, 1984.
- [137] B. Wunderlich *Macromolecular Physics*, vol. 1, 1973. New York: Academic Press.
- [138] K. J. Kim, G. B. Kim, C. L. Valencia, and J. F. Rabolt, "Curie transition, ferroelectric crystal structure, and ferroelectricity of a VDF/TrFE(75/25) copolymer. 1. the effect of the consecutive annealing in the ferroelectric state on curie transition and ferroelectric crystal structure," *J. Polym. Sci., Part B: Polym. Phys.*, vol. 32, p. 2435, 1994.
- [139] D. Naegele and D. Y. Yoon, "Orientation of crystalline dipoles in poly(vinylidene fluoride) films under electric-field," *Appl. Phys. Lett.*, vol. 33, p. 132, 1978.
- [140] G. T. Davis, J. E. McKinney, M. G. Broadhurst, and S. C. Roth, "Electric-field-induced phase changes in poly(vinylidene fluoride)," *J. Appl. Phys.*, p. 49, 4998.
- [141] R. G. Kepler and R. A. Anderson, "Ferroelectricity in polyvinylidene fluoride," *J. Appl. Phys.*, p. 49, 1232.
- [142] A. J. Bur, J. D. Barnes, and K. J. Wahlstrand, "A study of thermal depolarization of polyvinylidene fluoride using X-ray pole-figure observations," *J. Appl. Phys.*, p. 59, 2345.
- [143] T. Furukawa, M. Date, E. Fukada, E. Tajitsu, and A. Chiba, "Ferroelectric behavior in the co-polymer of vinylidene fluoride and trifluoroethylene," *Jpn. J. Appl. Phys.*, vol. 19(2), p. L109, 1980.
- [144] T. Yamada and T. Kitayama, "Ferroelectric properties of vinylidene fluoride-trifluoroethylene copolymers," *J. Appl. Phys.*, vol. 52, p. 6859, 1981.
- [145] J. P. Luongo, "Far-infrared spectra of piezoelectric polyvinylidene fluoride," *J. Polym. Sci. A-2*, vol. 10, p. 1119, 1972.
- [146] E. Fukada, M. Date, and T. Furukawa, "Piezoelectricity and dipolar orientation in polyvinylidene fluoride," *Am. Chem. Soc. Org. Coat. Plast. Chem. Prepr.*, vol. 38, p. 262, 1978.

- [147] M. G. Broadhurst and G. T. Davis, "Ferroelectric polarization in polymers," *Annu. Rep. Conf. Electr. Insul. Diel. Phem*, vol. 48, p. 447, 1979.
- [148] H. Ohigashi and J. Koga, "Ferroelectric copolymers of vinylidene fluoride and trifluoroethylene with a large electro-mechanical coupling factor," *Japan J. Appl. Phys.*, vol. 21, p. L455, 1982.
- [149] Y. Takahashi and A. Odajima, "On the structure of poly(vinylidene fluoride) under a high electric-field," *Ferroelectrics*, vol. 57, p. 221, 1984.
- [150] K. Nakamura, Y. Teramoto, and N. Muruyama, "Rotation of polar axis of beta-form poly(vinylidene fluoride) under high electric-field," *Ferroelectrics*, vol. 57, p. 139, 1984.
- [151] F. Xia, H. Xu, F. Fang, B. Razavi, Z. Cheng, Y. Lu, B. Xu, and Q. Zhang, "Thickness dependence of ferroelectric polarization switching in poly(vinylidene fluoride-trifluoroethylene) spin cast film," *Appl. Phys. Lett.*, vol. 78, p. 1122, 2001.
- [152] F. Xia, B. Razavi, H. Xu, Z. Cheng, and Q. Zhang, "Dependence of threshold thickness of crystallization and film morphology of film processing conditions in poly(vinylidene fluoride-trifluoroethylene) copolymer thin film," *J. Appl. Phys.*, vol. 92, p. 3111, 2002.
- [153] J. A. Day, E. L. V. Lewis, and G. R. Davies, "X-ray structural study of oriented vinylidene fluoride/trifluoroethylene copolymers," *Polymer*, vol. 33, p. 1571, 1992.
- [154] M. A. Barique, M. Sato, and H. Ohigashi, "Thickness dependence of orientation factors of crystal axes in poly(vinylidene fluoride/trifluoroethylene) single crystalline films," *Polym. J.*, vol. 33, p. 169, 2001.
- [155] R. Hasegawa, Y. Takahashi, Y. Chatani, and H. Tadokoro, "Crystal-structures of 3 crystalline forms of poly(vinylidene fluoride)," *Polym. J.*, vol. 3, p. 600, 1972.
- [156] C. Harnagea, "Local piezoelectric response and domain structures in ferroelectric thin films investigated by voltage-modulated force microscopy," *Thesis, Martin-Luther-Universität Halle-Wittenberg*, 2001.
- [157] S. S. Guo, X. Z. Zhao, S. G. Lu, S. T. Lau, and H. L. W. Chan, "Effect of electron irradiation on poly(vinylidene fluoride-trifluoroethylene) 56/44 mol% copolymers," *J. Phys. D: Appl. Phys.*, vol. 37, p. 472, 2004.
- [158] M. Steinhart, Z. H. Jia, A. K. Schaper, R. B. Wehrspohn, U. Gösele, and J. H. Wendorff, "Palladium nanotubes with tailored wall morphologies," *Adv. Mat.*, vol. 15, p. 706, 2003.
- [159] H. Hou, Z. Jun, A. Reuning, A. Schaper, J. H. Wendorff, and A. Greiner, "Poly(p-xylylene) nanotubes by coating and removal of ultrathin polymer template fibers," *Macromolecules*, vol. 35, p. 2429, 2002.
- [160] H. P. Klug and L. E. Alexander, "X-ray diffraction procedures," 1954. New York: Wiley.
- [161] B. G. Levi, "Do atomic force microscope arrays have the write stuff?," *Phys. Today*, vol. 55, p. 14, 2002.

9. Curriculum vitae

First Name	Yun
Family Name	Luo
Date of Birth	September 8, 1976 (Shanghai, P. R. China)
Nationality	Chinese
E-mail	<i>luo@mpi-halle.de</i> or <i>Yun.Luo@polytechnique.org</i>

EDUCATION

<i>Jan. 2002 - present</i>	Max Planck Institute of Microstructure Physics and Martin-Luther-University Halle Wittenberg (Halle, Germany) Ph.D. candidate (Supervisors: Prof. Ulrich Gösele and Prof. Ralf B. Wehrspohn)
<i>Aug. 2000 - Jul. 2001</i>	Ecole Polytechnique (Palaiseau, France) Diplôme d'Études Approfondies in Physics
<i>Sep. 1998 - Jul. 2000</i>	Ecole Polytechnique (Palaiseau, France) Diplôme d'Ingénieur in Physics
<i>Feg. 1995 - Jul. 1998</i>	Fudan University (Shanghai, P. R. China) Bachelor's Degree in Physics

PROFESSIONAL EXPERIENCE

<i>Sep. 1999 - Aug. 2000</i>	Fontainebleau Research Centre of Corning Science and Technology Group Research Assistant Er-doped Polymers for Planar Optical Amplifiers.
------------------------------	---

List of publications

- **Y. Luo**, S. K. Lee, H. Hofmeister, D. Hesse, M. Steinhart, and U. Gösele, “Pt nanoshell tubes by template wetting”, *Nanoletts.*, vol. **4**, pp. 143, 2004.
- **Y. Luo**, I. Szafraniak, V. Nagarajan, R. B. Wehrspohn, M. Steinhart, J. H. Wendorff, N. D. Zakharov, R. Ramesh and M. Alexe, “Ferroelectric Lead Zirconate Titanate and Barium Titanate Nanoshell Tubes”, *MRS Symp. Proc.*, vol. **782**, pp. 415, 2004.
- M. Steinhart, P. Goring, **Y. Luo**, H. Hofmeister, A. Greiner, J. H. Wendorff, R. B. Wehrspohn, E. Pippel, and U. Gösele, “Nanotubes with Complex Wall Architectures by Template Wetting”, *Abstracts of the American Chemical Society* vol. **227**, pp. 332, 2004.
- R. B. Wehrspohn, J. Schilling, J. Choi, **Y. Luo**, S. Matthias, S. Schweizer, F. Müller, U. Gösele, S. Lölkes, S. Langa, J. Carstensen, and H. Föll, “Chapter 4: Electrochemically-prepared 2D and 3D Photonic Crystals, in *Photonic Crystals: Advances in Design, Fabrication, and Characterization*”, Wiley-VCH, pp. 63, 2004.
- **Y. Luo**, I. Szafraniak, N. D. Zakharov, V. Nagarajan, M. Steinhart, R. B. Wehrspohn, J. H. Wendorff, R. Ramesh, and M. Alexe, “Ferroelectric Switching of Nanotubes Composed of Lead Zirconate Titanate and Barium Titanate”, *Appl. Phys. Lett.*, vol. **83**, pp. 440, 2003.
- F. D. Morrison, **Y. Luo**, I. Szafraniak, V. Nagarajan, R. B. Wehrspohn, M. Steinhart, J. H. Wendorff, N. D. Zakharov, E. D. Mishina, K. A. Vorotilov, A. S. Sigov, S. Nakabayashi, M. Alexe, R. Ramesh, and J. F. Scott, “Ferroelectric nanotubes”, *Adv. Mat. Sci.*, vol. **4**, pp. 114, 2003.
- J. Choi, **Y. Luo**, R. B. Wehrspohn, R. Hillebrand, J. Schilling, and U. Gösele, “Perfect two-dimensional porous alumina photonic crystals with duplex oxide layers”, *Journal of Applied Physics*, vol. **94**, pp. 4757, 2003.
- **Y. Luo**, I. Szafraniak, N. D. Zakharov, V. Nagarajan, M. Steinhart, R. B. Wehrspohn, J. H. Wendorff, R. Ramesh, and M. Alexe, “Ferroelectric lead zirconate titanate and barium titanate nanotubes”, *Integr. Ferroelectr.*, vol. **9**, pp. 1513, 2003.

List of presentations (selection)

- **Y. Luo**, M. Geuss, P. Göring, K. Rademann, M. Steinhart, and U. Gösele, “Ferroelectric Properties of P(VDF-co-TrFE) Copolymer Nanotubes”, *11th International Conference on Polymeric Materials*, Halle, Germany, September 29 - October 01, 2004, poster.
- M. Steinhart, P. Goring, **Y. Luo**, H. Hofmeister, A. Greiner, J. H. Wendorff, R. B. Wehrspohn, E. Pippel, and U. Gösele, “Nanotubes with Complex Wall Architectures by Template Wetting”, *227th National Meeting of the American Chemical Society*, Anaheim, USA, March 28 - April 01, 2004, poster.
- M. Steinhart, P. Göring, **Y. Luo**, H. Hofmeister, M. Alexe, E. Pippel, and U. Gösele, “Nano- and Microtubes with Complex Wall Morphologies”, *Particles 2004: Particle Synthesis, Characterization, and Particle-based Advanced Materials*, Orlando, USA, March 06-09, 2004, talk.
- **Y. Luo**, J. Choi, R. B. Wehrspohn, R. Hillebrand, J. Schilling, and U. Gösele, “Fabrication and Optical Characterization of 2D Porous Alumina Photonic Crystals with Duplex Oxide Layers”, *International Symposium on Photonic and Electromagnetic Crystal Structures V (PECSV)*, Kyoto, Japan, March 07-12, 2004, poster.
- **Y. Luo**, I. Szafraniak, V. Nagarajan, R. B. Wehrspohn, M. Steinhart, J. H. Wendorff, N. D. Zakharov, R. Ramesh and M. Alexe, “Ferroelectric Lead Zirconate Titanate and Barium Titanate Nanoshell Tubes”, *Symposium on Micro- and Nanosystems of the 2003 MRS Fall Meeting*, Boston, USA, December 01-05, 2003, talk.
- M. Steinhart, P. Göring, **Y. Luo**, H. Hofmeister, M. Alexe, E. Pippel, and U. Gösele, “Komplex aufgebaute Nanoröhren durch Templatbenetzung”, *BMBF-Innovationsforum Nanostrukturierte Materialien*, Halle, Germany. November 24-25, 2003, talk.
- M. Steinhart, **Y. Luo**, M. Alexe, Z. Jia, A. K. Schaper, R. B. Wehrspohn, J. H. Wendorff, V. Nagarajan, R. Ramesh, U. Gösele, “Functionalized nNanotubes by Wetting of Porous Templates”, *2nd International Nanotechnology Symposium*, Dresden, Germany, November 20-21, 2003, talk.
- J. Choi, **Y. Luo**, R. B. Wehrspohn, R. Hillebrand, J. Schilling, and U. Gösele, “Synthesis of Dielectric and Metallo-dielectric Photonic Crystals based on Porous Alumina with Adjustable Ratios of Radius to Interpore Distance”, *Materials Research Society Spring Meeting (MRS)*, San Francisco, USA, April 21-25, 2003, poster.
- **Y. Luo**, J. Choi, J. Schilling, R. Hillebrand, R. B. Wehrspohn, and U. Gösele, “Fabrication and optical characterization of porous alumina photonic crystals via imprint method”, *Frühjahrstagung des Arbeitskreises Atome, Moleküle, Quantenoptik und Plasmen der Deutschen Physikalischen Gesellschaft*, Hannover, Germany, March 24-28, 2003, poster.
- **Y. Luo**, I. Szafraniak, V. Nagarajan, R. B. Wehrspohn, M. Steinhart, J. H. Wendorff, N. D. Zakharov, R. Ramesh and M. Alexe, “Ferroelectric Lead Zirconate Titanate and Barium Titanate Nanotubes”, *15th International Symposium on Integrated Ferroelectrics COLORADO SPRINGS*, Colorado, USA, March 09-12, 2003, poster.

Patent

M. Alexe, **Y. Luo**, I. Szafraniak, R. B. Wehrspohn, and M. Steinhart

”Piezoelectric actuators, transducers and storage devices based on piezoelectric nanotubes and a method of fabrication”

European patent, No. 03000969.0 (16.01.2003)

Acknowledgements

Traveling together is easier for a trip during which interdependence is more valuable than independence. This thesis is the result of three years of work whereby I have been accompanied and supported by many people. Now comes the pleasant moment that I have the opportunity to express my gratitude to all of them.

First, I would like to thank my supervisor, Prof. Gösele. During these years I have known him as a sympathetic and principle-centered person. His overly enthusiasm and integral view on research has made a deep impression on me. I owe him lots of gratitude for having shown me this way of research.

I wish to express my gratitude to Prof. Wehrspohn who always kept an eye on the progress of my work and was available when I needed his advises.

Special thanks go to Dr. Steinhart, who introduced me to the area of template-wetting method. He also monitored my work and took great effort in reading and providing me with valuable comments on earlier versions of this thesis. Besides of being an excellent promotor, Dr. Steinhart was as close as a good friend to me.

I wish to acknowledge Dr. Alexe and Dr. Hesse for introducing me the aspects of ferroelectrics in my research.

The “Ordered Porous Materials” group at MPI-Halle substantially contributed to the development of this work. The strict and extensive comments and the many discussions within the group had a direct impact on the final form and quality of this thesis. I thank Torsten and Sven, for not only sharing the same office, but also reminding me to keep an eye on the developments of photonic crystals. I thank Silko and Katrin, for always providing me porous alumina templates on time. Petra invested much time investigating XRD on my numerous samples. Mrs. Möhner supported my work with her skilled techniques in manipulating ultra-microtome as well as in making delicious cakes. I am also indebted to Cécile (now at the University of Surrey in England) and Jinsub (now at Caltech for their great friendships). This chain of gratitude should certainly touch everyone in our group. Many thanks for being your colleague.

I feel a deep sense of gratitude for Dr. Hofmeister, Dr. Pippel, Dr. Erfurth, Mrs. Hopfe and Dr. Hempel for their support to get deeper understanding of the structures realized in my work via electron microscopies and DSC measurements.

I deeply thank all Chinese friends in Halle for their support and friendship. During the last 3 years, I was continuously encouraged and supported by them.

This thesis is dedicated to my husband and parents. Without their endless love and sacrifice, nothing would have been accomplished.

Eidesstattliche Erklärung

Ich erkläre hiermit, dass ich keine anderen als die von mir angegebenen Quellen und Hilfsmittel zur Erstellung meiner Dissertation verwendet habe. Den benutzten Werken wörtlich oder inhaltlich entnommene Stellen sind als solche gekennzeichnet.

Yun Luo

Halle (Saale), im Februar 2005